Reconfigurable Metasurfaces in the Infrared

Reconfigurable Metasurfaces in the Infrared

A dissertation presented

by

Shuyan Zhang

to

The John A. Paulson School of Engineering and Applied Sciences

in partial fulfilment of the requirements

for the degree of

Doctor of Philosophy

in the subject of

Applied Physics

Harvard University

Cambridge, Massachusetts

December 2017

Dissertation advisor: Federico Capasso **Author: Shuyan Zhang**

Reconfigurable Metasurfaces in the Infrared

Abstract

Recently there has been great interest in the applications of infrared (IR) light in many areas, including infrared imaging, trace-gas detection, biological and medical sensing, and environmental monitoring. Over the last decade, there has been major progress in the development of new IR sources and detectors. However, a limiting factor in the development of IR optics is the lack of suitable materials that are transparent, low cost, lightweight, and easy to fabricate.

A new class of optical components based on metasurfaces could be used to overcome these limitations. In contrast to conventional optical components that achieve wavefront engineering by phase accumulation through light propagation in the medium, these components control the wavefront of light using arrays of optical resonators with subwavelength dimensions, which are patterned on a surface to introduce a desired spatial profile of optical phase. By tailoring the properties of each element of the array, one can spatially control the phase, amplitude, and/or polarization of the scattered light and consequently mold the wavefront. Their exceptional optical properties have led to the development of ultrathin optical devices with various functionalities outperforming their conventional bulky counterparts or demonstrating new optical phenomena

covering a wide range of spectrum from the visible to the terahertz. However, most of the metasurface devices are static, limiting the functions that can be achieved.

In this thesis, reconfigurable metasurface devices at IR wavelengths based on three types of tuning mechanisms are designed and fabricated: (1) a metasurface absorber and a metasurface polarizer based on a phase transition material, vanadium dioxide (VO_2); (2) a metasurface lens integrated with a Micro-Electro-Mechanical System (MEMS); (3) a metasurface lens and aberration corrector based on dielectric elastomer actuators (DEAs). These devices were designed to operate in the long-wave IR (LWIR, 8 – 14 μm), mid-wave IR (MWIR, 3 – 5 μm), and short-wave IR (SWIR, 1 – 3 μm), respectively. However, the design principles of these devices can be generalized to other wavelength ranges.

Contents

List of Figures

List of Tables

Acknowledgements

Firstly, I would like to express my sincere gratitude to my advisor Prof. Federico Capasso for the continuous support of my Ph.D. study and related research, for his patience, motivation, and immense knowledge. His guidance helped me in all the time of research and writing of this thesis. I could not have imagined having a better advisor and mentor for my Ph.D. study. Federico is also very kind like my grandfather. He was my wedding officiant and cared for me when I gave birth to my new baby.

Besides my advisor, I would like to thank the rest of my thesis and qualifying committee: Prof. Evelyn Hu, Prof. Philip Kim, Prof. Marko Lončar, and Prof. Jene Golovchenko for their insightful comments and encouragement, but also for the hard question which incentivized me to widen my research from various perspectives.

I thank my funding agency, Agency for Science, Technology and Research (A*STAR Singapore) for their generous support for my Ph.D. study.

My sincere thanks also goes to Dr. Mikhail A. Kats, who is now an assistant professor. He was my mentor when I first joined the Capasso group. I started with him working on the VO_2 project and lasted for two years. He taught me patiently and step by step how to use the cleanroom facilities and run computer simulations.

I thank my collaborators: You Zhou, Prof. Shriram Ramanathan, Jura Rensberg, Prof. Carsten Ronning (VO_2 project), Myoung-Hwan Kim, Prof. Nanfang Yu, Alex Soibel (Lens project), Tapashree Roy, Daniel Lopez (MEMS project), Samuel Shian, and Prof. David Clarke

(DE project). I thank the staff in the cleanroom, especially Yuan Lu, Guixiong Zhong, and JD Deng. Also, I thank my fellow labmates, Francesco Aieta and Tobias Mansuripur for the stimulating discussions and other Capasso group members and friends from the department for all the fun we have had.

Last but not the least, I would like to thank my family: my parents and my husband for supporting me spiritually throughout and my life in general. In particular, to my husband, Alan She, I am so fortunate to have you as my life partner as well as my lab partner! Thank you for being such a good company in the past five years.

Dedicated to

my parents and my husband

Chapter 1
Introduction

From auroras and rainbows to the human eye – light has fascinated scientists for centuries. Today, optical technologies – from lasers to solar cells to cameras – harness light to advance physics and serve societies' needs. The understanding and use of the fundamental properties of light is an important part of the development of the human history. The most influential discoveries and development milestones of light include the long debate on the character of light in 1600s; August Fresnel's proposal in 1815 that light is a wave; James Clerk Maxwell's electromagnetic theory of light in 1865; Albert Einstein's theory of General Relativity 1915; the study of solar cells in 1954; the invention of lasers in 1960; the discovery of the cosmic microwave background radiation and the development of optical fibers for communication in 1965; high resolution laser spectroscopy and frequency metrology in 1981; and the more recent hot research topics in plasmonics and metamaterials [1].

Physicist Richard Feynman had a famous quote, "there is plenty of room at the bottom," referring to the promise of nanotechnology [2]. The development of photonic materials, circuitry, devices, and probes on the nanoscale has opened up new opportunities for controlling light in the subwavelength regime. Metamaterials are artificial composite nanostructures with unique properties for controlling electromagnetic waves and have numerous intriguing novel optical effects and applications that cannot be achieved by natural materials [3]–[6]. Metasurfaces, benefit from the reduced dimensionality of metamaterials, however, are relatively easy to fabricate and possess smaller footprint. There has been increasing interest in the past decade as they carry great feasibility for realization and demonstrate remarkable capabilities for light molding beyond that

offered by conventional planar interfaces [7]–[11]. These optical components control the wavefront of light using arrays of optical resonators with subwavelength dimensions, which are patterned on a surface to introduce a desired spatial profile of optical phase. By tailoring the properties of each element of the array, one can spatially control the phase of the scattered light and consequently shape the wavefront. Besides subwavelength optical resonators, metasurfaces can also be created by using optically thin films made of lossy materials with the imaginary part of the complex refractive index comparable to the real part. The phase changes on reflection or transmission of light at the boundary between lossy media can be substantially different from 0 or π, which enable nanometer-thin films to substantially modify the incident light properties [10], [11].

The governing equations of the interaction of light of the metasurfaces composed of nanostructures designed and arranged in specific patterns at the interface between two media are summarized as the generalized Snell's laws derived from the Fermat's principle:

$$\begin{cases} sin(\theta_t)n_t - sin(\theta_i)n_i = \frac{\lambda_0}{2\pi}\frac{d\Phi}{dx} \\ sin(\theta_r) - sin(\theta_i) = \frac{\lambda_0}{2\pi n_i}\frac{d\Phi}{dx} \end{cases}, \quad (1)$$

where θ_t, θ_r, and θ_i represent the angle of transmission, reflection, and incidence, respectively [12]. Using these design equations, planar counterparts of conventional bulky optical devices like lenses [13]–[21], beam deflectors [12], holograms [22], [23], polarimeters [24] and so on have been designed and experimentally demonstrated. Such metasurface-based flat devices represent a new class of optical components that are compact, flat and lightweight.

Recently, a variety of tuning mechanisms have been proposed to add functionalities to

static metasurfaces. For instance, flexible substrates made of poly(dimethylsiloxane) (PDMS) were used for conformal metasurfaces [25] and mechanically reconfigurable metasurfaces [26]. The high flexibility and stretchability of soft materials such as PDMS and poly(methyl methacrylate) (PMMA) made it possible for the substrates to be wrapped and bent around. Phase transition materials have been widely used in optical data-storage systems and nanophotonic systems based on their tunable optical properties. Commonly used materials include vanadium dioxide (VO_2) [27]–[29] and GeSbTe alloys [30], which show a dramatic change in optical properties when undergoing phase transitions. The reversible phase transition can be triggered by thermal energy or chemical doping. Liquid crystals have also been extensively used for the dynamic control of the optical properties because of their broadband optical nonlinearity and birefringence. Their refractive-index change can be externally tuned by temperature, light, and electric or magnetic fields [31], [32]. Microfluidic technology has been applied to tunable metalenses by controlling the air pressure of the pneumatic valves to change the distribution of liquid metals within a unit cell [33]. In addition, two-dimensional materials with extraordinary optical and electrical properties such as graphene were integrated to electrically tunable metasurfaces. Their optical properties were made tunable through a change in the charge-carrier density which was controlled by the gate voltage [34].

The application of metasurfaces in the infrared spectrum is highly desirable. Infrared light is a scientific breakthrough that has led to advancements in many fields and applications including night vision, thermography, tracking technology, metrology, art history, heating, and astronomy. A limiting aspect for the development of infrared optics is represented by the scarcity of materials that are at the same time low-loss, lightweight and easy to mold. Here we design and implement

metasurfaces comprising subwavelength features which provide subwavelength resolution of optical wavefronts. They are extremely thin, light-weight, and free from spherical aberration compared to conventional bulky optical components. For example, metasurfaces can replace the mirrors in the Cassegrain telescope which tend to sag over time and make less accurate measurements. The infrared spectrum was divided into three regions, i.e. short-wave infrared (SWIR) ranging from 1 – 3 μm, mid-wave infrared (MWIR) ranging from 3 – 5 μm, and long-wave infrared (LWIR) ranging from 8 – 14 μm.

The purpose of this thesis is to study reconfigurable metasurface devices based on three types of tuning mechanisms. The applications are in the infrared wavelength region. It is organized into five chapters and their contents are summarized below:

Chapter 1 introduces the background and gives an overview of the thesis structure.

Chapter 2 presents reconfigurable metasurface devices based on vanadium dioxide (VO_2) in the LWIR: Active, widely tunable optical materials have enabled rapid advances in photonics and optoelectronics, especially in the emerging field of meta-devices. We demonstrate that spatially selective defect engineering on the nanometer scale can transform phase transition materials into optical metasurfaces. Using ion irradiation through nanometer-scale masks, we selectively defect-engineered the insulator-metal transition of VO_2, a prototypical correlated phase-transition material whose optical properties change dramatically depending on its state. Using this robust technique, we demonstrated several optical metasurfaces, including tunable absorbers with artificially induced phase coexistence and tunable polarizers based on thermally triggered dichroism. Spatially selective nanoscale defect engineering represents a new paradigm for active photonic structures and devices.

Chapter 3 discusses two types of metasurface lens designs in MWIR, i.e. reflective and transmissive metasurface lenses: We report the demonstration of a mid-IR reflection-based flat lens with high efficiency and near diffraction-limited focusing. Focusing efficiency as high as 80%, in good agreement with simulations (83%), has been achieved at 45^{o} incidence angle at $\lambda = 4.6$ μm. The off-axis geometry considerably simplifies the optical arrangement compared to the common geometry of normal incidence in reflection mode which requires beam splitters. Simulations show that the effects of incidence angle are small compared to parabolic mirrors with the same NA. The use of single-step photolithography allows large-scale fabrication. Such a device is important in the development of compact telescopes, microscopes, and spectroscopic designs. We also show a new type of transmissive metasurface lens design that operates as an immersion lens (i.e. focuses light inside the GaSb substrate instead of in the air) in the mid-IR. Such a lens is designed to be integrated with barrier infrared detectors (BIRD). BIRD devices with small (<30 μm) active elements are fabricated to reduce the detector volume (and therefore dark current). The size reduction combined with increasing optical collection efficiency by the integrated lens is predicted to enhance the signal-to-noise ratio by 5-10 times.

Chapter 4 presents reconfigurable metasurface devices based on Micro-Electro-Mechanical System (MEMS) technology in the MWIR: We demonstrate for the first time a monolithic MEMS integrated with a reflective metasurface-based flat lens that focuses incident light in the mid-IR spectrum. The two-dimensional scanning MEMS platform controls the angle of the lens along two orthogonal axes (tip-tilt) by ±9 degrees enabling dynamic beam steering. When the incident light deviates from the designed angle, the device can compensate for the off-axis angle and thus correct for any off-axis aberrations such as coma. We show that, for low

angular displacements, the integrated lens-on-MEMS system does not affect the mechanical performance of the MEMS actuators and preserves the focused beam profile as well as the measured beam width. We envision a new class of flat optics devices with active control provided by the combination of metasurfaces and MEMS for a wide range of applications, such as miniaturized MEMS-based microscope systems, LIDAR scanners, and projection systems.

Chapter 5 presents reconfigurable metasurface devices based on dielectric elastomer actuators (DEAs) in the SWIR: Tunable optical devices, in particular, varifocal lenses, have important applications in various fields, including imaging and adaptive vision. We have demonstrated for the first time an electrically tunable flat lens, based on large area metasurfaces combined with a dielectric elastomer actuator having inline transparent electrodes, that is capable of simultaneously performing focal length tuning (>100%) as well as dynamic corrections, including astigmatism and image shift. This offers control versatility to flat optics hitherto only possible in electron microscopes. The water-based transfer process, which we describe, also enables wide compatibility across materials. The combination of metasurface optics and dielectric elastomer actuators enables a new, versatile platform for creating all kinds of tunable optical devices, through the design of tunable phase, amplitude, and polarization profiles.

Chapter 2
Reconfigurable metasurface devices based on vanadium dioxide (VO_2) in LWIR

Vanadium dioxide (VO_2) is a correlated electron material which features an insulator-metal transition (IMT). The thermally driven IMT occurs near room temperature (~70 ^oC) and results in an on/off resistance ratio of up to five orders of magnitude [35]. This IMT also results in a large change in the optical transmittance in the near-infrared spectral range, which has found applications in energy-efficient windows [36] and high-efficiency switches [37]; in the infrared a close-to-zero reflectance has been used as a perfect absorber [38], thermal emitter [39], and resonance tuning of optical antennas [40], among others. The onset of the IMT can be percolative in nature, accompanied by phase inhomogeneity where the metallic and insulating phase coexist and various aspects of the transition are an active area of study [37], [41]–[43]. The transition can be driven electrically by current injection and the threshold can be modulated by external stimuli including pressure and ambient temperature or by chemical doping [44].

Probing the physics of this intermediate state is still at an early stage because the material quality of VO_2 films has only recently been improved to the point where a complex region such as the intermediate state of the phase transition can be explored with reproducibility. The IMT in this material has been known for over 50 years; however, bulk crystals often crack during the transition because of stress (as is often the case for brittle ceramics) [45]. Thin-film structures can be made more robust to the stress relaxation caused by substrate clamping; however, careful thermal profiles and composition control are required to obtain reversible transition properties [46], [47]. Studies on thin-film VO_2 with reproducible phase-transition properties can be considered an

emerging field, and within that, the intermediate state (i.e., a mixture of metallic and insulating states) is now being recognized as an opportunity, especially given recent interest in metamaterials that often require composite structures comprising domains of subwavelength dimensions with vastly different optical properties [48].

In this chapter, optical properties of VO_2 in the LWIR region will be discussed in detail. It is further divided into two sections. Two types of methods of triggering the phase transition are investigated. The first section utilizes current [49] and the second utilizes temperature [50]. Two metasurface devices were fabricated and measured based on the temperature-controlled phase transition.

2.1 Current-modulated phase transition of VO_2

Recently, VO_2-based spatially tunable gradient index metasurfaces have been demonstrated in the terahertz spectral regime where the tuning was achieved by applying heat or voltage pulses to a VO_2 thin film combined with split ring resonators [51], [52]. However, as the authors pointed out, tradeoffs exist between the degree of spatial control and the strength of the tuning of the optical properties.

In this section, we demonstrate electrical tuning of the mid-infrared optical properties of VO_2 on the micron scale. Our simple design provides dynamic control of the geometry of metallic and insulating phase regions within a compositionally-homogeneous VO_2 thin film. A two-terminal device consisting of a pair of wide electrodes patterned on a VO_2 thin film was fabricated. By current injection, a localized micron-scale conducting path comprising metal-phase VO_2 was formed within the gap between the electrodes, surrounded by insulator-phase VO_2. The spatial

extent of this conducting path and thereby its optical properties can be deterministically controlled locally via the applied current which allows the development of tunable optical devices.

Our sample consists of a VO_2 film grown on a polished c-plane sapphire wafer substrate by radio frequency (rf) magnetron sputtering with a V_2O_5 target (99.9% purity, AJA International, Inc.). During film growth, the substrate temperature and RF source gun power were maintained at 550 ºC and 125 W, respectively. A mixture of 99.50-sccm Ar and 0.50-sccm O_2 was used as the sputtering gas while maintaining the total pressure at 10 mTorr. The film thickness is approximately 230 nm measured by a scanning ellipsometer (Gaertner Scientific) with a root-mean-square roughness value of approximately 3 nm measured by an optical profiler (Taylor Hobson CCI HD optical profiler system). The resistance on/off ratio of the film is $R_{25\ ^oC}/R_{100\ ^oC} = 610$. The transition temperature is 69 ºC given by the average of the maximum of derivative curves $d[log(R)]/dT$ during heating and cooling, respectively, i.e. $T_{IMT} = \left(T_{IMT}^{heating} + T_{IMT}^{cooling}\right)/2$. Figure 2-1(a) shows the resistance change as a function of temperature in a log scale measured by a home-made 2-probe station with a calibrated temperature stage. Resistance values were taken at every 2 degrees Celsius. The resistance on/off ratio is $R_{25\ ^oC}/R_{100\ ^oC} = 610$. To determine the transition temperature T_{IMT} and the hysteresis, we plot the $d[log(R)]/dT$ in Figure 2-2(b). The maxima occur at $T_{IMT}^{heating} = 71\ ^oC$ and $T_{IMT}^{cooling} = 67\ ^oC$. Hence the hysteresis width is the difference between the two which is 4 ºC .

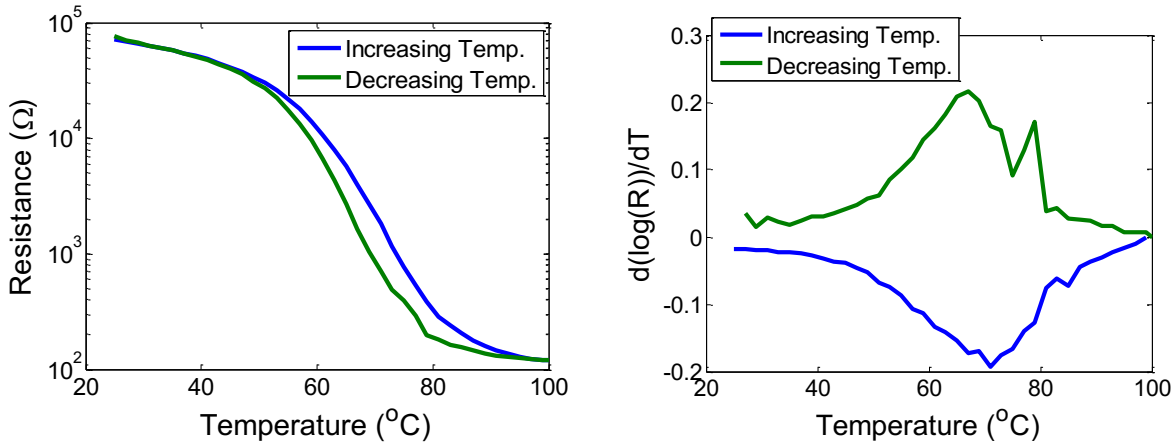

(a) (b)

Figure 2-1 *(a) Study of resistance change above and below the phase transition. (b) Determination of the transition temperature and the hysteresis width during heating and cooling. The hysteresis width ($T_{IMT}^{heating} - T_{IMT}^{cooling}$) is 4 °C.*

A pair of metallic electrodes was patterned on the sample using direct-write photolithography (MicroChem LOR3A, Shipley S1818 photoresist, and Heidelberg μPG501 writer), electron beam evaporation (Denton evaporator), and lift-off. The electrode composition was Ti (10 nm)/Au (300 nm). The gap between the electrodes was 15 μm and the width was 300 μm. The sample was mounted on a probe station and characterized using a parameter analyzer (Agilent 4156C). Before all other electrical measurements, electroforming of the contacts was performed to break down any oxide layers and to form a conducting path at the Ti-VO_2 interface. The electroforming process involved applying a voltage to the electrodes from 0 to a value at which a sharp increase in conductivity was observed and the I-V curve became S-shaped [53] (12 V in our experiment). The experiments were performed in an ambient atmosphere at room temperature with no external temperature control in the set-up. The Raman spectroscopy study was performed using a WITec Alpha300 confocal Raman microscope with a laser source of λ = 532 nm. The

Fourier transform infrared (FTIR) spectroscopy measurements were performed using a Bruker Vertex 70 FTIR spectrometer with a Hyperion 3000 microscope equipped with a focal plane array (FPA) detector.

Figure 2-2(a) shows a schematic of the two-terminal device and optical microscope images zoomed in on the gap region (black dashed box) when the applied current was gradually increased from 0 to 100 mA. The contrast of the images was increased for visual clarity. Below 18 mA, the increasing current did not lead to any visually noticeable features. When the current reached 18 mA, a dark strip (indicated by black arrows) suddenly appeared. As explained below, this dark strip corresponds to a 'conducting path' – a region of metal-phase VO_2 which has a much higher conductivity than the surrounding insulator-phase VO_2. As the current was increased further, the width of this conducting path increased until it reached the width of the electrodes. Similarly, when the current was decreased, the width decreased as would be expected for the reversible transition. The physics behind the formation of the conducting path was discussed in ref. [54]. We focus on the optical control that this tunable path can provide.

Figure 2-2(b) shows a linear relationship (curve fit with an r-squared value close to 0.99) between the width of the conducting path and the applied current for increasing current (blue curve) and decreasing current (red curve). The slopes of the curves are constant, which means that the current density in the conducting path region is approximately constant over the range of the applied current. Once a conducting path is formed, the local resistance drops significantly, which provides a favorable path for the current flow. Most of the power is dissipated in this metal-phase region, so any additional current elevates the local temperature and hence widens the region.

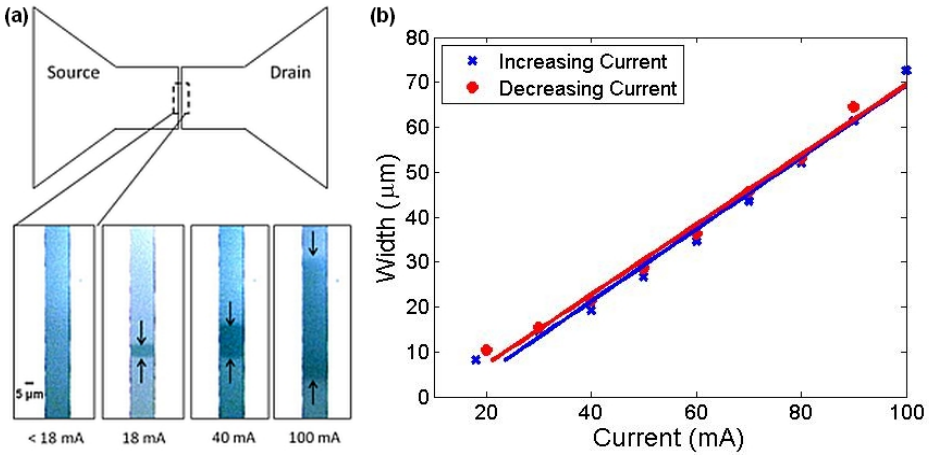

Figure 2-2 *Conducting path dynamics: (a) a schematic of the two-terminal device and optical microscope images zoomed in on the gap region showing a conducting path (indicated by the black arrows) appeared at a threshold current and grew wider as the current was increased (contrast of the images was increased for visual clarity). (b) Curve fit results showing a linear correlation between the width of the conducting path and the applied current in the increasing current mode (blue curve) and the decreasing current mode (red curve).*

Figure 2-3(a) shows the I-V characteristics of the two-terminal device measured using a current source. We observed a region of negative differential resistance (NDR) from 12.5 mA to 91.5 mA for increasing current and from 80.5 mA to 8.5 mA for decreasing current, where the voltage decreased as the current was increased and vice versa. The onset of the NDR region corresponds to the onset of the IMT which is percolative in nature, i.e. the metallic and insulating phase coexist in VO_2 [55], [56]. The difference between the NDR regions of the red curve and the blue curve is a result of the hysteresis [52], [56].

Since the conductance of the insulating phase region is much smaller compared to that of the metallic phase region and assuming that the borders between the metallic phase and insulating phase regions are relatively abrupt, we correlated the electrical measurements and the width of the conducting path to deduce the local resistivity of the metallic phase region. The resistivity ρ is

related to the resistance by $R = \rho \times l/A$, where l is the gap size, A is the product of the width of the conducting path and the thickness of the VO_2 film. In Figure 2-3(b), we plot the measured resistance as a function of the width of the conducting path. We fitted the data with the above expression to obtain the resistivity ρ to be 2.32×10^{-3} Ω·cm with an r-squared value close to 0.99 (black curve) consistent with the literature.

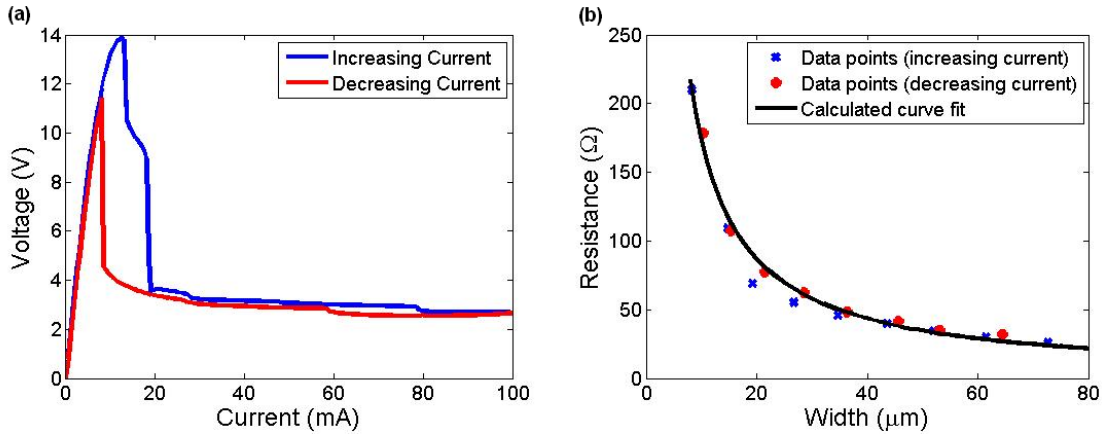

Figure 2-3 *(a) I-V characteristics for increasing current (blue curve) and decreasing current (red curve). (b) The measured resistance is related to the width of the conducting path. The resistivity of the metal-phase VO_2 is determined to be* 2.32×10^{-3} *Ω·cm from the fit of the data.*

Figure 2-4(a) shows the Raman spectroscopy measurements near the conducting path region. Raman measurements are frequently used to study the structural change associated with the IMT [57]. We compared the Raman spectrum at the center of and approximately 50 μm away from the conducting path region (the latter point is outside of the frame in Figure 2-4(b)). The blue curve in Figure 2-4(a) is the Raman spectrum of the VO_2 film with no applied current and the VO_2 film was entirely in its insulating phase. At an applied current of 35 mA, we observed a metal-phase conducting region (red curve); outside the conducting path, the VO_2 appeared to still be in

its insulating phase (black curve). Comparing the red curve with the blue and black curves, several peaks associated with the insulating phase VO_2 vanished (e.g. 196 cm^{-1}, 224 cm^{-1}, and 620 cm^{-1}), but a broad peak at about 390 cm^{-1} appeared, which is a Raman active mode of the metal-phase VO_2 [58].

We also performed a two-dimensional scan of an area of 60 × 60 μm^2 (150 ×150 points) around the conducting region (integration time = 0.5 seconds). We applied a sum filter which integrates the Raman signal intensity over a defined wavenumber range of interest and subtracts the background as a linear baseline from the minimum to the maximum value of the wavenumber range. The filter range selected was from 530 cm^{-1} to 700 cm^{-1} (indicated by the light gray region in Figure 2-4(a)) covering one of the characteristic Raman peaks of the insulator-phase VO_2 at 620 cm^{-1}. The resulting image is shown in Figure 2-4(b). We can see clearly the contrast of the Raman intensities inside and outside the conducting path; the darker the color, the lower the intensity sum. The Raman intensity distribution at the edge of the conducting path shows that there is a phase co-existence region. As a result, our assumption that the edge of the conducting path is abrupt made in calculating the resistivity (Figure 2-3(b)) is only approximate; nonetheless, the uncertainty is relatively small (~3 μm) compared to the total width of the conducting path (tens of microns).

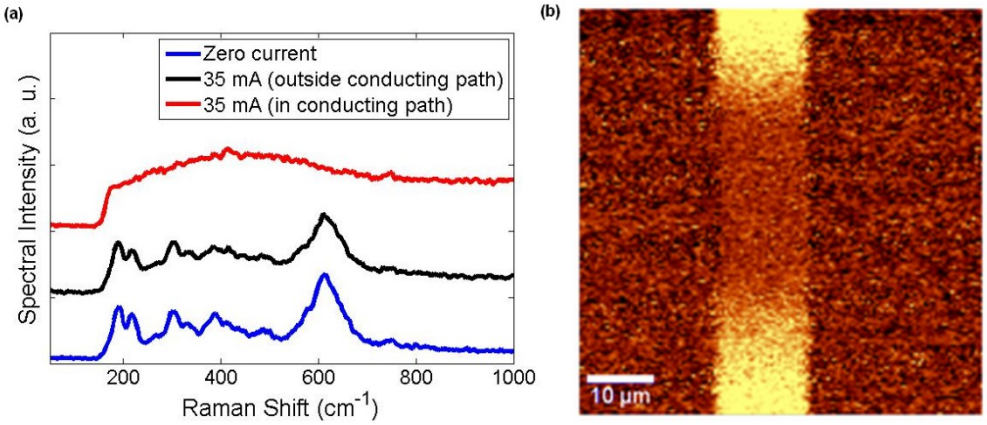

Figure 2-4 *(a) The blue curve is the Raman spectrum measured with zero applied current. The red and black curves are the Raman spectra measured with 35 mA applied current at the center of the conducting path and 50 μm away from the conducting path, respectively. (b) Plot of the sum of the Raman signal intensity integrated over the wavenumber range from 530 cm^{-1} to 700 cm^{-1} (light gray region in (a)) in an area (60 × 60 μm^2) around the conducting path; the darker the color, the lower the intensity sum.*

Since both the real and imaginary parts of the refractive index change drastically as VO_2 undergoes phase change [40], the optical properties are different in the conducting path region and outside of it. Figure 2-5 shows mid-infrared reflectance images acquired using an FTIR microscope with an FPA detector. The FPA detectors allow for the simultaneous acquisition of 64 by 64 spatially resolved spectra, with each pixel providing an independent infrared spectrum. With a 36X objective, each pixel corresponds to an area of 1.11 × 1.11 μm^2. The measurements were performed at two different currents (21 mA and 40 mA). Figure 2-5(a)-(c) show the reflectance spectra at each pixel integrated over the 2.86 to 2.94 μm and 8.33 to 10 μm regions. The resolution of each image is diffraction limited, so the smaller the wavelength, the better the resolution. All spectra were normalized to the reflectance of the gold electrodes. The conducting path is shown at the center of the images. The line scans are taken across the middle of the conducting path indicated by the black dashed lines. The reflectance intensity sum is higher in the conducting path than

outside of it. The width of the high-reflectance region increased with the current. This provides a way to dynamically control the optical properties of VO_2 locally and use it as a tunable optical device.

Figure 2-5(d) compares the reflectance at the center of (blue), at the edge of (green), and far away from (red) the conducting path (CP) as a function of wavelength. The positions are marked as the black crosses in (b). It can be seen that the reflectance decreases gradually from a value above 0.6 at the center of the conducting path to approximately 0.4 at the edge (10 μm away from the center) and finally to approximately 0.2 far away (23.3 μm from the center). The reflectance spectrum at the center of the conducting path increases slightly at longer wavelengths whereas the reflectance at the edge of and far away from the conducting path decreases the wavelength increases. This is consistent with the observations of the reflectance spectra of the same sample at temperatures above and below the transition temperature. The spikes at near 4.25 μm and 6.25 μm come from carbon dioxide and ambient water respectively which do not affect our analysis.

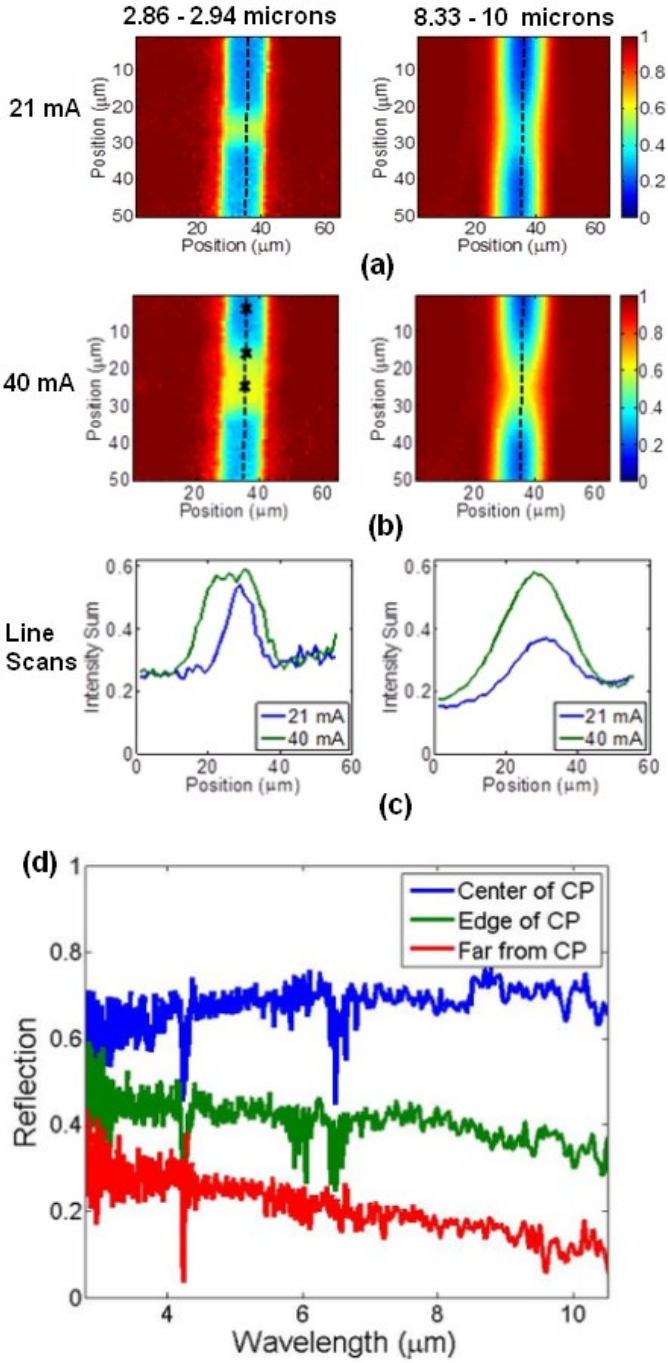

Figure 2-5 *(a) – (c) FTIR spectroscopy measurement at 21 mA and 40 mA. The reflectance spectra are integrated over the 2.86-2.94 μm (left) and 8.33-10 μm (right) wavelength regions. (a) and (b) are the maps of the reflectance distribution after integration and (c) is the corresponding line scans taken at the positions indicated by the black dashed lines. (d) Infrared spectrum at the center of (blue), 10 μm away from the center (green), and 23.3 μm away from (red) the conducting path (CP). The positions are shown as black crosses in (b) at 40 mA.*

Figure 2-6(a) and (b) show the reflectance spectra at different temperatures for the heating and cooling cycles respectively. The measurements were performed with Bruker Fourier transform infrared (FTIR) spectrometer with a Hyperion 3000 FTIR microscope. Above the T_C, VO_2 is in its metallic phase which has a high reflectance close to 0.6 whereas below the T_C, VO_2 is insulating which has a low reflectance of about 0.2 and it decreases as the wavelength increases. This observation is consistent with Figure 2-5(d). The close-to-zero reflectance point at about 11.6 μm is a result of critical coupling between the device layers and is used as the perfect absorber condition discussed in ref. [35]. Unfortunately, our Focal Plane Array detector has a limited spectral range, so this feature is not captured in Figure 2-5.

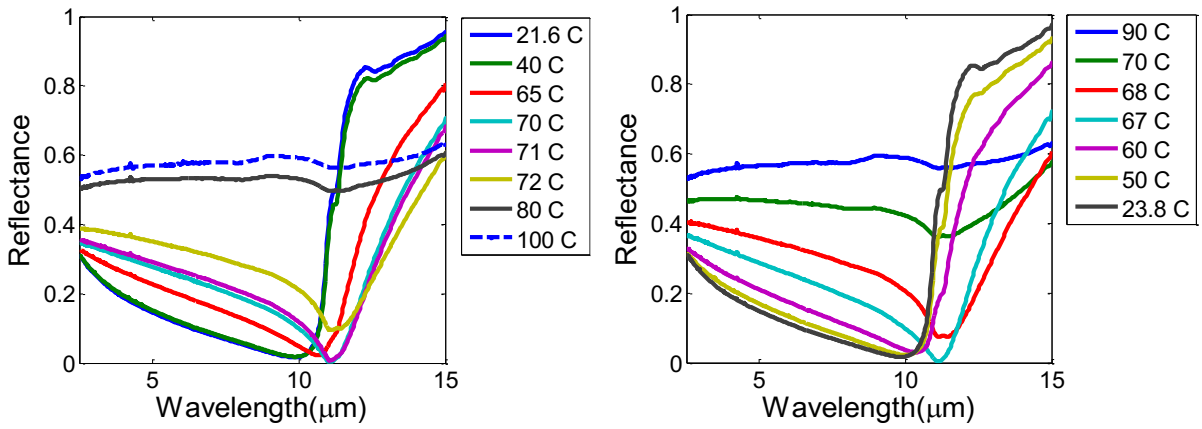

Figure 2-6 *Reflectance spectra at different temperatures during the heating cycle (a) and the cooling cycle (b).*

2.2 Reconfigurable metasurface devices based on temperature-modulated phase transition of VO_2

Tunable optical metamaterials and metasurfaces are an emerging frontier with promising applications including optical modulation, routing, dynamic beam shaping, and adaptive optics [59]–[62]. Dynamic control in meta-devices can be achieved by careful integration of existing

designs with active media, for example, liquid crystals [63], [64], graphene [62], or strongly electron-correlated [65], [66] and chalcogenide [67] phase-transition materials. Phase-transition materials featuring various structural and electronic transitions such as germanium antimony tellurium (GST) [66]–[68], vanadium dioxide (VO_2) [65], [69], and rare-earth nickelates [70] have particular promise because of their large change of optical properties given an applied stimulus compared to, for example, Kerr materials [71] or liquid crystals [63], [64], [72]. Of the phase-transition materials, one of the most prolifically studied is VO_2, which exhibits a reversible insulator-metal transition (IMT) as the temperature reaches a critical temperature $T_C \sim 67$ °C [69]. This transition, which takes VO_2 from its low-temperature insulating monoclinic phase to the high-temperature metallic rutile phase, corresponds to a resistivity change of up to five orders of magnitude and a dramatic change in the complex refractive index, especially at infrared (IR) wavelengths [73]. Here we describe how ion beam irradiation can be used to modify and engineer the thermally driven IMT of vanadium dioxide via the intentional creation of structural defects and lattice damage ("defect engineering"). Unlike existing means to modify the IMT via doping during growth [74], ion beam irradiation can be combined with lithographic patterning to create complex optical meta-devices with designer phase transitions (Figure 2-7).

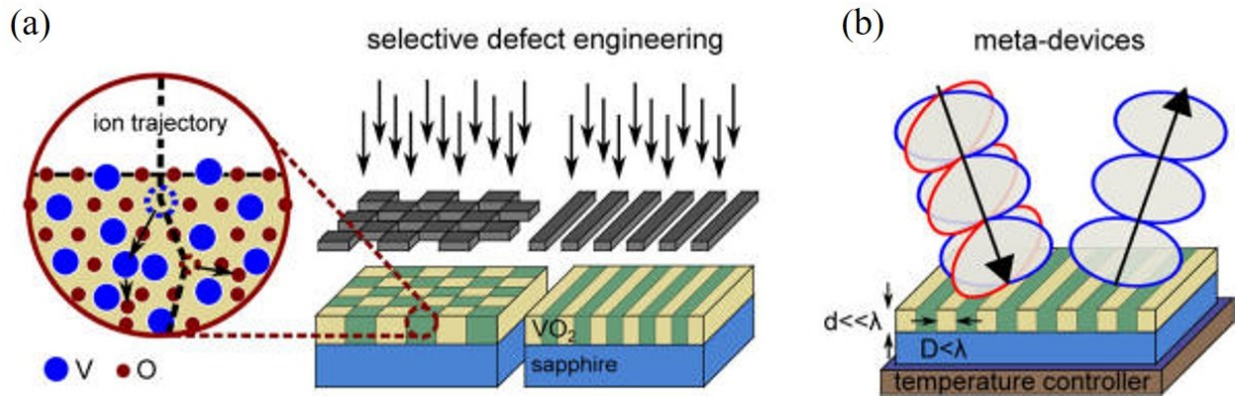

Figure 2-7 *Optical meta-devices based on defect engineering of phase-transition materials. (a) The thermally driven insulator-to-metal phase transition of vanadium dioxide (VO_2) can be modified by deliberately introducing structural defects into the lattice (defect engineering). Spatially selective defect engineering is achieved by ion beam irradiation through a mask. The enlarged area shows the primary displacement of both vanadium and oxygen lattice atoms by an incoming energetic ion and the subsequent damage cascade. The complex refractive indices of the insulating and metallic states are similar for the intrinsic and irradiated VO_2, but the phase transition of the irradiated regions occurs at a much lower temperature. (b) The irradiated features can be made much smaller than the wavelength of light, so the resulting film becomes a metasurface with effective optical properties. One example is a tunable polarizer comprising stripes of irradiated and intrinsic VO_2, creating a metasurface with a variable degree of optical anisotropy.*

Vanadium dioxide (VO_2) thin films with a thickness of ~ 100 nm were grown on double-side polished c-plane sapphire substrates using rf magnetron sputtering from a V_2O_5 target. During growth, the temperature, pressure and the Ar gas flow were maintained at 550 °C or 450 °C, 5 mTorr, and 40 sccm leading to phase pure crystalline films with few structural defects, which was confirmed by X-ray diffraction measurements and Rutherford backscattering spectrometry (RBS) (see Appendix A3). The VO_2 films consist of highly oriented epitaxial domains with the [010] direction normal to the substrate surface and three-fold in-plane rotational symmetry. The domain size varies between 20 – 100 nm as measured by atomic force microscopy (see Appendix A4).

The insulating phase of VO_2 is a Mott-Peierls insulator with both electron-electron correlations and dimerization of vanadium ions contributing to the opening of an insulating gap [75]. Thus, the IMT is very sensitive to the stability of the electron hybridization and therefore to electronic doping [74], structural defects [76], and lattice strain [77]–[79], all of which can be introduced via ion beam irradiation. The VO_2 thin films were irradiated with 75 keV Ar^+ or 190 keV Cs^+ ions at room temperature in a fluence range starting from $N_I = 5x10^{12}$ to $N_I = 1x10^{15}$ cm^{-2}. To compare the irradiation effects on the IMT induced by the same amount of lattice defects, we estimated the fraction of atoms that have been displaced by the incoming ions (number of primary displacements per lattice atom) n_{dpa} using Stopping and Range of Ions in Matter (SRIM) code. For this purpose, the depth distribution of primary displacements was calculated with SRIM for both ion species. The calculations indicate that the maximum number of displacements per ion is ~ 3 times higher for 190 keV Cs^+ irradiation of VO_2: $N_I/n_{dpa} \sim 2.1 \times 10^{14}$ cm^{-2} compared to 75 keV Ar^+: $N_I/n_{dpa} \sim 6.7 \times 10^{14}$ cm^{-2}. Area-selective irradiation was achieved by covering the samples with an e- beam patterned PMMA masks prior to ion irradiation. The thickness of each mask was 300 nm, sufficient to stop all ions in the covered regions.

To investigate the effect of the irradiation on the optical properties, we performed temperature-dependent near-infrared transmittance measurements (λ = 2.5 μm) of intrinsic and irradiated VO_2 films (Figure 2-8). The highly oriented epitaxial VO_2 films were grown to a thickness of ~100 nm on c-plane sapphire and then irradiated with varying fluences of 75 keV Ar^+ ions, corresponding to a Gaussian depth profile centered at the middle of the film (see Appendix A). Argon was chosen because it is a noble gas and is thus not chemically incorporated in the VO_2 lattice, enabling the study of the effects of irradiation-induced lattice defects separate from any

impurity doping. The transmittance of all films decreased with increasing temperature (Figure 2-8(a)), a result of increasing free carrier concentration during the transition from the insulating to the metallic state and displayed a hysteresis loop that is characteristic of a first-order phase transition [80]. We calculated the critical temperature T_C of the IMT as the average of the temperatures of the largest slope of the transmittance versus temperature curves for the heating and cooling cycles, respectively [81].

Temperature-dependent optical transmission measurements were performed at a wavelength of 2.5 μm using a halogen lamp attached to a Shamrock 500 monochromator. The transmitted light was detected with a PbSe detector. The reflectance of the patterned samples in the mid-IR wavelength range was investigated via near-normal incidence measurements using a mid-infrared microscope Hyperion 2000 with a Cassegrain objective (NA = 0.4) attached to a Fourier transform infrared (FTIR) spectrometer (Bruker Vertex 70). All spectra were collected in the middle of the respective pattern on an area of 50 x 50 μm^2 while gradually increasing/decreasing the sample temperature in the range between 25°C and 100°C at 1°C increments.

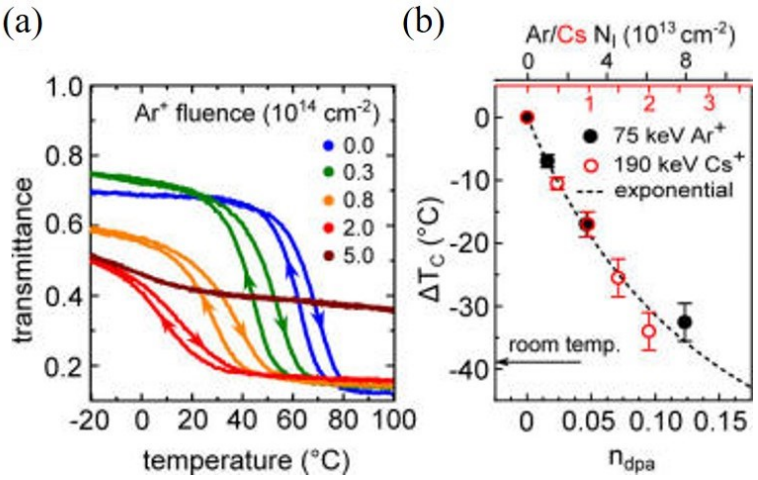

Figure 2-8 *Defect engineering via ion beam irradiation. (a) Temperature-dependent transmittance (λ = 2.5 μm) of a 100 nm VO_2 film on* c*-plane sapphire irradiated with 75 keV Ar^+ ions for various ion fluences. The arrows mark the heating and cooling branches of the hysteresis curves. (b) Experimentally determined shift of the phase transition temperature (ΔT_C) versus the calculated* n_{dpa}*, given irradiation with 75 keV Ar^+ and 190 keV Cs^+ ions. The energy, mass, and fluence of the ion irradiation determine the* n_{dpa}*. The data points for Ar^+ and Cs^+ fall on the same curve and, because argon is not incorporated into the VO_2 lattice, we conclude that the shift of the critical temperature is a result of lattice defects induced by ion irradiation and is not caused by impurity doping. The exponential curve is a common fit to both sets of points using a direct impact damage formation model.*

When the films were irradiated with an increasing Ar^+ ion fluence N_I (number of ions per unit area), the transition temperature decreased, reaching room temperature for $N_I \sim 1 \times 10^{14}$ cm^{-2} (Figure 2-8(a) and (b)). This effect is a result of irradiation damage, that is, the displacements of both oxygen and vanadium from their lattice sites by nuclear collisions that lead to the formation of stable interstitial-vacancy complexes (Frenkel pairs) at low ion fluences [82], reducing T_C via the local compressive strain [77], [78] induced in the lattice by atomic displacements [83]. We attribute the broadening of the transition width for increasing ion fluences to the Gaussian depth distribution of lattice defects, and the reduction of transmittance in the insulating state (Figure 2-8(a)) to absorption within the band gap resulting from the increasing number of defect states. For

the highest ion fluences (>5 × 10^{14} cm^{-2}), the accumulation of point defects leads to the formation of amorphous regions of VO_2 that overlap until a continuous amorphous VO_2 film is formed (see Appendix A3). For a comparable shift of T_C to room temperature by ion beam impurity doping with tungsten, the most efficient dopant [74], $N_I \sim 10^{16}$ cm^{-2} would be necessary, far above the amorphization threshold. Amorphous films of VO_2 do not feature an IMT [84].

To confirm that the shift of T_C (ΔT_C) is caused by irradiation damage rather than impurity doping or stress from the impurity atoms themselves, we repeated the experiment with 190 keV Cs^+ ions, which have a much larger atomic number and ionic radius (Figure 2-8(b)). The energy was chosen to ensure an implantation profile comparable to that of the Ar^+ irradiation (see Appendix A). To compare ΔT_C induced by the same density of lattice defects due to Ar^+ and Cs^+ ion irradiation, respectively, we estimated the fraction of atoms that have been displaced by the incoming ions (number of primary displacements per lattice atom, n_{dpa}). The reflectance of each region was measured in the 2 - 15 μm wavelength range for increasing temperatures (25 °C to 100 °C in steps of 1 °C). In agreement with ref. [11], the reflectance changes non-monotonically as a function of temperature, with a minimum-reflectivity point near (but slightly below) T_c at $\lambda =$ 11.3 μm, which is a result of the complex interplay between the intermediate state of VO_2 and the underlying substrate (Figure 2-9). For the irradiated regions of VO_2, the temperature of the intermediate state is decreased, but all the reflectance curves display the same shape as those of intrinsic VO_2 (Figure 2-9(b) and (c)), indicating that the ion irradiation does not fundamentally alter the optical properties of VO_2 across the phase transition. The temperature at which the reflectance minimum occurs is 70°C for intrinsic VO_2, and 55, 43 and 32 °C for irradiated VO_2 with n_{dpa} = 0.02, 0.05 and 0.09, respectively. T_C is found to be roughly independent of the ion

species, depending only on ndpa, and reaches room temperature when less than ~15% of all lattice atoms are displaced (Figure 2-8(b)). The irradiation defects are stable in the temperature range investigated in this work and remain unaltered after many cycles through the IMT. Thus, we can conclude that defect engineering using ion irradiation with various ions can be used to broadly tune the critical temperature of the IMT.

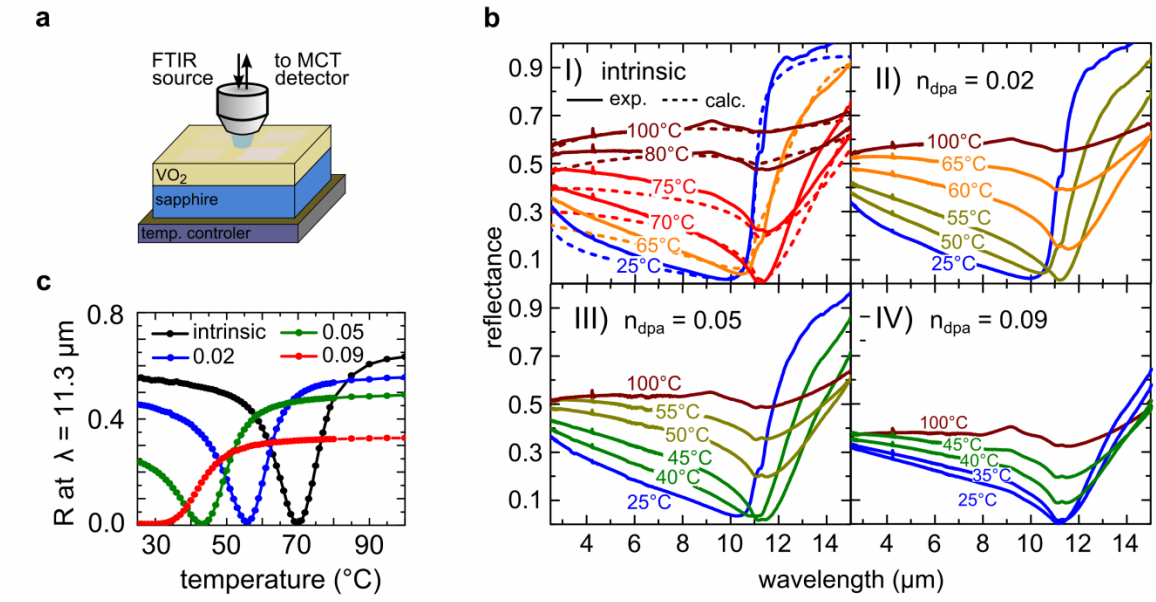

Figure 2-9 *(a) Schematic drawing of the near-normal incidence reflectance measurement setup using an IR microscope and a temperature controlled stage. (b) Effect of Cs^+ ion irradiation on the temperature dependent reflectance of a 100 nm VO_2 thin film on c-Al_2O_3 for ion fluences up to* $N_I = 2\times10^{13}$ *cm^{-2} corresponding to* $n_{dpa} = 0.09$*. At a critical temperature, the reflectance drops to almost zero at* $\lambda = 11.3$ *μm for all samples. Calculated reflectance curves for intrinsic VO_2 using Fresnel Equations and our effective medium approximation are given in dashed lines. (c) Measured reflectance for different ion fluences at* $\lambda = 11.3$ *μm as a function of increasing temperature. The critical temperature at which the sample shows minimal reflectance decreases with increasing ion fluence, reaching room temperature for the highest fluence.*

The IMT in VO_2 is particularly useful for tunable optical and optoelectronic devices because it occurs gradually over a range of temperatures and provides access to a wide range of complex refractive index values. At the onset of the IMT, nanoscale islands of the metallic phase start to nucleate surrounded by insulating VO_2, which then grow and connect in a percolation process [41]. Because of this phase coexistence on a subwavelength scale, VO_2 in its transition region has been described as a natural disordered optical metamaterial [39]. A similar gradual refractive index change can be observed in GST [84]. However, it has been noted that the intrinsic transition temperature of VO_2 limits the utility of this material for devices. Now using area-selective defect engineering with ion fluences significantly smaller than the amorphization threshold of VO_2, we can obtain control over the shape, temperature, and persistence of the phase coexistence regions by selectively irradiating appropriate regions of the VO_2 film, locally modifying the IMT (Figure 2-7 [84]). In the temperature range where irradiated VO_2 regions are metallic while the intrinsic regions are insulating, persistent phase coexistence of metallic and insulating domains with a fixed metallic fraction is artificially induced.

To calculate the theoretical infrared reflectance of our samples, we consider light incident from air ($\tilde{n}_1 = 1$) onto the VO_2 film with thickness d and temperature dependent complex refractive index $\tilde{n}_2(T) = n_2(T) + ik_2(T)$, which is deposited on a sapphire substrate with a temperature-independent index of $\tilde{n}_3 = n_3 + ik_2$. The reflectance is given by $R = |r|^2$ where

$$r = \frac{r_{1,2} + r_{2,3}e^{2i\delta}}{1 + r_{1,2}r_{2,3}e^{2i\delta}}, \qquad (2)$$

$r_{k,l} = (\tilde{n}_k - \tilde{n}_l)/(\tilde{n}_k + \tilde{n}_l)$ are the Fresnel reflection coefficients for normal incidence as the wave encounters medium l from medium k, $\tilde{n}_{k,l}$ are the complex refractive indices of medium k

and l, respectively, and $\delta = \frac{2\pi}{\lambda} d\, \tilde{n}_2(T)$ is the complex phase shift [38] due to the wave passing through the VO_2 film.

In the vicinity of the phase transition of VO_2, as the temperature is increased, islands of the metallic phase begin to nucleate and grow in the insulating VO_2 film until the film is entirely in the metallic phase. Thus, VO_2 during its transition can be described as an inhomogeneous composite medium composed of metallic and insulating domains that are much smaller than the wavelength of the incident light. The optical properties of such a system can be estimated by effective medium approximations (EMAs), which predict the effective dielectric constant of the composite medium in terms of dielectric constants and volume fractions of its constituent components [85]. Here we use the Bruggeman formalism [86] with a definition of the depolarization factors that were introduced by Polder and van Santen [87]. For a mixture of two isotropic constituents with bulk dielectric functions $\tilde{\epsilon}_1$ and $\tilde{\epsilon}_2$ (here insulating and metallic VO_2, experimentally obtained by spectroscopic ellipsometry [41], the effective dielectric function $\tilde{\epsilon}_{eff,a}$ along the directions $a = x, y$ and z is given by the Bruggeman Equation [88]:

$$f_1 \frac{\tilde{\epsilon}_1 - \tilde{\epsilon}_{eff,a}}{\tilde{\epsilon}_{eff,a} + q_a(\tilde{\epsilon}_1 - \tilde{\epsilon}_{eff,a})} + f_2 \frac{\tilde{\epsilon}_2 - \tilde{\epsilon}_{eff,a}}{\tilde{\epsilon}_{eff,a} + q_a(\tilde{\epsilon}_2 - \tilde{\epsilon}_{eff,a})} = 0, \qquad (3)$$

where f_1 and f_2 are the volume fractions of component 1 and 2, respectively. In general, the inclusions are modeled as ellipsoids, where q_a is the depolarization factor of the ellipsoid along the a direction, which can be calculated as [88]:

$$q_a = \frac{xyz}{2} \int_0^\infty \frac{ds}{(s+a^2)\sqrt{(s+x^2)(s+y^2)(s+z^2)}}. \qquad (4)$$

The three depolarization factors have to satisfy $q_x + q_y + q_z = 1$ and are linked to the structure of the inclusions. For example, spherical inclusions can be modeled with $q_x = q_y = q_z = 1/3$, whereas

for disk-like inclusions the depolarization factor orthogonal to the disk is zero and the in-plane depolarization factors are $q_x = q_y = 1/2$.

Following the arguments of ref. [41] for VO_2 thin films, the isotropic in-plane depolarization factor is taken to be 0.2-0.4 assuming nearly spherical metallic inclusions of the emerging metallic phase for low metallic fractions $f = f_2$ ($f_1 = 1 - f$).With increasing f, the depolarization factor continuously increases to 0.5 (thin flat disks) because the out-of-plane dimension of the metallic inclusions is limited by the film thickness. We used a depolarization factor $q(f)$ as given in Figure 2-10(a).

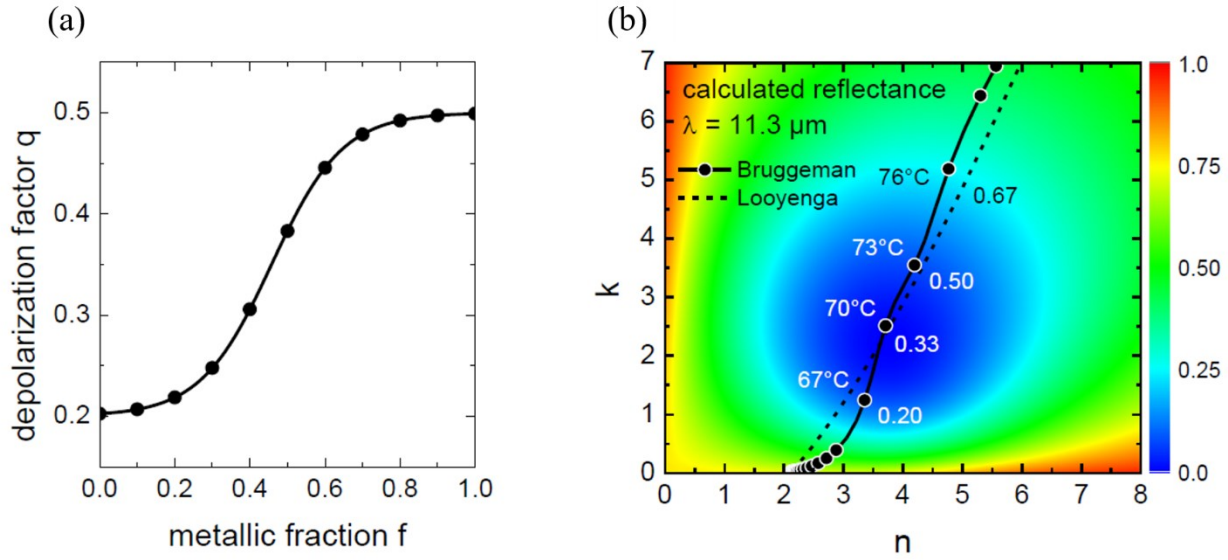

Figure 2-10 *(a) Depolarization factor* q *as a function of the metallic fraction* f *that was used in Bruggeman's Equation to approximate the effective dielectric function of intrinsic VO_2 across the phase transition. b, Calculated map of the reflectance at λ = 11.3 μm as a function of the real and imaginary part of the complex refractive index $\tilde{n} = n + ik$ of an arbitrary 100 nm thin dielectric film on sapphire. The black line marks the trajectory of the calculated complex refractive index of VO_2 obtained by Bruggemann's mixing rule using the depolarization factors from (a). The black dashed line marks the calculated index paths obtained by Looyenga's mixing rule. Selected temperatures and corresponding metallic fractions f are labeled.*

The phase co-existence in VO_2 can be empirically considered as a first-order equilibrium [89] and hence the metallic fraction can be estimated:

$$f(T) = \frac{1}{1+exp\left[{}^{W}/_{k_B}\left({}^{1}/_{T} - {}^{1}/_{T_{1/2}}\right)\right]}, \quad (5)$$

where W is an energy scale for the IMT which contains information about the total width (sharpness) of the IMT, and $T_{1/2}$ is the temperature at which half of the VO_2 is in the metallic state.

Using Equation (5), we were able to fit the calculated reflectance in the mid-IR simultaneously to our experimental data of intrinsic VO_2 at all temperatures (in total 76 data sets) by independently varying only the two free parameters: $T_{1/2}$ and W. The best fit using W = 2.4 eV and $T_{1/2}$ = 73 °C agrees well with all reflectance spectra across the IMT over the entire spectral region (Figure 2-9(b), Equation (2)). The metallic fraction at the point of minimal reflectance is ~ 0.33. This means that minimal reflection at a given wavelength occurs at a fixed metallic fraction during the IMT, but not necessarily at T_C or $T_{1/2}$.

We calculated the reflectance of a 100 nm thick arbitrary film on a sapphire substrate at a wavelength of $\lambda = 11.3\ \mu$m for a range of potential complex refractive indices $\tilde{n} = n + ik = \sqrt{\tilde{\epsilon}}$ of this film using Equation (2) (color map in Figure 2-10(b)). The complex refractive index of sapphire was taken to be ~0.1 + 0.5i at this wavelength [90]. The calculated reflectance goes to zero for $\tilde{n}$ = 3.8 + 2.2i, corresponding to a critical coupling condition [11].

We calculated the complex refractive index of intrinsic VO_2 using Equations (3)-(5) for different temperatures (metallic fractions) across the IMT. We the same $T_{1/2}$ = 73°C and W = 2.4 eV as above as well as refractive indices of insulating and metallic VO_2 of $\tilde{n}_{ins}$ = ~2.1 + 0.02i and $\tilde{n}_{met}$ = ~6.9 + 9.2i, respectively [41]. The calculation shows that during the phase

transition the effective refractive indices of the VO_2 at λ = 11.3 μm almost cross the point of perfect absorption. The predicted reflectance minimum ~0.003 at a temperature of T_{min} ~ 69°C for intrinsic VO_2 is in agreement with the experimental data, which showed a minimum value of 0.005 at 70°C (Figure 2-9(b) and (c) and 2-11). The metallic fraction at the point of minimal reflectance is ~ 0.33.

An alternative approximation of the effective optical properties of intrinsic VO_2 in the vicinity of the phase transition can be obtained using Lichteneckers mixing rule with the exponent *k* being 1/3 (consistent with Looyengas mixing rule [91]):

$$\tilde{\epsilon}_{eff}{}^{k} = (1-f)\tilde{\epsilon}_1^k + f\,\tilde{\epsilon}_2^k, \qquad (6)$$

where $\tilde{\epsilon}_1$ and $\tilde{\epsilon}_2$ are the dielectric functions of insulating and metallic VO_2, respectively, *f* is the metallic fraction and *k* is an exponent that describes the anisotropy of the compound.

Lichteneckers mixing rule is based on the Wiener theory for bounds of the effective dielectric function of a two-phase composite. According to Lichtenecker the dielectric function for any composite must satisfy Equation (6) with k varying within the [-1,1] range. The upper bound for this effective dielectric function is reached in a system consisting of plane-parallel layers disposed along the field. The lower bound is reached in a similar system, but with the layers perpendicular to the field [92]. Applied to isotropic composites (k = 0) Lichteneckers Equation reads:

$$log\,(\tilde{\epsilon}_{eff}) = (1-f)log\,(\tilde{\epsilon}_1) + f\,log\,(\tilde{\epsilon}_2). \qquad (7)$$

We fabricated a sample composed of defect-engineered and intrinsic VO_2 regions in a square checkerboard arrangement (period = 0.5 μm) by irradiating a 100 nm VO_2 film on c-plane sapphire with 190 keV Cs^+ through a PMMA mask made using electron-beam lithography (Figure

2-7(a) and 2-11(a)). The ion fluence was set to $N_I = 1 \times 10^{13}$ cm^{-2}, which corresponds to n_{dpa} = 0.05 (i.e. 5% of all lattice atoms are displaced), and decreases T_C of the irradiated region to ~50 °C (Figure 2-8(b)). We probed the temperature-dependent effective optical properties of this sample via mid-IR reflectance measurements using a FTIR spectrometer and a mid-IR microscope (Figure 2-11). The mid-IR was chosen because the carrier concentration change due to the IMT leads to greater changes of the refractive index compared to the visible and near-infrared. E-beam lithography (Raith 150TWO and Elionix ELS F-125) was employed to cover at least 100 x 100 μm^2 areas of the VO_2 thin films with PMMA masks. The mask consisting of parallel ridges with a width of 0.5 μm and a period of 1 μm was fabricated in the FIXED-BEAM-MOVING-STAGE mode. This method guarantees continuous ridges without any offset. The checkerboard mask is composed of squares with a period of 0.5 μm. Various area coverages D were realized by keeping the period constant and changing either the ridge width or the edge length of the squares. After ion irradiation, the PMMA mask was lifted-off with dimethyl sulfoxide in an ultrasonic bath for 30 min.

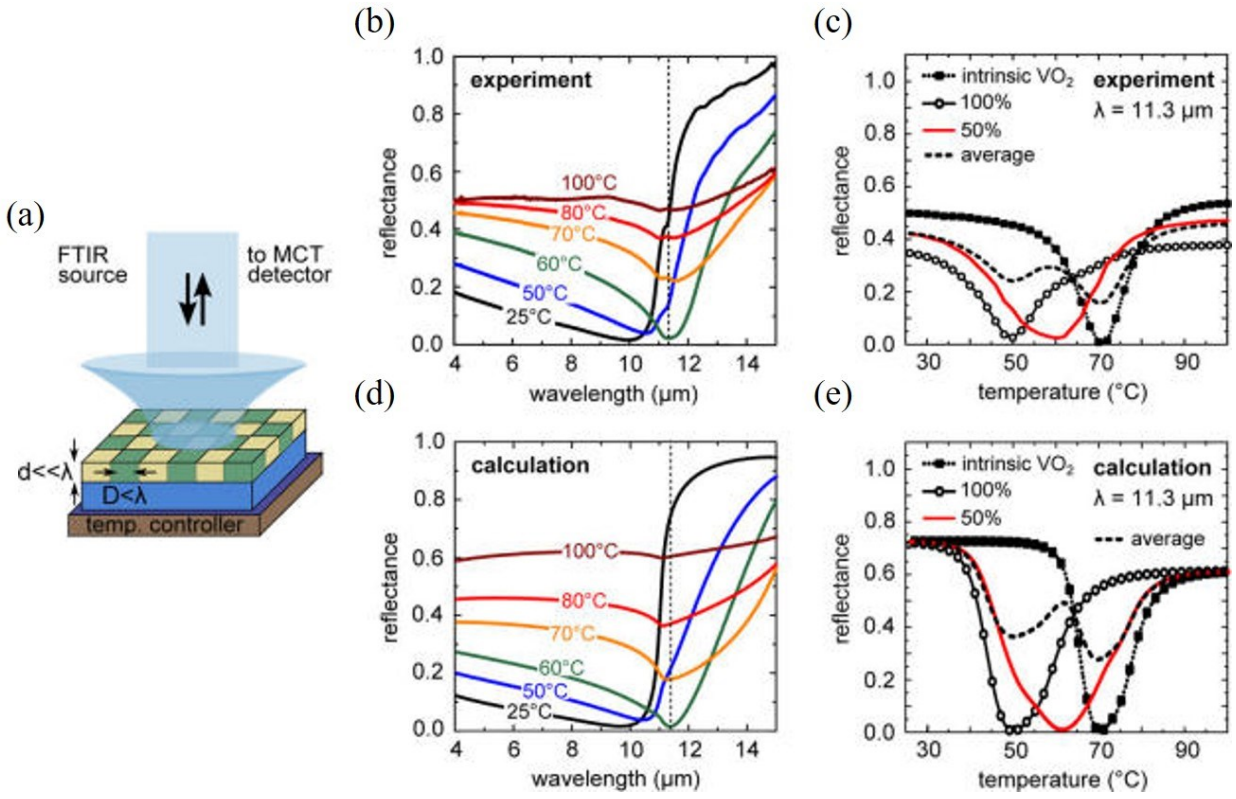

Figure 2-11 *Artificially induced persistent phase coexistence. (a) Schematic drawing of the near-normal incidence reflectance measurement using an infrared microscope and a temperature-controlled stage. (b) Temperature-dependent reflectance of the checkerboard structure (area coverage D = 50%, period = 500 nm, film thickness = 100 nm). At a critical temperature, the reflectance of the sample drops to almost zero for λ = 11.3 μm due to an ultrathin film interference interaction between the film and the substrate.35 (c) Measured reflectance of intrinsic, checkerboard structure (D = 50%), and completely irradiated (D = 100%) films at λ = 11.3 μm. The subwavelength checkerboard structure possesses effective optical properties that cannot be trivially deduced by averaging the reflectance of the intrinsic and fully irradiated samples (dashed line) and appears to have a single broadened phase transition. (d,e) Calculated reflectance for the sample measured in (b,c) using Fresnel Equations and our effective medium approximation.*

At low temperatures, both the irradiated and intrinsic VO_2 regions are insulating and essentially transparent. The reflectance spectrum is dominated by the onset of a prominent Reststrahlen band of the sapphire substrate, leading to high reflectivity above ~11 μm. As the temperature T is increased, the mid-IR reflectance changes monotonically in the 4−10 μm region

and non-monotonically in the 10−15 μm region, reaching a minimum-reflectance point at λ = 11.3 μm and T_{min} = 60 °C. Such a reflectance minimum is also found in the vicinity (~3 °C below) of the phase transition at a metallic fraction of ~33% in intrinsic and fully irradiated samples (Figure 2-11(c)) and is a result of an 'ultrathin-film interference condition' found in highly absorbing films on certain reflective substrates [11]. Note that for sapphire, the wavelength at which this reflectance minimum appears is fixed to a relatively narrow range within the Reststrahlen band, where the complex refractive index is similar to that of metals at visible or UV frequencies and can be tuned slightly by the film thickness. Comparable complex refractive indices can also be found in a variety of other substrates in the visible and mid-IR, for instance, highly doped semiconductors and transparent conducting oxides [39].

In particular, the reflectance of the sample at λ = 11.3 μm as a function of temperature (Figure 2-11(c)) shows that the subwavelength checkerboard structure possesses effective optical properties that cannot be trivially deduced by averaging the reflectance of the intrinsic and fully irradiated samples. While the reflectance minimum of irradiated and intrinsic VO_2 regions occurs independently at ~50 and ~70 °C and has a full width at half-minimum (FWHM) of ~15 and ~12 °C, respectively, the subwavelength checkerboard appears to have a single effective reflectance minimum at ~60 °C with an FWHM >25 °C.

Due to the subwavelength nature of the checkerboard ('check') pattern features, we can treat the patterned VO_2 film as an effective medium that has a well-defined temperature- and wavelength-dependent complex refractive index:

$$\tilde{n}_{eff}^{check}(T) = \sqrt{\tilde{n}_{int}(T)\tilde{n}_{irr}(T)}\,, \qquad (8)$$

where $\tilde{n}_{int}(T)$ and $\tilde{n}_{irr}(T)$ are the temperature-dependent refractive indices of intrinsic and irradiated VO_2 regions, calculated from the refractive indices of insulating and metallic VO_2, extracted from the measurements of Quazilbash et al. [41] using the Bruggeman equations. Taking into account the effective optical constants, we used Fresnel Equations to calculate the reflectance of the samples (Figure 2-11(d) and (e)), which are in agreement with the measurements. Differing absolute reflectance values are most likely due to a different optical quality of our initial films compared to the film measured in reference [15], and an increasing amount of lattice defects with increasing ion fluence for the irradiated films.

Our results show that the temperature range of phase coexistence can be greatly increased by patterned ion irradiation because the metallic fraction will remain roughly constant in the temperature range between the transition temperatures of the irradiated and intrinsic VO_2 regions (e.g., between 50 and 70 °C in Figure 2-11(c)). Furthermore, the metallic fraction can be adjusted by changing D. The optical properties can then be tuned in and out of an artificially designed effective medium state over a desired range of temperatures. We note that a vertical (rather than lateral) distribution of phase transition temperatures has been achieved in thin VO_2 films synthesized from colloidal VO_x nanocrystal solutions with various tungsten doping densities [93].

Further functionality can be achieved by realizing VO_2-based anisotropic metasurfaces with tunable dichroism. Anisotropic phase coexistence in thin VO_2 films has been observed on TiO_2 substrates and occurs naturally due to strain [94] but requires particular substrates and provides little control over the degree of anisotropy. Similar phase coexistence was also achieved by selective laser heating of embedded VO_2 nanoparticles, though this structure is not temperature tunable [95].

One requirement for the applicability of defect engineering of VO_2 and other phase-change materials for meta-devices is the stability of the defects. Figure 2-12(a) shows the transmittance ($\lambda = 2.5\ \mu m$) as a function of temperature for a VO_2 sample irradiated with 75 keV Ar^+ ions to $N_I = 0.8 \times 10^{14}$ cm^{-2} and subsequently thermally cycled through its IMT. We observed no transmittance change multiple cycles indicating that all defects are stable up to at least 100°C.

An extensive thermal stability test was performed with the checkerboard sample used and described in Figure 2-11. The sample was repeatedly cycled through the IMT in the temperature range from 30°C to 100°C with a heating and cooling rate of ~ 0.5°C/min, respectively. We measured the temperature-dependent reflectance at 11.3 μm (Figure 2-11(c)) before cycling, and after 200 and 400 cycles (Figure 2-12(b)). Although the absolute reflectance values differ slightly, predominantly caused by different placement of the sample under the IR microscope, the minimum-reflectance point at λ = 11.3 μm remains constant at T ~ 60 °C, indicating good thermal stability of the checkerboard patterned sample.

We did not perform higher-temperature studies of the samples used for this manuscript to ensure that they remain in their original condition. However, we explored annealing on additional irradiated samples. VO_2 thin films with T_C ~ 71 °C were irradiated in order to decrease T_C to ~56 °C and subsequent annealing studies to higher temperatures were performed in air. Annealing to 150 °C and 200 °C increased T_C to ~58 °C and ~62°C, respectively, for the irradiated samples. This indicates that while some of the defects were annealed out, most remained stable up to 150 - 175 °C.

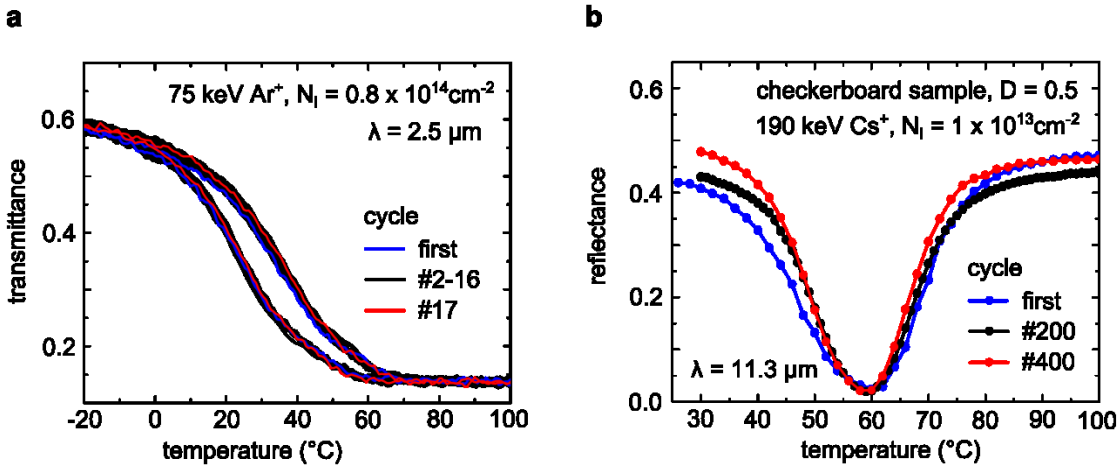

Figure 2-12 *(a) Temperature-dependent transmittance measured at λ = 2.5 μm for a 100 nm VO_2 film on sapphire entirely irradiated with 75 keV Ar^+ ions at* $N_I = 0.8 \times 10^{14}$ *cm^{-2}. The sample was cycled through the IMT from -50 to 100°C for 17 times without noticeable transmittances change. (b) Temperature-dependent reflectance measurement for the checkerboard patterned sample described in Figures 1a and 3a. The sample was cycled through the IMT from 30 to 100°C for 400 times. Although the absolute reflectance values slightly differ, the minimum-reflectance point at λ = 11.3 μm remains constant at* T ~ 60 °C, *indicating good thermal stability of the checkerboard patterned sample in the measured temperature region.*

We fabricated a periodic structure consisting of parallel ridges with a width of 0.5 μm and a period of 1 μm by irradiating a suitably masked sample with 190 keV Cs^+ ions at a fluence of $N_I = 2 \times 10^{13}cm^{-2}$, corresponding to $n_{dpa} = 0.09$ (compare also Figure 2-7(a)). At a temperature where only the irradiated VO_2 is metallic, the reflectance from the patterned region is polarization-dependent over most of the λ = 2−15 μm wavelength region, indicating a large degree of dichroism (Figure 2-13(a) and (b)). Especially at the wavelength at which minimal reflection occurs (λ = 11 μm in Figure 2-13(a)), light polarized parallel to the ridges ($E_\parallel$) is preferentially absorbed.

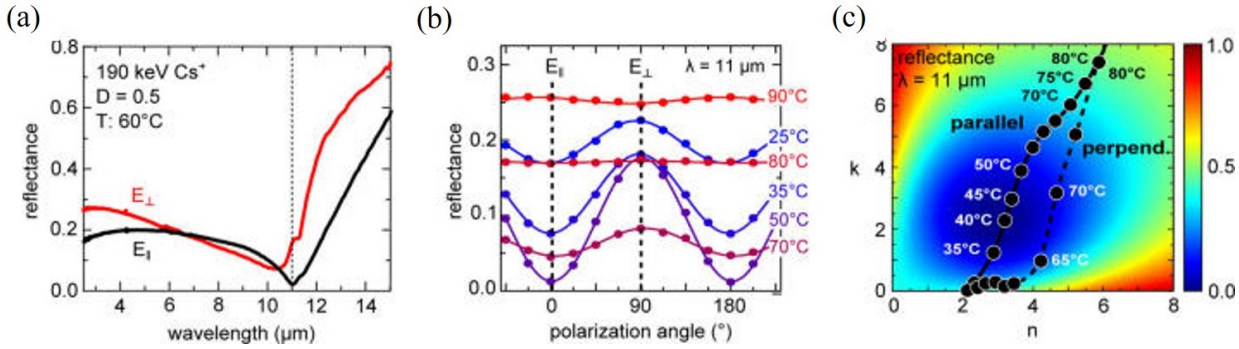

Figure 2-13 *Switchable polarizer via tunable anisotropy. (a) Measured reflectance of the anisotropic metasurface shown in Figure 1b, comprised of stripes of irradiated and intrinsic VO_2 (film thickness = 100 nm, D = 50%, period = 1000 nm) on a sapphire substrate. The sample temperature was maintained at 60 °C, between the transition temperatures of the intrinsic and irradiated VO_2, for light polarized parallel ($E_{\parallel}$) and perpendicular ($E_{\perp}$) to the ridges. Light polarized parallel to the ridges is preferentially absorbed at $\lambda \sim 11$ μm. (b) Evolution of the polarization-dependent reflectance at $\lambda = 11$ μm for increasing temperatures between 25 and 90 °C. (c) Calculated map of the reflectance at $\lambda = 11$ μm as a function of the real and imaginary part of the complex refractive index $\tilde{n} = n + ik$ of an arbitrary 100 nm film on sapphire. The lamellar grid pattern is equivalent to a uniaxial crystal with form birefringence and dichroism. The solid (dashed) line marks the calculated temperature-dependent complex refractive index of a patterned VO_2 film for light that is polarized parallel (perpendicular) to the ridges.*

Figure 2-13(b) shows the measured polarization-dependent reflectance at $\lambda = 11$ μm as a function of increasing temperature. The reflectance is small from 40 to 70 °C for light polarized parallel to the ridges ($E_{\parallel}$), and a value of $R_{\parallel} \sim 0.01$ is reached at T ~ 50 °C. At the same temperature, the reflectance for the orthogonal polarization is $R_{\perp} = 0.17$. As a consequence, unpolarized light reflected from the patterned VO_2 film becomes highly polarized with a degree of linear polarization (DOLP) of ~90%, defined as the intensity of light reflected with the preferential polarization minus the intensity of light reflected perpendicular to it divided by the sum of both. The polarization dependence vanishes above 75 °C, as both regions become metallic. Therefore, our device can be tuned in and out of the highly polarizing state by tuning the temperature.

To better understand the temperature- and polarization dependent reflectance, we calculated the reflectance of a 100 nm thick anisotropically patterned VO_2 film on sapphire for normally incident light that is polarized parallel (∥) or perpendicular to the ridges (⊥), respectively. When the wavelength is large enough, the refractive indices for a periodic structure consisting of ridges can be expressed as

$$\tilde{n}_{\parallel}^{grid}(T) = [(1-D)\tilde{n}_{int}^{2}(T) + D\,\tilde{n}_{irr}^{2}(T)]^{1/2} \quad (9)$$

$$\tilde{n}_{\perp}^{grid}(T) = \left[\tilde{n}_{int}(T)\tilde{n}_{irr}(T)\right] \Big/ \left[D\tilde{n}_{int}^{2}(T) + (1-D)\tilde{n}_{irr}^{2}(T)\right]^{1/2}. \quad (10)$$

D is the area coverage (duty cycle) of the irradiated VO_2 and $\tilde{n}_{int}(T)$ and $\tilde{n}_{irr}(T)$ are the temperature-dependent refractive indices of intrinsic and irradiated VO_2 regions. The calculated complex refractive index trajectories are plotted in Figure 2-13(c) onto the n-k space map of calculated reflectance for a 100 nm thin film of the arbitrary refractive index on sapphire at $\lambda = 11$ μm. At the lowest (<25 °C) and the highest (>70 °C) temperatures, the refractive index values for parallel and perpendicular polarized light are the same, whereas for all intermediate temperatures they differ because of the induced anisotropy (Equation 9 and 10). In this temperature region, the complex refractive index change in the mid-infrared is much greater than 1, whereas typical values achievable using, for example, the Kerr effect is no greater than $\sim 10^{-4}$ [96]. The predicted DOLP is 98% and can be improved to almost 100% by choosing an appropriate film thickness.

Although far-field measurements can probe the effective optical properties, the subwavelength patterns of irradiated VO_2 cannot be resolved due to the diffraction limit. To explore the limits of our approach such as the sharpness of the boundary between irradiated and

intrinsic areas, we performed near-field imaging (Figure 2-14). Mid-infrared near-field images at different temperatures clearly show that the effective optical properties originate from the artificial phase coexistence and are not simply caused by a homogeneous distribution of diffused irradiation defects or long-range stress. Near-field images were obtained at temperatures from 30 to 80 °C using a scattering scanning near-field infrared microscope (s-SNIM) at a wavelength of 10.9 μm and with a spatial resolution of ~10 nm (Figure 2-14(a)). The s-SNIM signal is related to the local value of the dielectric function of the sample and provides contrast between the insulating and metallic phase. A scattering scanning near-field infrared microscope (s-SNIM) with a CO_2 laser operating λ = 10.9 μm was used to investigate the local contrast between electronic phases of the patterned sample with a spatial resolution on the order of 10 nm [97]. We simultaneously recorded atomic force microscopy (AFM) topography maps (tapping mode) and the scattering amplitude signal demodulated at the third harmonic of the tapping frequency.

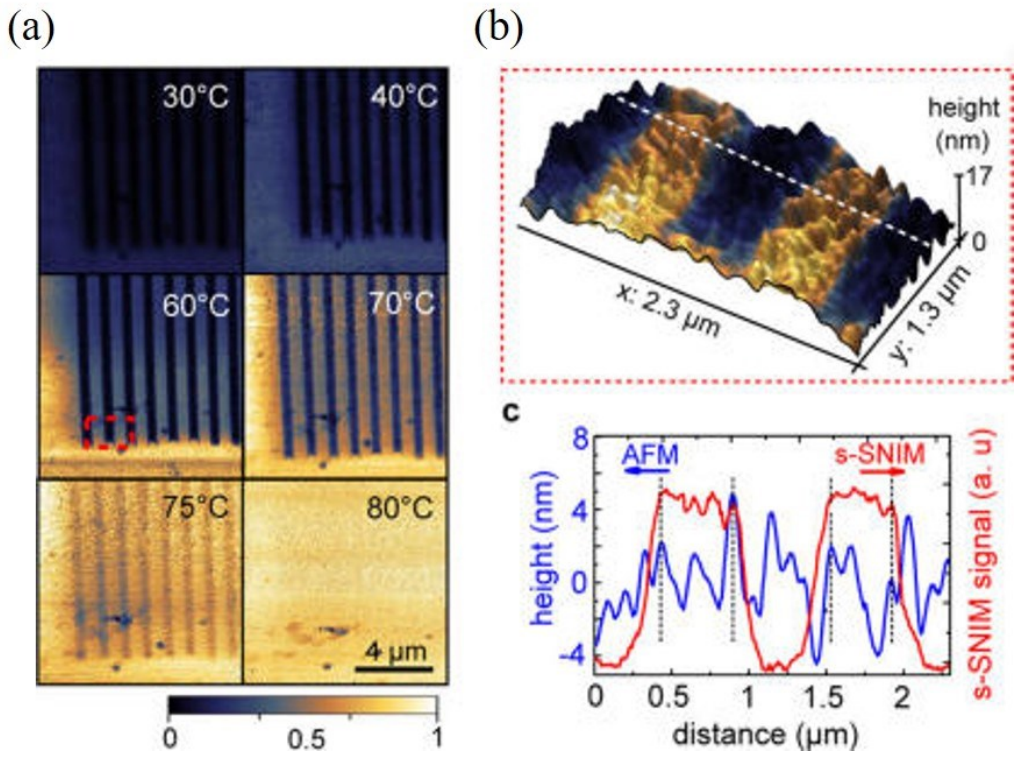

Figure 2-14 *Limits of spatially selective defect engineering probed by infrared nano-imaging. (a) Near-field scattering amplitude of the switchable polarizer of the type shown in Figures 1b and 4 obtained by scattering-type scanning near-field infrared microscopy (s-SNIM) at λ = 10.9 µm for increasing sample temperature. The scattering amplitude is related to the local value of the dielectric function and thus yields a good contrast between the insulating and metallic phases of VO_2. The contrast in the image is highest at intermediate temperatures (~60 °C), at which half of the stripes have transitioned to the metallic state while the others have not. (b) The topography of the sample measured by AFM [zoom-in, corresponding to the red dashed area in (a)] overlaid with the color map of the near-field scattering amplitude that was measured simultaneously at 60 °C. (c) Line scan of the AFM topography (blue) and near-field amplitude (red) taken at the line indicated in (b).*

At low temperatures, both the irradiated and intrinsic VO_2 regions are in their insulating states (e.g., Figure 2-14(a), 30 °C). As a consequence of different defect densities, the intrinsic regions appear slightly darker. With increasing temperature, the irradiated VO_2 undergoes the IMT first and thus those regions appear brighter. For increasing temperature above 60 °C, the contrast

decreases and vanishes completely at >80 °C, which is in agreement with the reflectance measurements in Figure 2-13(b) and (c). By comparing the near-field images with simultaneously acquired topography information, we observe that the spatial boundary between metallic (irradiated) and insulating (intrinsic) VO_2 is not sharp but follows the domain boundaries. A combined AFM and s-SNIM image of a film at 60 °C are shown in Figure 2-14(b) and a representative line scan through the ridges in Figure 2-14(c). Because strain relaxation in thin films tends to terminate at grain boundaries, the best spatial resolution that can be achieved with our approach is reached when the domain size is on the order of the lateral straggle of ions in the film plane (~15 nm, see Appendix A).

2.3 Summary

A VO_2-based two-terminal device was fabricated and characterized by optical microscopy, electrical measurements, and Raman spectroscopy. By current injection, we are able to tune the optical properties of VO_2 locally on the micron scale as observed by spatially resolved FTIR measurements. The results point to interesting directions for further studies in the design of electrically tunable optical devices utilizing phase change materials.

It has previously been shown that it is possible to electrically trigger the phase transition of VO_2 on the nanosecond timescale. We envision our technique being applied to a wide range of high-speed tunable structures, e.g. spatial light modulators and beam steering devices. Furthermore, if spatial control on subwavelength scales can be attained, our technique may enable a new class of dynamically-tunable metamaterials and metasurfaces.

Correlated phase-transition materials featuring insulator-to-metal transitions such as vanadium dioxide have a promising future as tunable components in optics and optoelectronics. The introduction of defect engineering as a robust method to engineer the phase transition on a subwavelength scale greatly expands the utility of these materials, enabling new types of optical meta-devices. We envision defect engineering as a way to bring the critical transition temperature of other phase transition materials, such as rare earth nickelates, closer to room temperature, creating an ecosystem of defect-engineered tunable optical (meta)materials for applications such as optical switching, adaptive optics, and tunable thermal emission.

Chapter 3
Reflective and transmissive metasurface lenses in MWIR

The interest in the applications of mid-infrared (IR) light has recently increased in many areas, such as trace-gas detection, biological and medical sensing, and environmental monitoring [98], [99]. Over the last decade, there has been major progress in the development of new IR sources and detectors. However, a limiting factor in the development of mid-wave and long-wave IR optics is the lack of suitable materials that are transparent, low cost, lightweight, and easy to machine [99]–[101]. Metasurfaces could be used to circumvent the limitations.

3.1 High efficiency and diffraction-limited reflective metasurface lenses

In the reflection mode, designs for focusing in the visible [102] and the near-IR [103], [104] have been reported. As far as we know, there has been no demonstration of a flat lens in the reflection mode in the mid-IR and with high efficiency. Such a device would be ideal for compact catoptric and catadioptric systems such as Cassegrain telescopes, FT-IR microscopy and spectroscopic designs [105], [106]. In particular, astronomers use reflecting telescopes because the lenses in large refractors are bulky, heavy and tend to bend and droop over time. Flat lens technology provides a solution of a lightweight, thin and compact design.

In this section, we report the first high efficiency (80%) mid-IR (λ = 4.6 μm) reflection-based flat lens based on reflectarrays [16]. A reflectarray metasurface is a multi-layered structure consisting of a planar array of antennas separated from a ground metallic plane by a dielectric spacer of subwavelength thickness [107], [108]. Experiments and simulations show that the focusing is near diffraction-limited. It is less sensitive to the change of incidence angle compared to its parabolic mirror counterpart in terms of reflection angle and focal length. The material and

processing requirements of our lens are minimal, requiring only a flat reflective substrate and one photolithography step using conventional high-throughput photolithography steppers, which enables large-scale fabrication. Note that in [109], the mid-IR lens was fabricated using e-beam lithography, but we have successfully fabricated our device using photolithography while tolerating larger fabrication errors than e-beam lithography. The experimental results agree well with the simulation ones considering these fabrication errors.

As a proof of principle, we demonstrated a flat lens with the functionality of a cylindrical lens (one-dimensional focusing). A schematic of the flat lens is shown in Figure 3-1(a): a collimated Gaussian beam arrives at the flat lens at an oblique incidence angle θ and is focused at a length f in the direction normal to the lens surface. The reason for the oblique incidence is purely practical: by using the metasurface itself to spatially separate the incident and reflected beams, we avoid the need for a beam splitter to separate the two beams. This technique simplifies the experimental setup and eliminates the insertion loss introduced by a beam-splitter [110], [104], which improves weak signal detection.

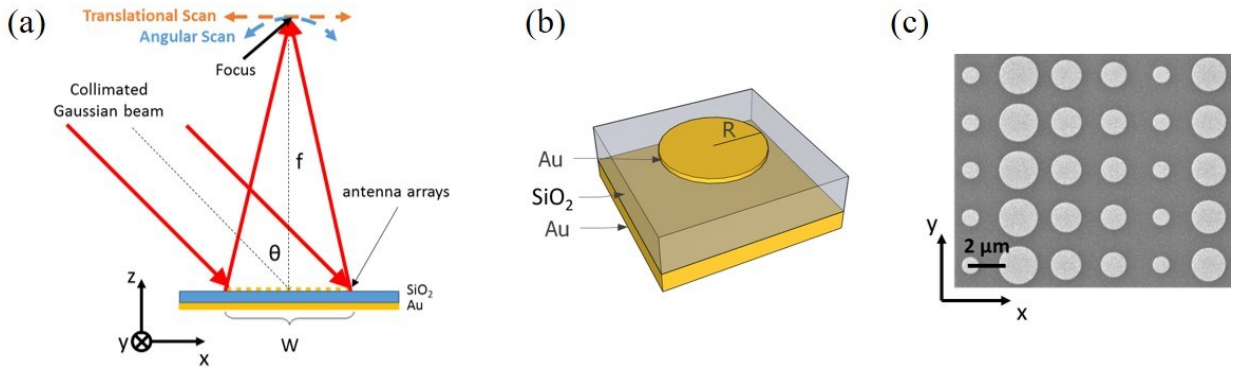

Figure 3-1 *(a) Geometry of the flat lens based on reflectarray antennas. W is the width of the lens. The focus is a narrow line in the y-direction which is characterized by angular and translational scans indicated by the blue and orange dashed lines, respectively. The drawing is not to scale. (b) Schematic of the unit cell of the reflectarray lens: a 50 nm-thick gold disc is separated from a 200 nm-thick gold back reflector layer by a 400 nm-thick SiO_2 spacer. The size of the unit cell is 2.5 μm x 2.5 μm. (c) Scanning electron microscope image of a small section of the fabricated antenna arrays. The center-to-center distance of the discs is the same.*

In order to achieve the desired focusing for $\theta = 0^o$, the phase profile of the wavefront as a function of position x along the metasurface lens must satisfy:

$$\varphi_{focus}(x) = \frac{2\pi}{\lambda_0} \times \left(f - \sqrt{x^2 + f^2} \right). \tag{11}$$

where λ_0 is the wavelength. There is no phase modulation along the y-direction, resulting in a focal line rather than a point. The oblique incident beam arrives with a linear phase gradient of its own, which we can cancel out using the metasurface by applying an additional phase profile:

$$\varphi_{linear}(x, \theta) = -\frac{2\pi}{\lambda_0} \times \left[x \times \sin(\theta) \right]. \tag{12}$$

Thus, we engineer the total phase shift $\varphi$of the lens to be:

$$\varphi(x) = \varphi_{focus}(x) + \varphi_{linear}(x). \tag{13}$$

The total phase function was realized by subwavelength antennas of fixed center-to-center separation. The unit cell of the reflectarray is shown in Figure 3-1(b). We take advantage of the interaction of the antenna with its mirror image in the ground plane: the near-field coupling between the antenna and its image results in a reflected field with a broad phase coverage without polarization conversion [13], [111]. At each center position x, the disc radius was chosen such that its phase response was closest to the calculated value $\varphi(x)$ (Figure 3-2). We used full difference time domain (FDTD module, Lumerical Inc.) simulations with periodic boundary conditions to find a set of phase shift elements with different radii that yielded both a large range of reflection phase and a relatively uniform reflection amplitude, as shown in Figure 3-2. The unit cell configuration is shown in Figure 3-1(b) in the main manuscript. The incident polarization is s-polarized. The phase coverage is from 0 to approximately 1.6π for discs with radii ranging from 0.4 μm to 1 μm. We note that the phase and reflectance are weakly dependent on the incidence angle, so we have tested two lens designs based on the phase response at the incidence angles of 0^o and 45^o and we found that the focusing performance is almost the same.

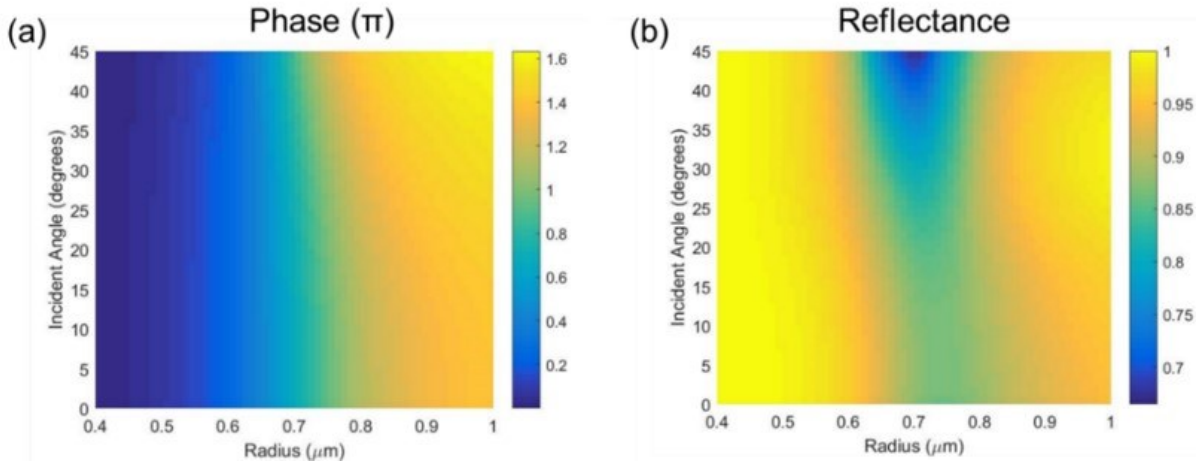

Figure 3-2 *(a) Phase and (b) amplitude response of antennas with varying disc radius for different incidence angles from 0^o to 45^o.*

Using this method, we designed a flat lens for the parameters: θ = 45°, f = 80 mm, and W = 3.08 mm in both x- and y-directions. The numerical aperture (NA) of our lens is 0.02, which can be increased by decreasing the focal length or increasing the size of the lens itself [13], [104]. We fabricated the flat lens on a 6-inch fused silica wafer substrate. The deposition of the gold (Au) back reflector layer and discs was done by electron-beam evaporation. The silicon dioxide (SiO_2) dielectric spacer layer was deposited using plasma-enhanced chemical vapor deposition. The antenna patterns were fabricated using a stepper photolithography tool (GCA AS200 i-line stepper), which allows for large-scale fabrication. Figure 3-1(c) shows a scanning electron microscope image of a small section of the fabricated lens. Note that the 6-inch wafer substrate can accommodate over 160 such lenses with different focusing properties, such as focal lengths and reflection angles.

We have performed both numerical simulations and experimental measurements to characterize the performance of the flat lens. Simulation results are shown in Figure 3-3. Since there is no spatial variation of the antenna array in the y-direction, only one row of disc antennas was simulated and Bloch boundary conditions were applied in the y-direction. To monitor the phase profile created by the lens with an oblique incidence, a monitor was placed $2\lambda_0$ away from the lens surface to record data for the propagating waves only. Figure 3-3(a) shows the phase profile (phase of the E_y component for s-polarized incident light) at the monitor with a resolution of 0.1 μm. The fuzziness is mainly due to the incomplete phase coverage and the variation of the scattering amplitude of antennas (Figure 3-2). The correlation coefficient of the curve fit is $R^2 = 0.99$, indicating a very good agreement between the designed phase profile and the ideal phase profile (black solid line) calculated from the design Equation (11). The transmission data from the monitor, which can be calculated by the amplitude profile, is 84%, i.e. the amount of power transmitted through monitors, normalized to the source power. Figure 3-3(b) is the calculated distribution of the electric field intensity (normalized $|E|^2$) near the focal region in the x-z plane. It was obtained by propagating the field data obtained from the near-field monitor to the far-field (see [112]). Figure 3-3(c) shows the reflected beam intensity (normalized $|E|^2$ in log scale) from the flat lens along a semicircle of radius 80 mm, equal to the focal length of the lens. Only a focused beam at $\theta = 0^o$ is observed. We have verified this experimentally. Figure 3-4 shows the experimental results of an angular scan ranging from -50^o to 10^o with a step size of 1^o. The range of the angular scan is limited by the experimental setup. In addition to the beam focused by the flat lens at $\theta = 0^o$, we also observed a reflected beam at $\theta = -45^o$. This is because the effective laser beam size along the lens surface was bigger than the lens; as a result, the portion of the light not

incident on the lens was directly reflected by the gold backplane. The intensity of the light at -45° is approximately 16.2% of the laser output power.

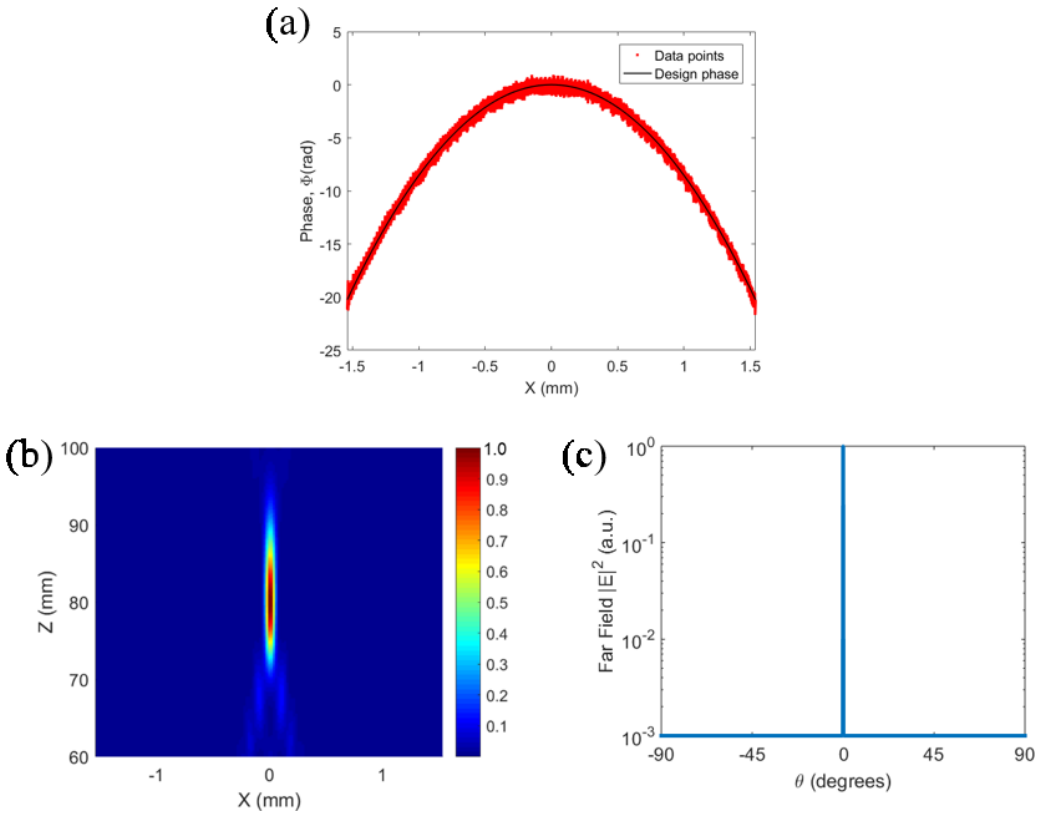

Figure 3-3 *FDTD simulation results of the flat lens. (a) Phase profile created by the lens weighted by the respective reflectance amplitude for an oblique incidence at θ = 45°. (b) Distribution of the intensity (normalized* $|E|^2$*) of the reflected beam in the x-z plane at y = 0. The lens is centered at x = 0 and the size of the lens is from -1.54 mm to 1.54 mm. (c) Far-field angular scan of the reflected beam with the scan radius equals to the focal length).*

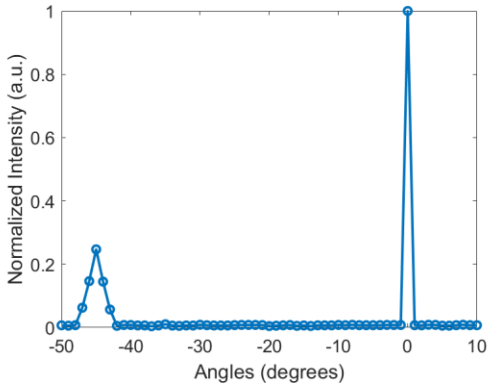

Figure 3-4 *Angular scan of the reflected beam intensity (normalized) from -50º to 10º at y = 0.*

For the experimental characterization of the lens, we used a continuous-wave Fabry-Pérot quantum cascade laser (QCL) (AdTech Optics) emitting at $\lambda = 4.6$ μm. The laser was mounted so that its output beam is s-polarized (electric field along y-direction). We operated the laser near threshold so that the emitted beam is in a single mode. The full beam waist of the laser was 3 mm. The focusing beam created by the reflectarray was collected by a thermoelectrically-cooled mercury-cadmium-telluride detector (VIGO Systems) mounted on motorized rotation and translation stages. To increase the spatial resolution of the scans the light was first sent through a 30 μm pinhole before reaching the detector. The signal-to-noise ratio was increased by modulating the intensity of the QCL with a small sinusoidal current superimposed on the dc current (Wavelength Electronics QCL1500) and demodulating the detected signal with a lock-in amplifier (AMETEK Advanced Measurement Technology).

The reflected focused light from the flat lens was characterized experimentally by angular and translational scans as shown in Figure 3-5(a) and 3-5(b), respectively. The data were taken at the center of the focal line, i.e. $y = 0$. The experimental results are in good agreement with the simulations. The average standard deviation of repeated measurements is 0.2%. Note that the step

sizes used in scanning the reflected beam in Figure 3-5(a) was 0.01° (equivalent to 14 μm in the x-direction) and in Figure 3-5(b) was 10 μm, both smaller than the pinhole diameter (30 μm), so the raw data are a convolution of the true signal and the pinhole response function. Hence, deconvolution was performed to retrieve the original beam profiles. Figure 3-5(a) shows that the measured reflection angle is 0°, which agreed well with the design Equation. The full width at half maximum (FWHM) is less than 0.1°. Figure 3-5(b) shows that the full beam waist at $1/e^2$ of the peak intensity (indicated by the two black arrows) is 164 μm in the experiment and 166.5 μm in the simulation. The diffraction-limited full beam waist ($2w_0$) is 156 μm, calculated by Fourier transformation of an ideal continuous focusing phase profile. Our measured focused beam size is close to the diffraction limit. The difference is likely due to the incomplete phase coverage and the variation of the reflectance amplitude of the antennas (Figure 3-2). Since our lens focuses light into a line, we checked the focused beam profile at other y positions and verified that the focus is near diffraction-limited along the focal line (Figure 3-6). It is worth pointing out that although the results shown are for s-polarized incident light, we have simulated and measured the lens with p-polarized incident light and found that $2w_0 = 167$ μm. Hence, the focusing performance of our lens is near polarization-independent (Figure 3-7).

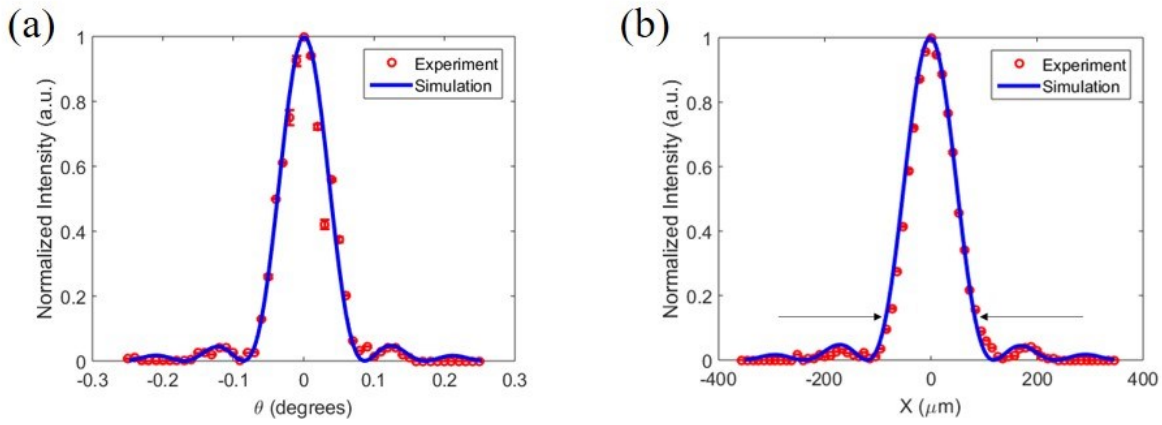

Figure 3-5 *Angular scan (a) and translational scan (b) of the reflected beam intensity (normalized* $|E|^2$*) measured at the center of the focal line. The arrows in (b) indicate the full beam waist measurement in μm.*

Since our lens is a cylindrical lens, the focus is a focal line. The data presented in the main manuscript were taken at y = 0. We expect that the focused beam profile does not change along the y-direction. We experimentally verified it at two other y positions, which are shown in Figure 3-6(a) and 3-6(b). The full beam waist size is 166 μm and 165 μm at y = -0.75 mm and y = 1.4 mm, respectively. Recall that the full beam waist at y = 0 is 164 μm. The difference is small, so we conclude that there is no aberration along the focal line. However, we note that the focused beam intensity varies along the focal line as shown in Figure 3-6(c). This is due to the intensity variation of the Gaussian beam source. The intensity drops to nearly zero beyond the size of the lens, i.e. -1.54 mm to 1.54 mm.

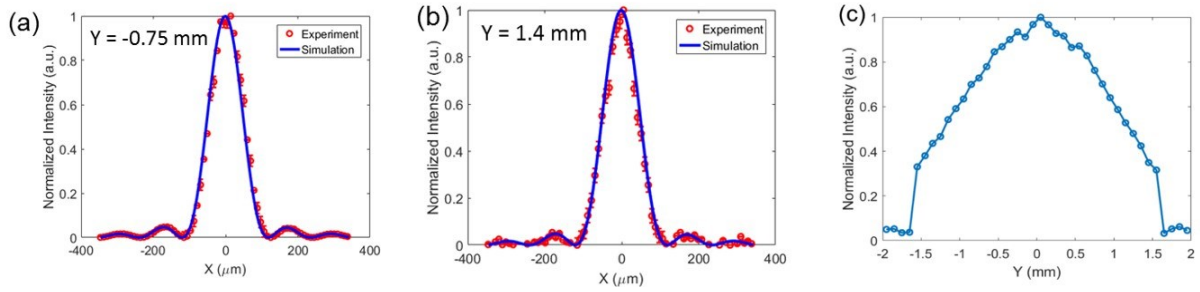

Figure 3-6 *Normalized focused beam profile at (a) y = -0.75 mm and (b) y = 1.4 mm. (c) Normalized focused beam intensity as a function of y measured at x = 0. The step size of the measurement is 100 μm.*

This section summarizes the simulation and measurement results when the incident light is p-polarized (electric field in the plane of incidence) with an incidence angle of $\theta = 45^{o}$. Experimentally, this was realized by mounting the QCL vertically. All measurements were performed on the same lens as in the main manuscript. We found that the focusing performance including the focal length, the beam waist at the focus, and the focusing efficiency is similar to that of the s-polarized light.

Figure 3-7 shows the FDTD simulations of the flat lens with p-polarized illumination. Figure 3-7(a) is the distribution of the electric field intensity (normalized $|E|^2$) around the focal region in the x-z plane. The focal length is 80 mm. Figure 3-7(b) shows the reflected beam intensity (normalized $|E|^2$ in log scale) along with a semicircle of radius of 80 mm. The focusing efficiency is 82% (simulation) and 78% (experiment), which is slightly lower than that of the s-polarized light.

The reflected focused light from the flat lens was characterized experimentally by angular and translational scans as shown in Figure 3-7(c) and 3-7(d), respectively. The experimental results

are in good agreement with the simulations. The scanning parameters are the same as that for the s-polarized light and deconvolution was performed. The reflected light was focused at 0^o and the full beam waist ($2w_0$) at the focus was found to be 167 μm, both in the experiment and in the simulation.

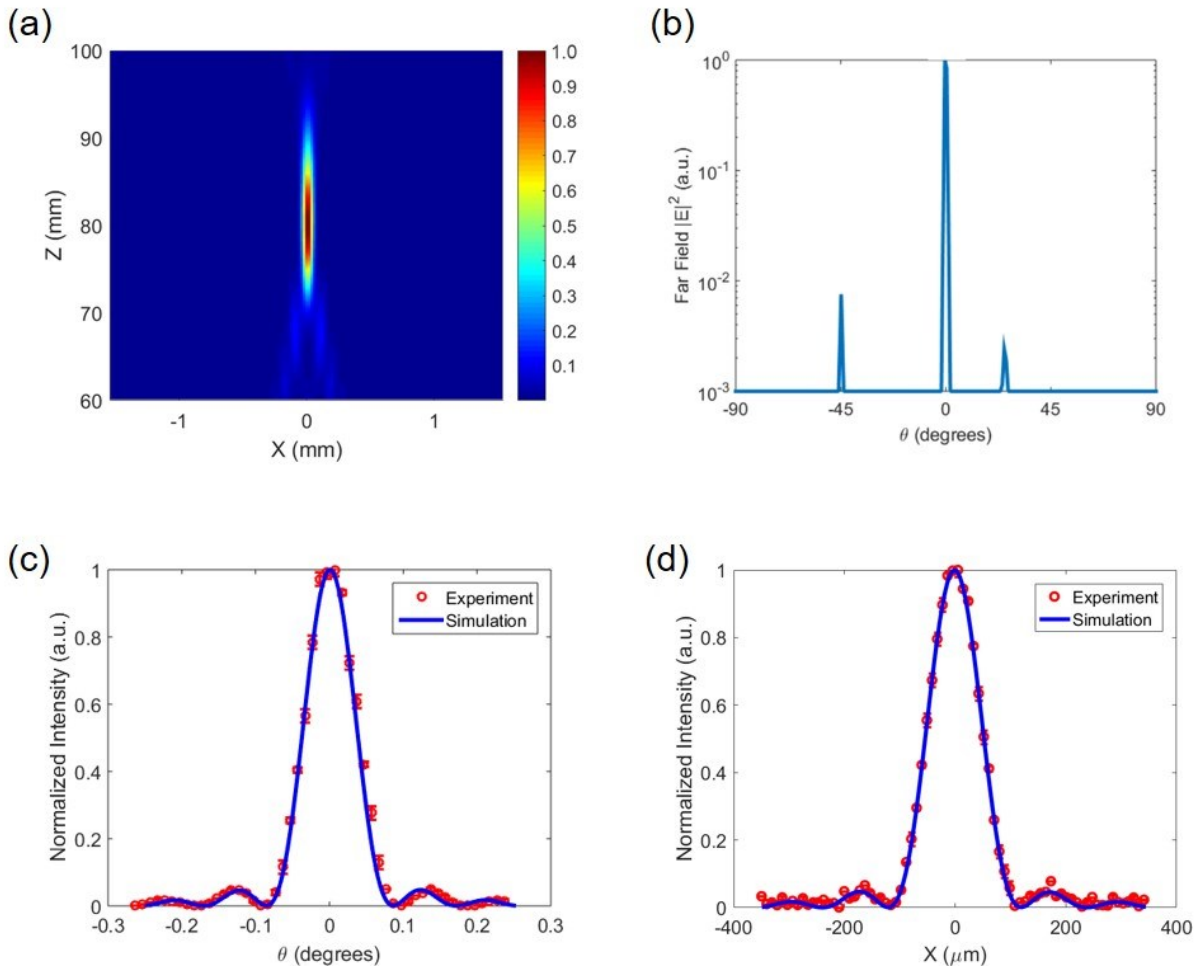

Figure 3-7 *Simulation and experimental results of the flat lens with p-polarized incident light. (a) Distribution of the intensity (normalized $|E|^2$) of the reflected beam in the x-z plane. The antenna arrays are centered at x = 0. (b) Far-field projection of the reflected beam intensity (normalized $|E|^2$ in log scale) showing that the majority of the light was focused at 0^o (normal to the lens surface). (c) Angular scan and (d) Translational scan of the reflected beam intensity (normalized $|E|^2$) at the focus.*

The measured focusing efficiency of the lens was $\eta = 80\%$ which is close to the simulated value of 83%. Most of the loss comes from the metal. Experimentally, the focused beam power was measured by placing a laser power meter (Nova, Ophir Photonics) in the focal region with an iris (~3 mm in diameter) in front to block non-focused light. Note that since the incidence angle was 45°, the effective incident beam size along the lens surface was bigger than the size of the lens, hence, the portion of the incident power on the lens was 82%, which was used to calculate the focusing efficiency. In the simulation, η was calculated by taking the ratio of the optical power in the focal region in Figure 3-3(c) and the incident power. The discrepancy is likely due to fabrication errors. The reasons that enabled us to achieve high efficiency are: (1) reflectarray structures enable us to achieve a large phase coverage of 2π without the need of polarization conversion; (2) material (gold) used in our structure has a low loss in the mid-IR; (3) fabrication and experiment techniques: in [104], authors used a similar structure as ours (metal/dielectric/metal reflectarrays), but the highest efficiency demonstrated was 27% compared to 78% in simulation. It was mentioned in [104] that the discrepancy was due to the fabrication errors.

Table 1 shows the effects of change of incidence angle of the reflectarray lens. The wavelength is fixed at 4.6 μm. The sign of the angle is defined in Figure 3-1(a). If the incidence angle increases (or decreases) from the design angle (45°), the reflected light shifts to more negative (or positive) angles from the normal to the lens surface. The physical origin is that any deviation from the designed incidence angle introduces an extra phase gradient on the surface of the lens, which cannot be compensated by the phase profiles of the antennas. Therefore, scattered waves from each antenna will not arrive at the designed focal line in phase, resulting in a shift in

the position of the focal line. The focal length and the full beam waist, however, remain relatively constant as the incidence angle changes within ±15° from the design angle.

The beam profiles at the center of the focal line for various incidence angles in Table 1 obtained by FDTD simulations are plotted in Figure 3-8(a). The inset shows the difference between each curve taking the one at θ = 45° as the baseline. The difference between the beam profiles is less than 8%. We have cross-checked the results with experiment for θ = 35° and 55°, which are shown in Figure 3-8(b). The simulations and experiments agree well with each other.

Table 1 *Effects of incidence angle on reflectarray lens (NA = 0.02) at λ_0 = 4.6 μm.*

Incidence angle (°)	Reflection angle (°)	Focal length (mm)	Full beam waist (μm)
30	12	76	163
35	7.7	78	165
40	3.7	80	167
45	0	80	166.5
50	-3.4	79	165.5
55	-6.5	79	165.5
60	-9.2	78	164.5

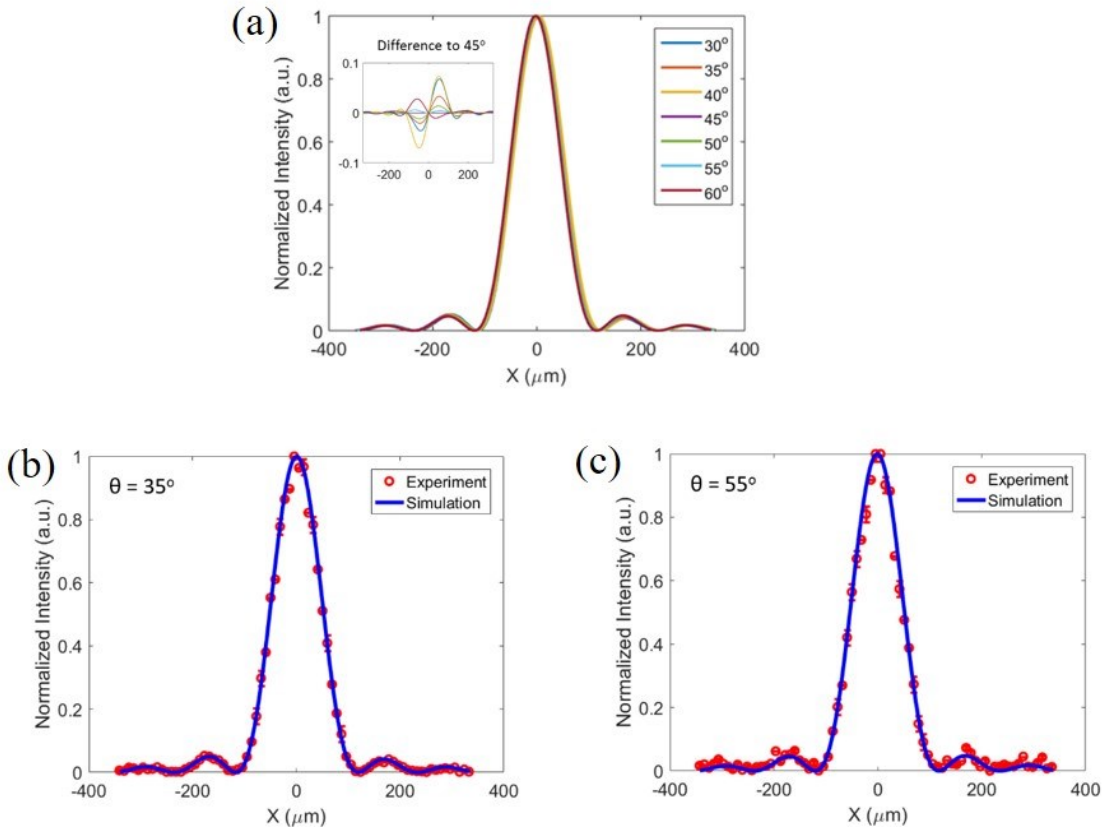

Figure 3-8 *(a) The focused beam profile for various incidence angles obtained by FDTD simulations. The inset shows the difference between the beam profiles and the one corresponding to an incidence angle of θ = 45°. Experimentally measured focused beam profiles for (b) θ = 35° and (c) θ = 55° compared with the simulation results.*

Parabolic mirrors are widely used for focusing in the IR spectral range but are known to be very sensitive to the change of incidence angle [113]. Hence, we studied the effects of the incidence angle of an off-axis parabolic mirror of the same NA using ray tracing techniques [113]. The result is shown in Table 2. The change in the reflection angle always equals the change in the incidence angle, which is expected for a mirror. But both the change in the reflection angle and the change in the focal length are larger than those of the reflectarrays as shown in Table 1. It is more clearly

seen in the ray tracing plots of the reflectarray lens (red lines) and the parabolic mirror (blue lines) in Figure 3-9(a)-(c) where the incidence angle is 35°, 45°, and 55°, respectively. When $\theta = 45^{o}$ (design angle), both the red and blue lines focus at $x = 0$ and $z = f = 80$ mm. When the incidence angle changes, the focus of the blue lines deviates more from the designed focus than that of the red lines. Hence, our reflectarray lens is not only thinner and lighter but can also be designed to be less sensitive to the change in the incidence angle than a parabolic mirror in terms of reflection angle and focal length.

Table 2 *Effects of incidence angle on parabolic mirror (NA = 0.02).*

Incidence angle (°)	Reflection angle (°)	Focal length (mm)
30	15	86
35	10	85
40	5	83
45	0	80
50	-5	77
55	-10	73
60	-15	69

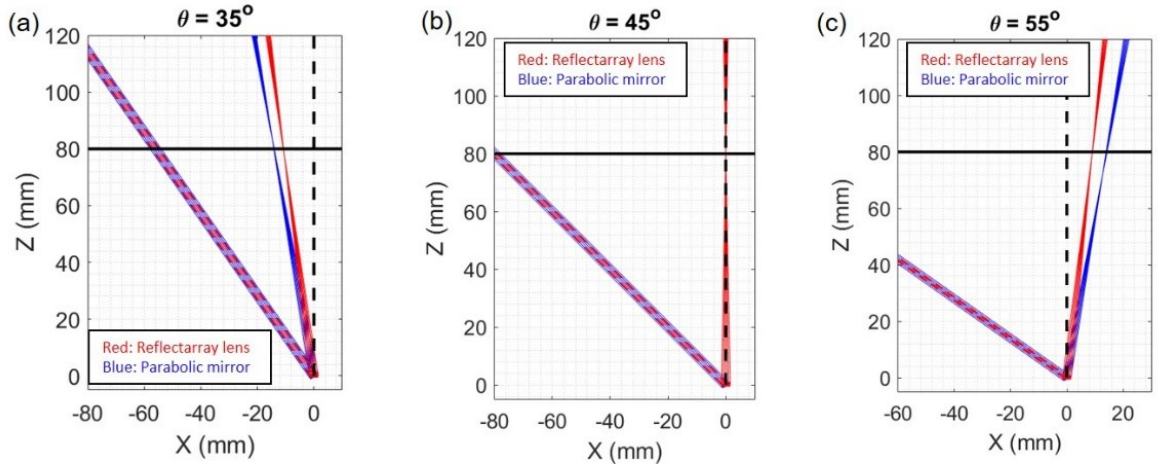

Figure 3-9 *Ray tracing plots of reflectarray lens and parabolic mirror of NA = 0.02 for incidence angles (a) θ = 35°, (b) θ = 45°, and (c) θ = 55°. The vertical black dashed line is at x = 0 and the horizontal black solid line is at z = 80 mm (focal length).*

Studies of the effects of the incidence wavelength using FDTD simulations are summarized in Table 3. Depending on whether the incident wavelength is shorter or longer than λ_0 = 4.6 μm; the reflection angle is negative or positive, respectively. The focal length decreases but the full beam waist remains relatively constant as the incident wavelength increases.

Table 3 *Effects of incidence wavelength on reflectarray lens for incidence angle θ = 45°.*

λ (μm)	Reflection angle (°)	Focal length (mm)	Full beam waist (μm)
4	-5.3	91	165
4.6	0	80	166.5
5	3.6	73	167

3.2 Solid-immersion flat lenses for mid-infrared detectors

The high operating temperature of infrared imagers can be achieved by integrating detectors with optical concentrators that increase optical collection area while keeping detectors volume constant. The most common way to realize optical concentrators is by integrating spherical microlens with detectors but this technology is not well developed in mid- and long-infrared. The goal of this work is to enable infusion of novel optical components based on nanophotonics and metasurfaces into the development of IR detectors. Utilization of these recently invented metasurfaces has potential to significantly advance the state-of-the-art of IR devices. In particular, they can replace the microlens by offering better collection efficiency (up to 90%) and by eliminating spherical aberrations. Moreover, the flat lens will not only reduce the weight and volume of the optics but also simplify the optics cooling, which is required in the IR sensing applications at low light levels, and minimize the cooling power. The proposed work will result in a new class of IR detectors integrated with a metasurfaces-based, focusing lens in MWIR for sensing applications. The integration of flat and ultrathin lenses based on metasurfaces with the barrier infrared detector (BIRD) [113] has the potential to achieve an order of magnitude increase in signal-to-noise ratio (SNR) of these integrated devices.

To be integrated with photodetectors in the future, we designed a new type of transmissive lenses that focus light in the substrate (as compared to in the air in normal cases). The lenses focus in two dimensions with high focusing efficiency and work for all incident polarization. Another feature is that the meta-lens optical components and the substrate were made of the same material GaSb. This makes the fabrication process simpler by only requiring a single step of lithography and etching. Our demonstration will result in a new class of infrared detectors integrated with a

metasurfaces-based, focusing lens with potentially improved signal-to-noise ratio for sensing applications.

We worked on two lens designs. For the monochromatic meta-lens, the incident light (λ = 4 μm) is normal to the metasurface lens (D = 30 μm), which consists of GaSb (n = 3.73) posts with different radii. The circular shape of the post structures ensures that the lens design is independent of the incident light polarization. The metasurface focuses the light in the GaSb substrate. The unit cell of the metasurface is shown in the inset of Figure 3-10(a). The height of the posts is h = 2 μm. By varying the diameter of the posts (d = 200 - 1240 nm), a phase coverage of close to 2π and a high, uniform transmission amplitude response are achieved (see Figure 3-10(a)). These data were used as a lookup table to digitize the phase profile. The designed focal length is F = 150 μm, which gives the metasurface lens a NA = n*sin(atan(D/2F)) = 0.37. The phase profile was realized by subwavelength antennas with fixed edge-to-edge separation [19], by which the placement of antennas is made denser than that with the conventional fixed center-to-center separation. In our design, we chose the edge-to-edge spacing to be 400 nm, which was determined to avoid interaction between neighboring antennas. Note that only posts with a diameter range from 440 to 1170 nm are necessary to achieve the phase coverage required. Figure 3-10(b) and (c) are the normalized field intensity in the x-z plane and x-y plane, respectively. The focal length is determined with the highest intensity point at z = 150 μm. The focal spot is symmetric in the x- and y-direction. The full beam waist is determined to be 7.4 μm at the focus (the x span when the intensity drops to $1/e^2$ of the peak value). It is near diffraction-limited, which is 6.8 μm. The focusing efficiency is calculated to be 75.3%, the total intensity within a 10 μm diameter

(corresponds to one single pixel size of the IR photodetector) as a ratio of the total incident intensity. All simulations were performed using the FDTD module from Lumerical, Inc.

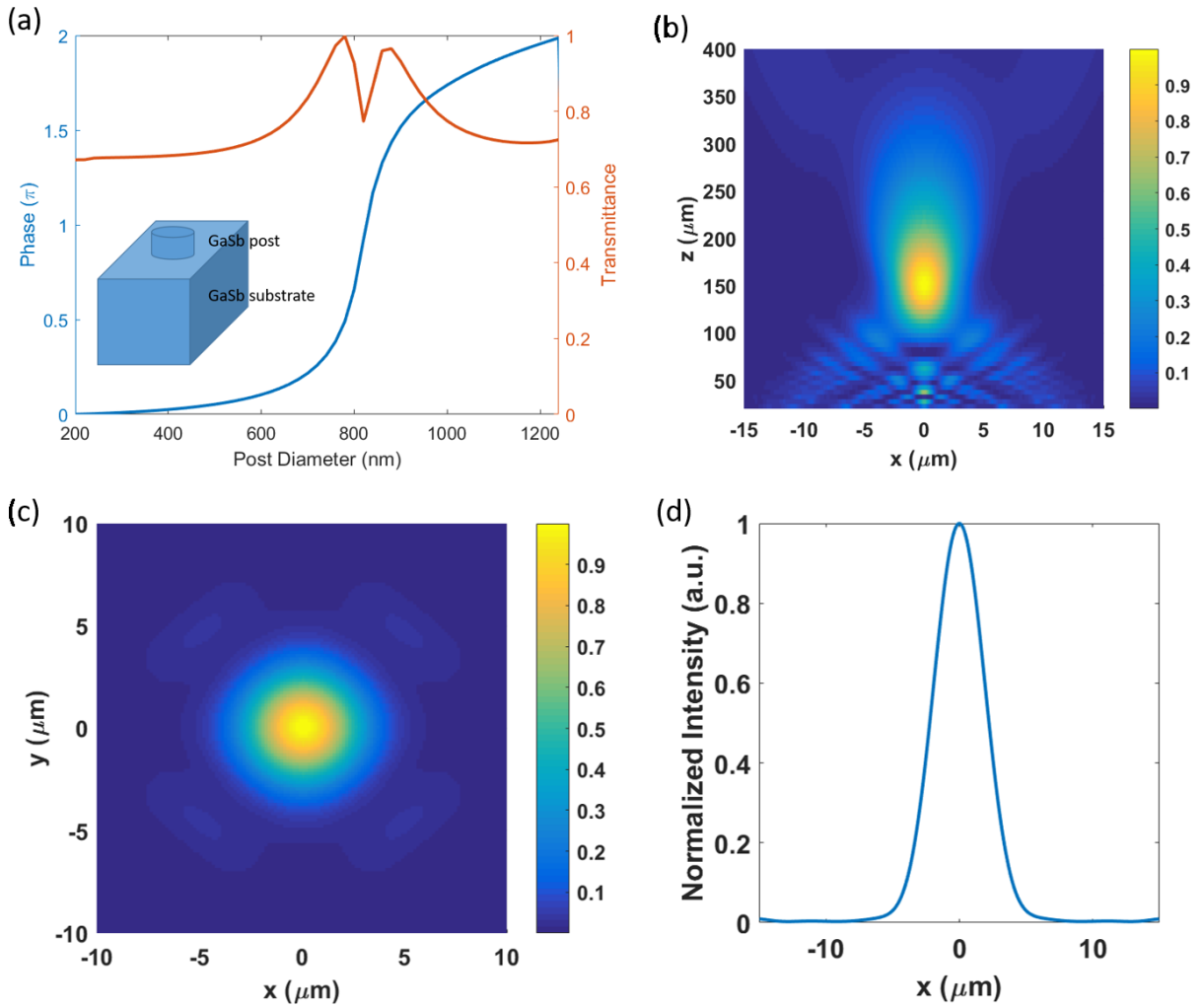

Figure 3-10 *FDTD simulation results. (a) Phase and amplitude response of GaSb posts with different radii. The inset is the design of the unit cell. (b) Normalized intensity plot in the x- and z-direction at y = 0. (c) Normalized intensity plot in the x- and y-direction at z = F = 150 μm. (d) Normalized line scan at the focus, i.e. at y = 0 and z = 150 μm.*

For the broadband meta-lens, the incident wavelength range is from 3 to 5 μm. The post height is 2 μm throughout and the post diameter range is 750 – 980 nm which is photolithography

compatible. The post height-to-diameter aspect ratio is smaller than 2.7, which makes the etch process much easier. Figure 3-11(a) is the beam size as a function of incident wavelength at the camera plane. The new focal length is 158 μm. The two black dashed lines indicate the pixel size of the camera, i.e. 10 μm. The beam size is confined within the 10 μm window for the entire wavelength range. Figure 3-11(b) plots the focused beam profile of selected wavelengths. We can see that the beam size does not vary much. Figure 3-11(c) shows the focal length as a function of wavelength. For achromatic focusing, a flat curve is desired. The black dashed line indicates the designed focal length. The current design is not perfect as there is variation, but the curve is flat for $\lambda = 3.2 – 4.1$ μm, i.e. the achromatic bandwidth is $\Delta\lambda = 0.9$ μm. The error bar for the focal length is 2 μm, which is the resolution in the z-axis in the simulation. The percentage change in the focal length is plotted in Figure 3-11(d). The change is smaller than 10% for wavelengths $\lambda = 3.1 – 4.5$ μm.

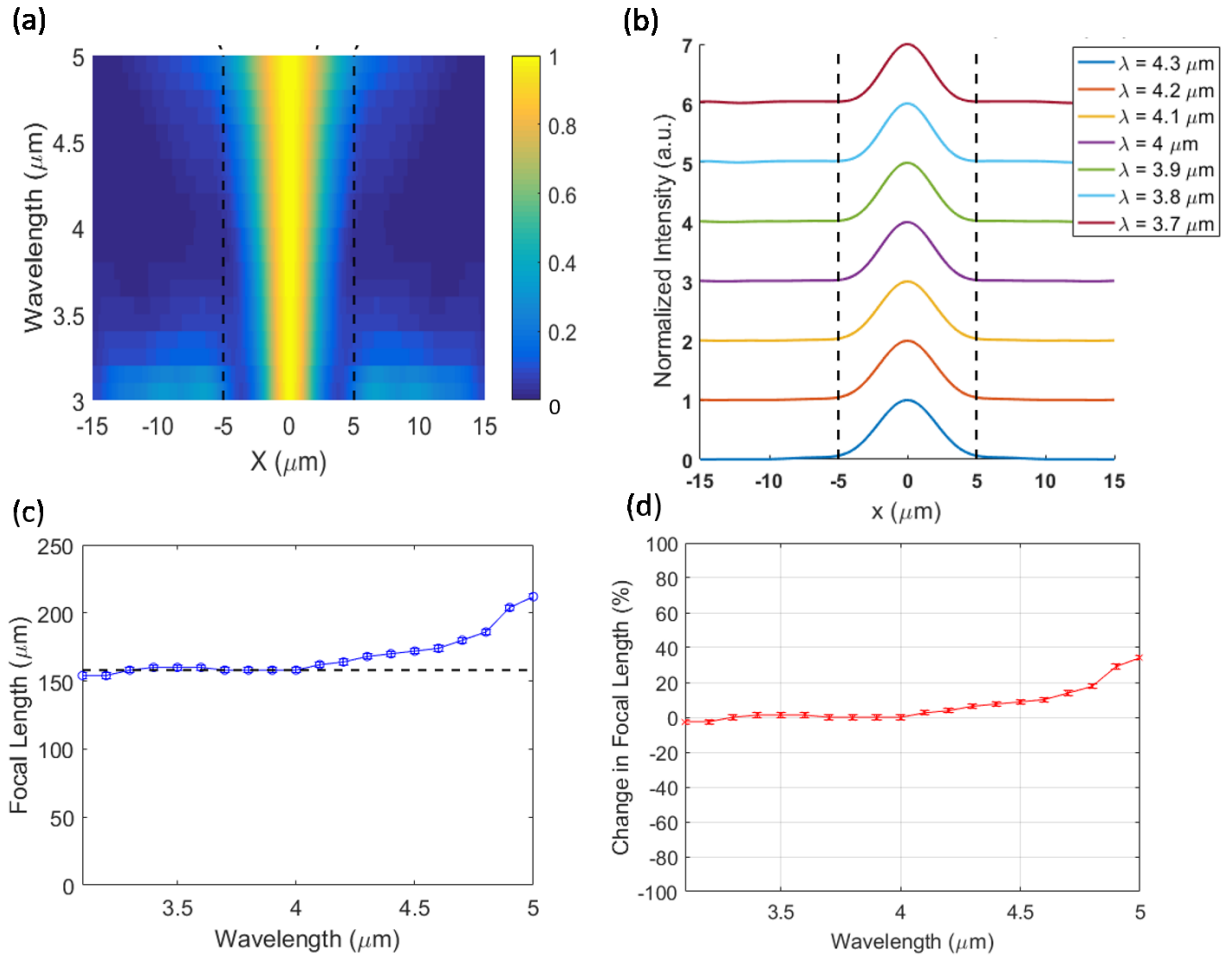

Figure 3-11 *FDTD simulations of the broadband meta-lens. (a) Beam profile as a function of incident wavelength at the camera plane. The two black dashed lines indicate the pixel size of the detector, i.e. 10 μm. (b) Horizontal line cuts of (a) at selected wavelengths. Curves are shifted in the y-axis for visual clarity. (c) Focal length as a function of wavelength. The black dashed line indicates the designed focal length, 158 μm. (d) Percentage change in focal length as a function of wavelength.*

We fabricated an array of metasurface lenses on a GaSb substrate (thickness = 500 μm). The substrates were first cleaned with solvents, oxygen plasma ash, and buffered oxide etch. Then a hard nitride mask SiN_x was deposited on the wafer to encapsulate and protect the surface of the wafers during next fabrication steps. The meta-lenses were defined by e-beam lithography using a

ZEP520A resist with a film thickness of around 500 nm. After the ZEP520A development, the hard mask was etched with CF_4/O_2 using an Inductively-Coupled Plasma (ICP) fluorine system (Plasma-Therm ICP etching system). Prior to the etching, samples were mounted on substrate carriers with a thermal conductive-cooled adhesive medium. After the fabrication, the meta-lenses were measured with a scanning electron microscope, Alpha-Step optical surface profilers to verify the lens parameters. The result is shown in Figure 3-12.

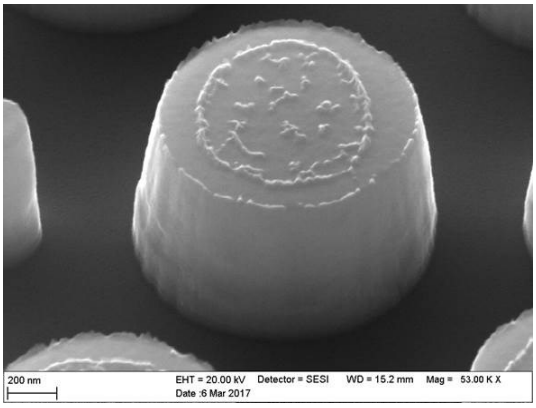

Figure 3-12 *Fabricated lens. The SEM image shows one GaSb post.*

The measurement setup is shown in Figure 3-13. The blackbody at 1000 ^oC was used as the infrared source. In order to investigate the broadband response of the lenses, we performed measurements with five bandpass filters: BP-3050-200 nm (2950 - 3150 nm), BP-3390-345 nm (3220 - 3565 nm), BP-3900-200 nm (3800 - 4000 nm), BP-4220-200 nm (4120 - 4320 nm), and BP-4665-240 nm (4545 - 4785 nm). The meta-lenses were placed after the bandpass filters with the posts facing the source. The focal spot was observed using a combination of optics including a microscope objective of 36X (to magnify the focused beam) and an infrared camera (MW FPA

FLIR SBF184 19.5 μm 1024×1024 pixels). During the measurement, we moved the microscope objective along the optical axis.

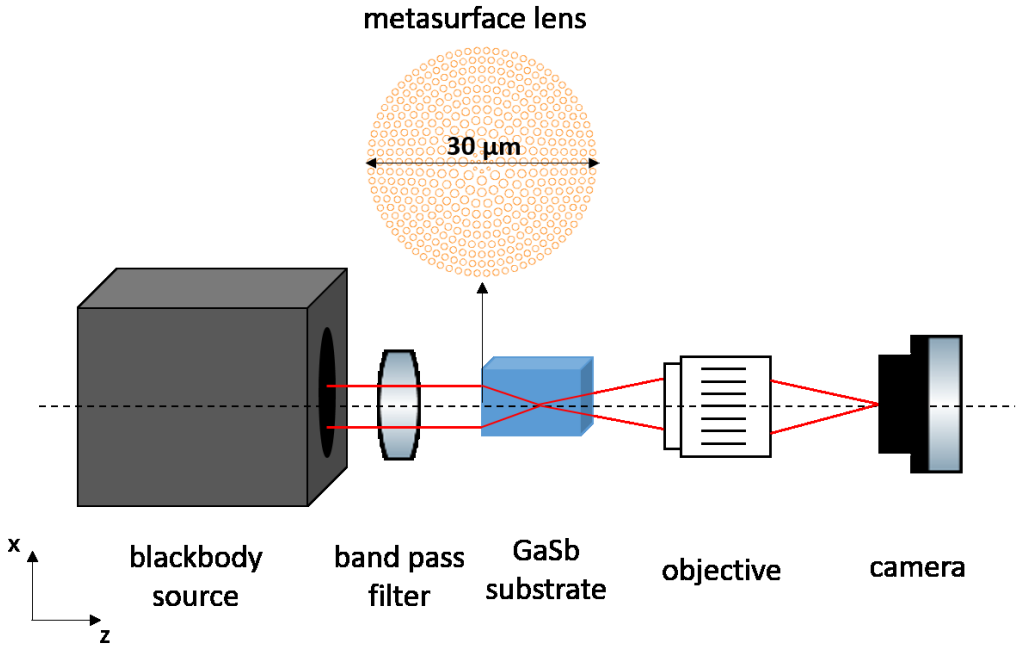

Figure 3-13 *Experimental setup. The metasurface lens array is facing the front of the blackbody. The inset shows a zoomed-in view of one lens. This is a drawing of the actual design of the lens.*

Figure 3-14 are measurement results of the monochromatic lens design. Z = 0 μm was set when the camera is focused on the edge of the etched corner. The microscope objective was then moved away from the lens in 1 μm step, i. e. scanning the focal spot along the z-direction. The normalized electric field intensity in the x-z plane is shown in Figure 3-14(a). The incident wavelength values are taken as the center wavelength of the bandpass filters. There is one subtle point worth pointing out is that in this measurement technique, the measured z values need to be multiplied by the refractive index of GaSb to reflect the real values, which is shown in the figure.

The explanation is given in the supplementary information. The beam profiles at the focus are shown in Figure 3-14(b), which are the line cuts at the maximum intensity values. The dots are measured data and the lines are Gaussian fits. The x values of the peaks shift slightly. The closest to the designed incident wavelength is the green curve. The measured full beam waist at $1/e^2$ of the peak intensity is 13.9 μm. The difference with the simulated value is possibly due to the slope of the fabricated posts being not exactly 90° as designed. The effect of the fabrication errors are studied by simulations and results are given in the supplementary information. The focal length as a function of the incident wavelength is shown in Figure 3-14(c). The focal length decreases as the incident wavelength increases as expected for a single wavelength lens design. The focal length is 149.2 μm for the green curve which is close to the simulated value. The camera images at the focus are given in the supplementary information.

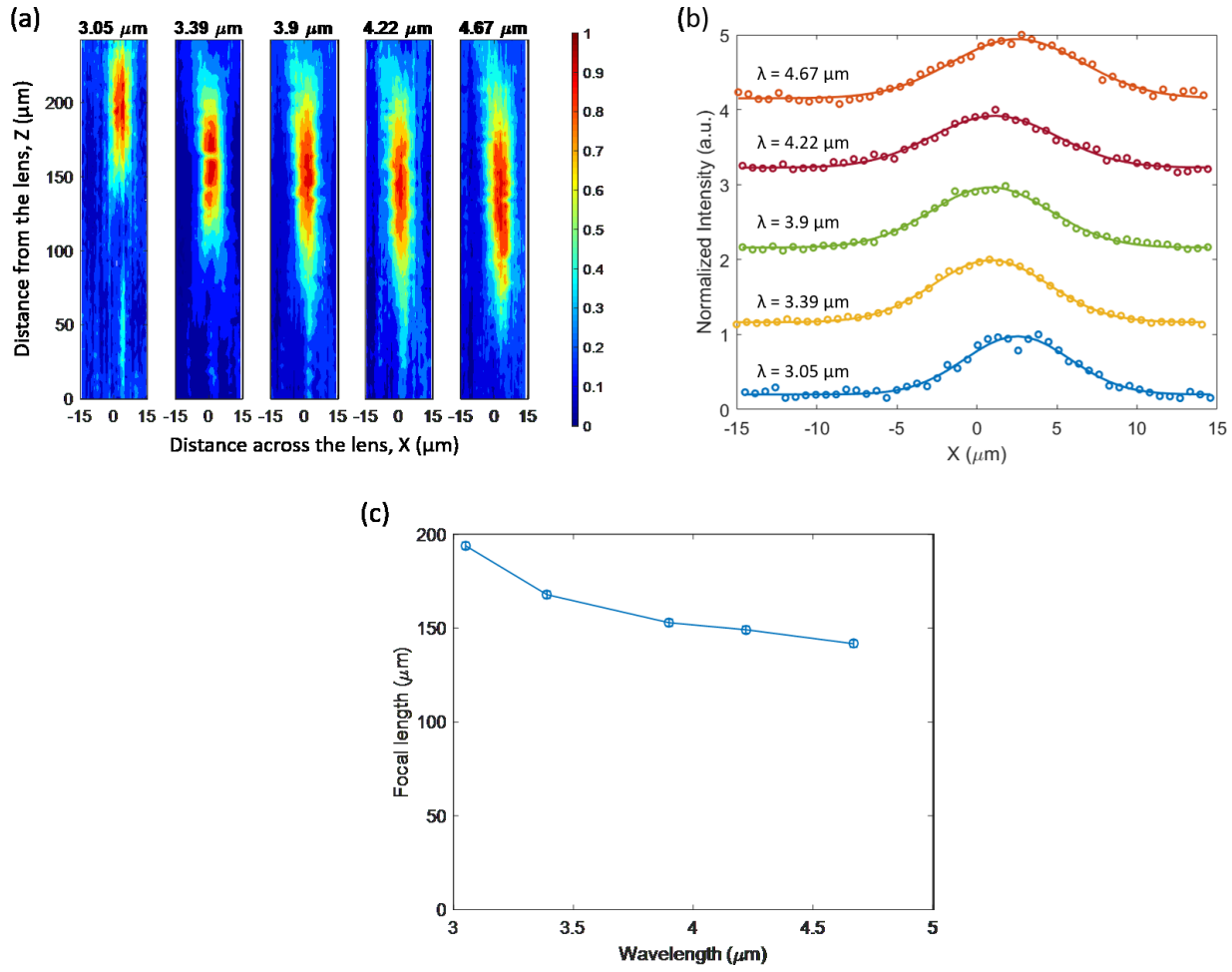

Figure 3-14 *Measurement results for the monochromatic lens design. (a) Normalized electric field intensity in the x-z plane for different incident wavelengths. (b) Focused beam profiles at peak intensities. (c) Focal length change as a function of incident wavelength.*

Figure 3-15 is the measurement results for the broadband design. Improvements from the monochromatic lens design include: (1) The x positions at the center of the peaks shift less. (2) The focal length is constant for the first three bandpass filters, i.e. from 2.95 - 4 μm. As the wavelength increases further, the focal length decreases. The measured results are consistent with the simulated ones in Figure 3-11(c).

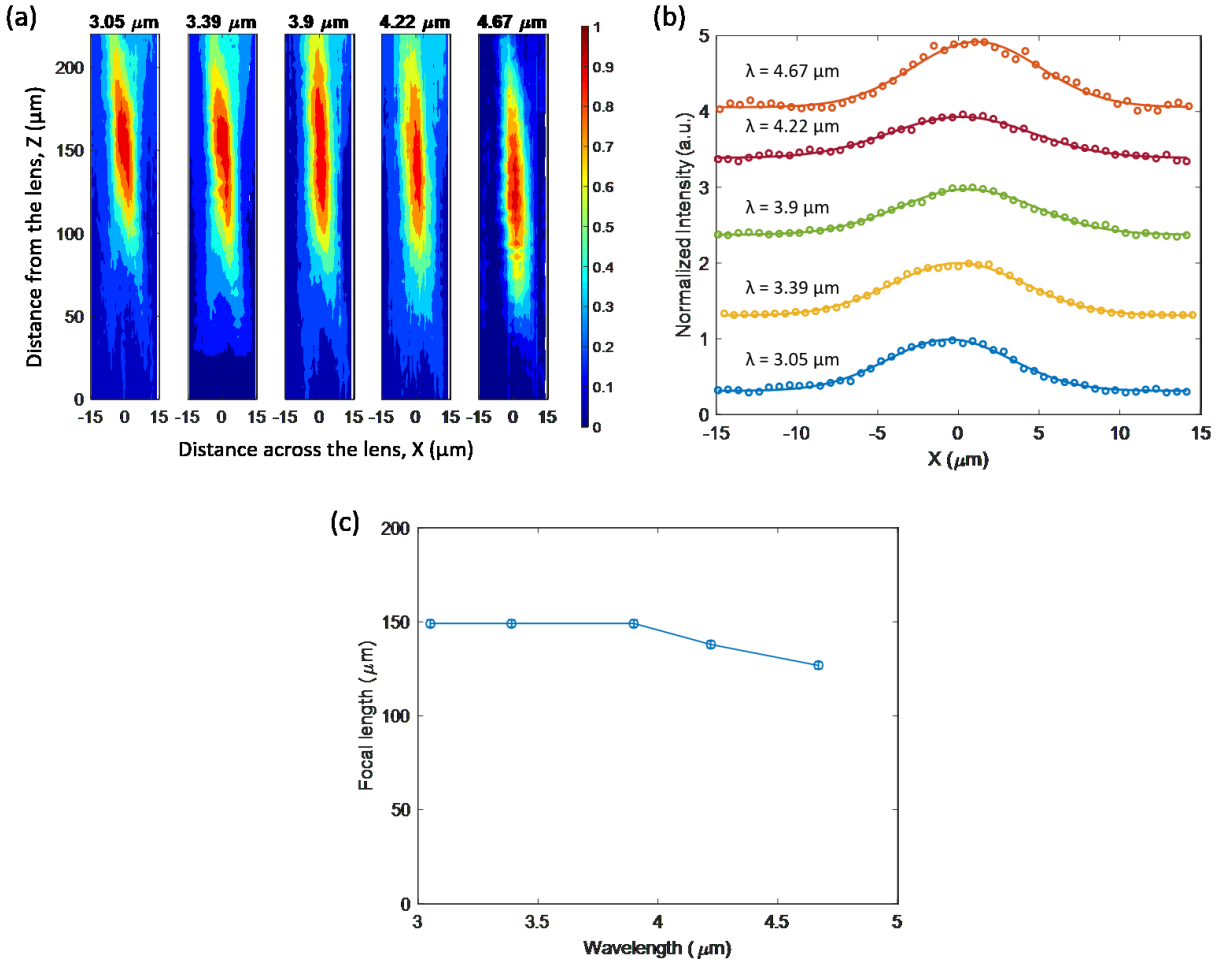

Figure 3-15 *Measurement results for the broadband lens design. (a) Normalized electric field intensity in the x-z plane for different incident wavelengths. (b) Focused beam profiles at peak intensities. (c) Focal length change as a function of incident wavelength.*

The measured intensity enhancement values are given in Table 4. The values were calculated as the ratio between the intensity at the focus and the incident intensity. Both values were measured with the camera placed after the bandpass filters. The two designs perform similarly with around three times intensity enhancement. The highest enhancement is in the wavelength range 3220 - 3565 nm.

Table 4 *Measured intensity enhancement of the two designs for different incident wavelengths.*

Bandpass filters	Monochromatic design	Broadband design
BP-3050-200 nm (2950 - 3150 nm)	2.7x	2.7x
BP-3390-345 nm (3220 - 3565 nm)	3.3x	3.2x
BP-3900-200 nm (3800 - 4000 nm)	2.8x	2.8x
BP-4220-200 nm (4120 - 4320 nm)	2.4x	2.8x

3.3 Summary

In the first section, we designed a mid-IR flat lens that consists of a reflectarray of metallic antennas with subwavelength spacing. The focusing performance of the lens and effects of incidence angle and wavelength were studied by experiments and simulations. We have achieved 80% focusing efficiency and near diffraction-limited focusing. One possible way to further improve the efficiency is to consider the optical impedance of the planar device to match with that of free space. Some of the examples are given in [114], [115]. We found that the effects of incidence angle on the reflection angle and focal length were small for a deviation of the incidence angle within ±15^{o}, which compare favorably to an off-axis parabolic mirror with the same NA. Our approach based on illuminating the flat lens at an oblique angle has the advantage of a simplified experimental setup compared to other reflection-based measurements with normal incidence. Our lens has a number of attractive features, including high focusing efficiency, the flexibility of design, polarization-independence, a straightforward fabrication based on single-step photolithography, and reproducibility on a large scale. Although our flat lens is not aberration-free, there are strategies to reduce coma [102], [116] and chromatic aberrations [14], [117]–[121] of flat lenses. We envision that our flat lenses will complement or replace various conventional bulky

optical components in systems for IR imaging, ranging, and detection, as well as for beam shaping of IR lasers and beacons.

In the second section, we successfully demonstrated a new type of transmissive meta-lenses that operate as solid-immersion lenses, i.e. incident light is focused in the substrate. These lenses were fabricated directly on GaSb substrates using an unbroken CMOS-only process flow. Two lens designs were studied and both showed intensity enhancement of around three times at the focus compared to the incident intensity. The focal length of the broadband meta-lens does not change for 2.95 - 4 μm. Current state-of-the-art infrared devices use microlens arrays to improve external quantum efficiency and signal-to-noise ratio but are limited in terms of choice of materials and precise control over the lens shape. Our demonstration is the first step in the realization of infrared detectors monolithically integrated with flat lenses. The integrated device with small (< 30 μm) active elements will reduce the detector volume (and therefore the dark current). The size reduction combined with increasing optical collection efficiency by the meta-lens is predicted to enhance the signal-to-noise ratio by 5-10 times.

Chapter 4
Reconfigurable metasurface lenses integrated with MEMS in MWIR

In this chapter, we introduce the concept of dynamically controlling metasurfaces by integrating them onto MEMS [122]. MEMS unique advantages are high speed and excellent optical quality, wavelength and polarization independence, and low optical loss [123]. We present a prototype consisting of a MEMS-controlled reflective metasurface lens that focuses in the mid-IR spectrum. The preferred MEMS device is an electrostatically controlled 2D scanner micro-mirror because it is a key element used in many applications such as LIDAR laser scanners [124], optical communications [125], [126] and bio-imaging [127]–[130]. Technologies like these will greatly benefit from a dynamically controlled metasurface-based lens because it will enable the removal of bulky optical components in the system while allowing unique functions such as the predetermined shaping of light beams. When electrostatically actuated, the MEMS platform controls the angle of the lens along two orthogonal axes enabling scanning of the flat lens focal spot by about ±9 degrees in each direction. When the incident light is off the designed angle, the device can compensate for the off-axis degree and thus correct for any off-axis aberrations such as coma.

4.1 Lens design and fabrication

We design a plasmonic lens producing a line focus, like a cylindrical lens, when illuminated with $\lambda = 4.6$ μm light. As the design unit cells, we choose subwavelength sized 50 nm thick gold resonators in the shape of a disc (Figure 4-1(a)), so that the device is polarization

independent. The resonators sit on a 400 nm thick silicon dioxide layer deposited on a 200 nm thick continuous gold film. This structure has been used to improve the focusing efficiency in reflection [16], [107]. By changing the radius of the disc, the phase of the reflected light changes (Figure 4-1(b)). To construct a planar lens, we spatially distribute the discs with varying radii to realize the hyperbolic phase profile. Figure 4-1(c) and (d) show a schematic of the reflective metasurface lens when a collimated Gaussian beam is incident perpendicularly (c) and at an angle, θ (d) on the lens and is focused at a distance *f* along the normal axis to the lens surface. This configuration proves the flexibility of our design technique: by using the metasurface itself to spatially separate the incident and reflected beams, we avoid the need for a beam splitter, resulting already in a reduction in the number of bulk optical components that are conventionally used in optical systems.

The equation of the phase profile used to design the metasurface lens is given by Equation (13). The lens functions as a cylindrical lens, i.e. one-dimensional focusing, so the phase profile is only a function of x [16]. One improvement from previous literature [8] is that the elements are placed in such a way that their edge-to-edge distance is constant so that the overall packing density is increased which improves the sampling of the ideal phase profile. The metasurface lens demonstrated here is designed on a square layout with each side measuring W = 0.8 mm to focus light incident at an angle of θ = 45° normal to the lens surface at a distance *f* = 5 mm away.

The metasurface lens is fabricated using standard photolithography techniques on a silicon-on-insulator (SOI) wafer with a 2 μm thick top device layer, a 200 nm buried-oxide layer, and a 600 μm thick handle layer. SEM images of the reflective lens are shown in Figure 4-1(e) and (f).

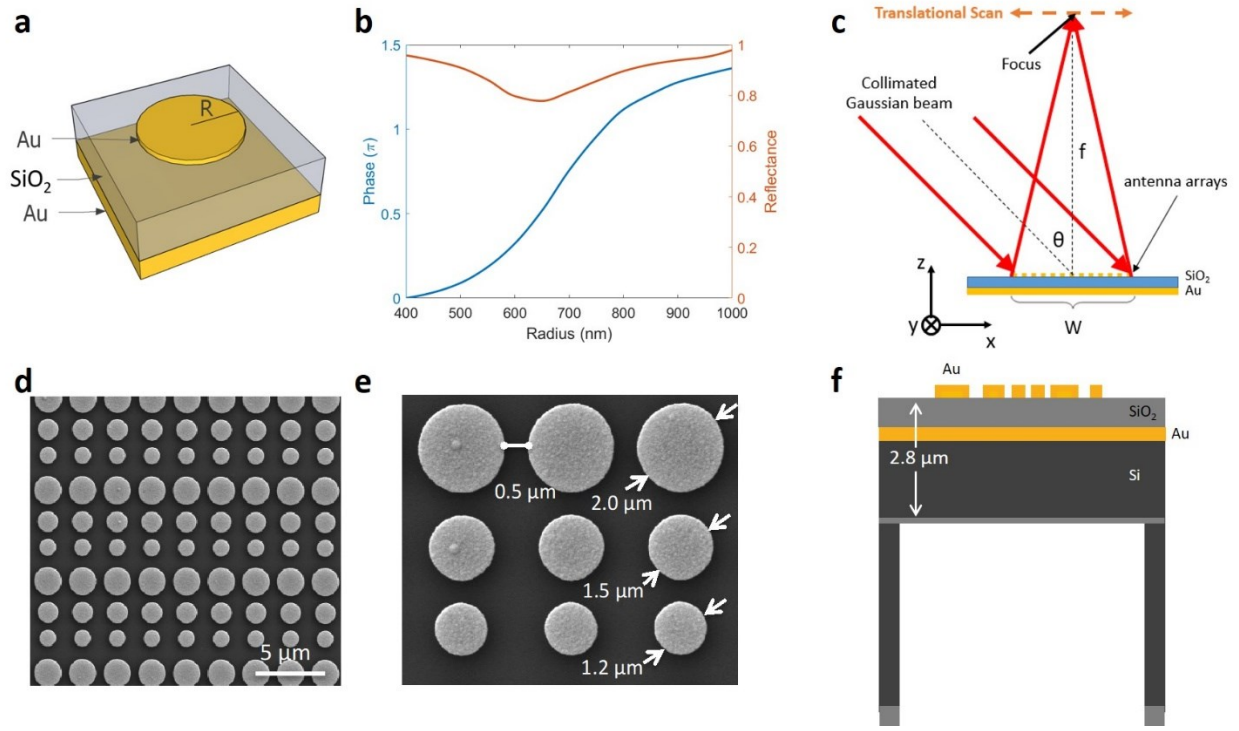

Figure 4-1 *Design and fabrication of the metasurface lens: (a) A unit cell consisting of a 50 nm thick gold disc on 400 nm thick silicon dioxide substrate with a 200 nm thick gold backplane. (b) Simulated values of reflectance and phase for varying sizes of gold discs. (c) Schematic representation of focusing characteristics of the reflective metasurface lens for tilted illumination. (d,e) Scanning electron microscope images of the fabricated lens. (f) Schematic cross-section of the different constituting layers of the membrane-supported flat lens.*

Here we describe the fabrication steps following the Figure numbers of Figure 4-2: (a) On the topside of the SOI wafer, a 100 nm thick protective layer of silicon nitride (Si_3N_4) is deposited by the plasma-enhanced chemical vapor deposition process. On the backside, a 110 nm thick layer of silicon dioxide (SiO_2) is deposited using the same process; this layer would serve as the oxide mask for etching the handle layer at a later stage of the fabrication. (b) A positive photoresist (SPR 700) is coated on the backside and exposed using a stepper tool (Autostep 200 i-line) to print circular windows, which would be perfectly aligned with the flat lenses to be fabricated on the

topside. Using the developed photoresist as an etch-mask, the silicon dioxide layer is plasma-etched to produce the windows. (c) Next, the topside protective layer of Si_3N_4 is cleared in hot phosphoric acid (85% H_3PO_4 at 165 °C for 5 minutes). (d) Now we start fabricating the flat lens on the topside. We deposit 200 nm thick layer of gold (using electron beam vapor deposition), followed by 400 nm thick SiO_2 (using PECVD). (e) We choose a bilayer resist for facilitating clean lift-off. The topside is coated with the photoresists LOR 3A followed by SPR 700. The resist bilayer is exposed using the stepper, ensuring each lens structure is accurately aligned with the previously etched backside windows. (f) Finally, 50 nm gold with an adhesion layer of 5 nm thick titanium is deposited using e-beam vapor deposition, and lifted-off in remover-PG. This results in the gold disks constituting each lens.

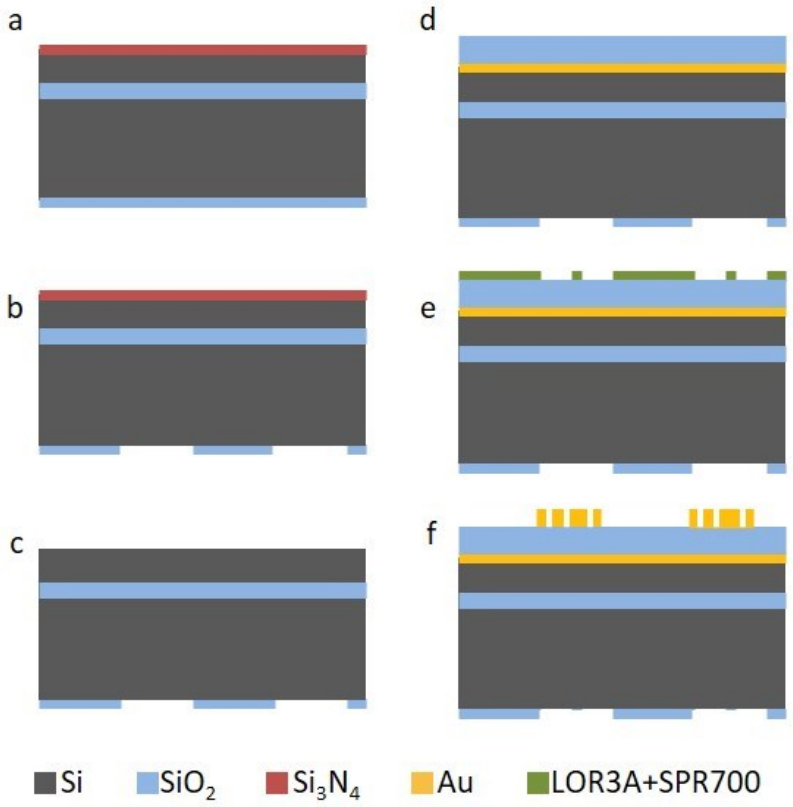

Figure 4-2 *Fabrication of the planar lens. (a) – (f) Process flow of photolithography as described in the text.*

Following the lens fabrication, the handle layer is removed using a dry-etch process based on xenon-difluoride, resulting in a reflective flat lens standing on top of a 2.8 μm thick membrane (Figure 4-1(g)). To integrate the flat lens with an external MEMS device, we "tear out" the lens from the thick SOI wafer. To do this, we start by etching the 600 μm thick handle layer in xenon difluoride (XeF_2). Xenon difluoride etch is a highly selective, isotropic, dry-etch process for silicon [131]. The backside window made with SiO_2 provides the entry point for the xenon difluoride gas to react with the bulk of silicon in the handle layer. Due to the excellent selectivity of XeF_2 to silicon versus SiO_2, the 200 nm thick buried-oxide layer of the SOI wafer also serves as the etch-

stop layer. The etching process is visually inspected in-situ until all the silicon directly beneath the lens is etched out, and the lateral extent exceeds the outer dimension of the lens. Figure 4-3 shows an optical image of the etched portion from the backside as well as from the topside. From the top, the shadow beneath the square lens structure indicates the area where silicon has been etched out. After the XeF_2 etch, we are left with a membrane that is only 2.8 μm in thickness and almost 1.35 mm in diameter.

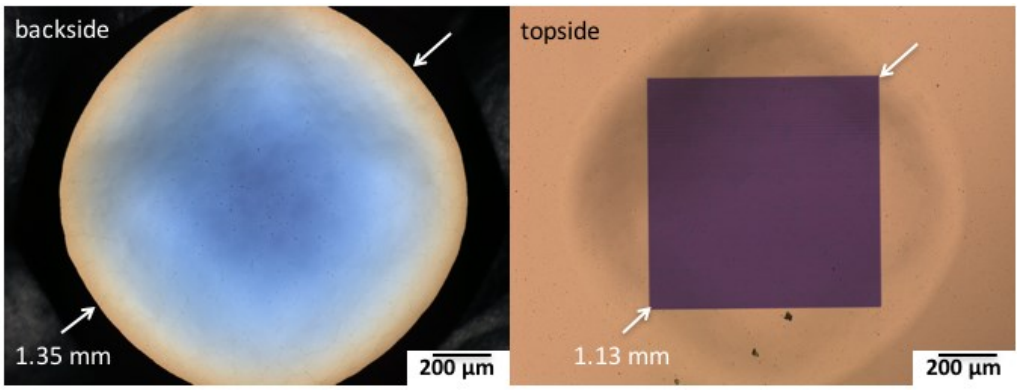

Figure 4-3 *Optical microscope image after etching of the SOI handle layer from the backside and from the topside. In the topside image, the thinned membrane is a circular shadow surrounding the square metasurface lens.*

For the next stage of fabrication, we use a focused ion beam (FIB) tool integrated with an Omniprobe micromanipulator needle to integrate the flat lens onto a 2D MEMS scanner. Figure 4-4(a) depicts the steps of the process. We trace the focused ions around the periphery of the lens to cut out most of the structure, except a small portion. Here we weld the needle-tip of the micromanipulator by depositing platinum. The remaining structure is subsequently released; the membrane is free from the surrounding solid substrate and is held only by the micromanipulator needle. We move the membrane out of the substrate and on to the MEMS platform by controlling

the micromanipulator arm. After the lens is placed and aligned with the central platform of the MEMS, it is glued by depositing platinum in small patches. Finally, the needle is cut away by milling with focused ion beam [132]. This practical technique allows for fusion welding of the flat lens to the MEMS device without the need for extra materials. Moreover, it enables the integration of hybrid structures fabricated with processes having different critical dimensions.

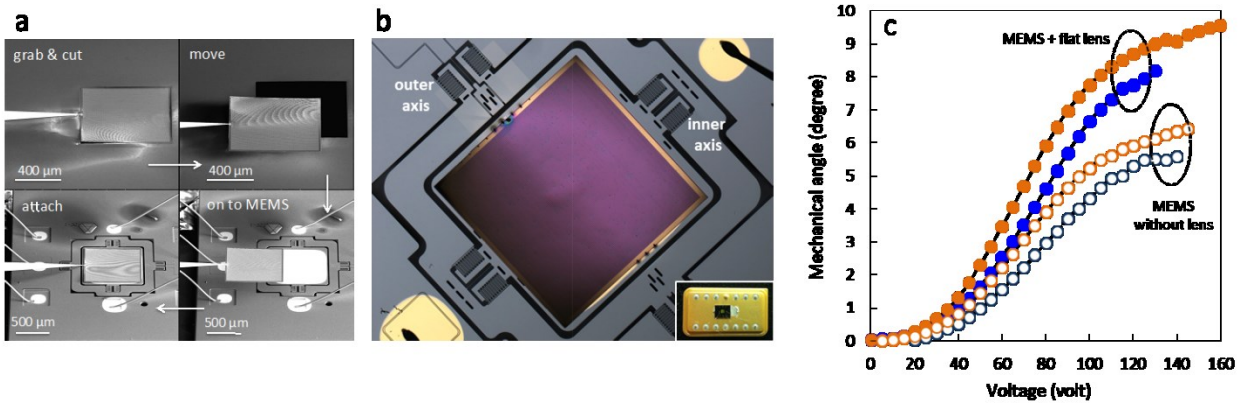

Figure 4-4 *Integration of flat lens onto MEMS: (a) Stages of integration of the metasurface-based flat lens with an external 2D MEMS platform. (b) Optical microscope image of a MEMS scanner with a flat lens on top. The two rotational axes of the scanner are indicated. The inset shows the device mounted on a dual in-line package ready for electrostatic actuation. (c) Angular displacement of the MEMS scanner with and without the metasurface-based lens. The orange circles represent the angular displacement when the inner axis is actuated, while the blue circles show the response when the outer axis is activated.*

An optical image of the 2D MEMS scanner with the integrated flat lens is shown in Figure 4-4(b). The scanner is gimbaled for achieving biaxial degrees-of-freedom and is actuated by electrostatic vertical comb-drives. Vertical comb-drives consist of stationary plates interspersed with rotating ones. When a potential difference is applied between these plates, the moving elements are pulled downward causing a rotation around a particular axis. Simple single-layer straight beams are used for torsional flexures on both inner and outer axes to give a two-

dimensional rotational degree-of-freedom. The micro-mirror is electrostatically rotated about the inner axis using the vertical comb drives mounted on the gimbal frame [127]. The gimbal frame rotates about the outer axis using the vertical comb drives mounted on its frame and substrate. For the devices reported here, the typical maximum angular displacement is close to ±9 degrees and the resonance frequency is of the order of 1 kHz about each torsional axis. The mirror dimensions are 1 mm x 1mm with a thickness of 10 μm. Although thicker device layers are desired for better flatness of mirrors and frame under dynamic deformation, they are also more difficult to fabricate due to the required high aspect deep reactive ion etching (DRIE) ratio and alignment issues. Simulations showed that 10 μm thick layers provide sufficiently large stable deflection range with minimal adverse effect on the performance of the device caused by the dynamic deformations of the rotating MEMS platform. To characterize the mechanical response of the flat lens-on-MEMS assembly, the device is mounted on a dual in-line package and electrostatically actuated to independently control either the inner or the outer axes as shown in Figure 4-4(b). Details of the MEMS platform and voltage connections are given in Figure 4-5. Figure 4-4(c) summarizes the mechanical response of the MEMS platform when a voltage is applied across each rotational axis. As the applied voltage is increased, the platform starts rotating until a saturating region is reached beyond which the comb drives cannot be moved further. We perform this experiment under an optical profilometer, capturing an image of the MEMS surface for each applied voltage. The rotation angle in the MEMS mirror is calculated with respect to a rigid part of the peripheral structure. The measurements are taken for bare MEMS, i.e. before the metasurface lens has been integrated, and for the same device after been loaded with the metasurface lens. As shown in Figure 4-4(c), even after the addition of the metasurface lens on top of the MEMS, the functional

dependence of the MEMS mirror remains the same. The increased angular dependence of the loaded MEMS is a consequence of using vertical comb drives for torsional actuation of the device. The incorporation of the flat lens onto the micro-mirror reduces the static gap between vertical combs resulting in a much larger angular deflection when actuated.

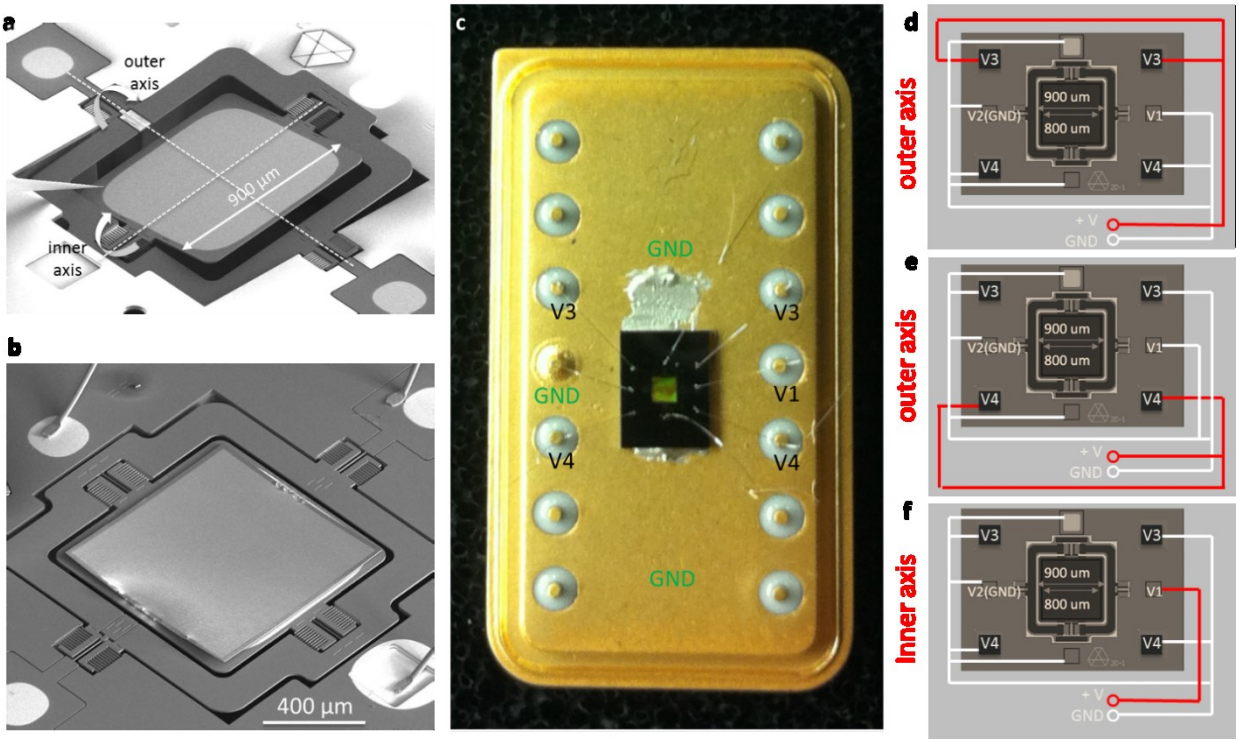

Figure 4-5 *(a) Scanning electron micrograph (SEM) of a bare MEMS platform with a square layout, each side measuring 900 µm. (b) SEM of a flat lens integrated with the MEMS platform shown in (a). (c) Photograph of the DIP where the MEMS-with-lens is attached with silver paste and wire-bonded appropriately. (d – f) Voltage connections (in red) for actuating outer or inner axis of the MEMS platform.*

4.2 Simulation and experiment

In the FDTD simulation (software package by Lumerical Inc.), only one row of nano-disc antennas is simulated and Bloch boundary conditions are applied in the y-directions. Figure 4-6(a) is the calculated distribution of the electric field intensity ($|E|^2$) near the focal region in the *x-z*

plane. The focal length is determined by the z value of the highest intensity point, which is indicated by the white dashed line at $z = f = 5$ mm. The focusing efficiency is estimated to be 83% which is calculated from the beam intensity at the focal region normalized to the source power. Figure 4-6(b) shows the beam profile at the focal region across the dashed line in Figure 4-6(a). The simulated discrete data points (blue circles) are fitted with a Gaussian curve (red line) to determine the full width half maximum (FWHM) of the focal beam size, which is 22.8 μm, which is slightly bigger than the diffraction-limited value (21.6 μm) due to the phase approximation of the 0 to 2π coverage.

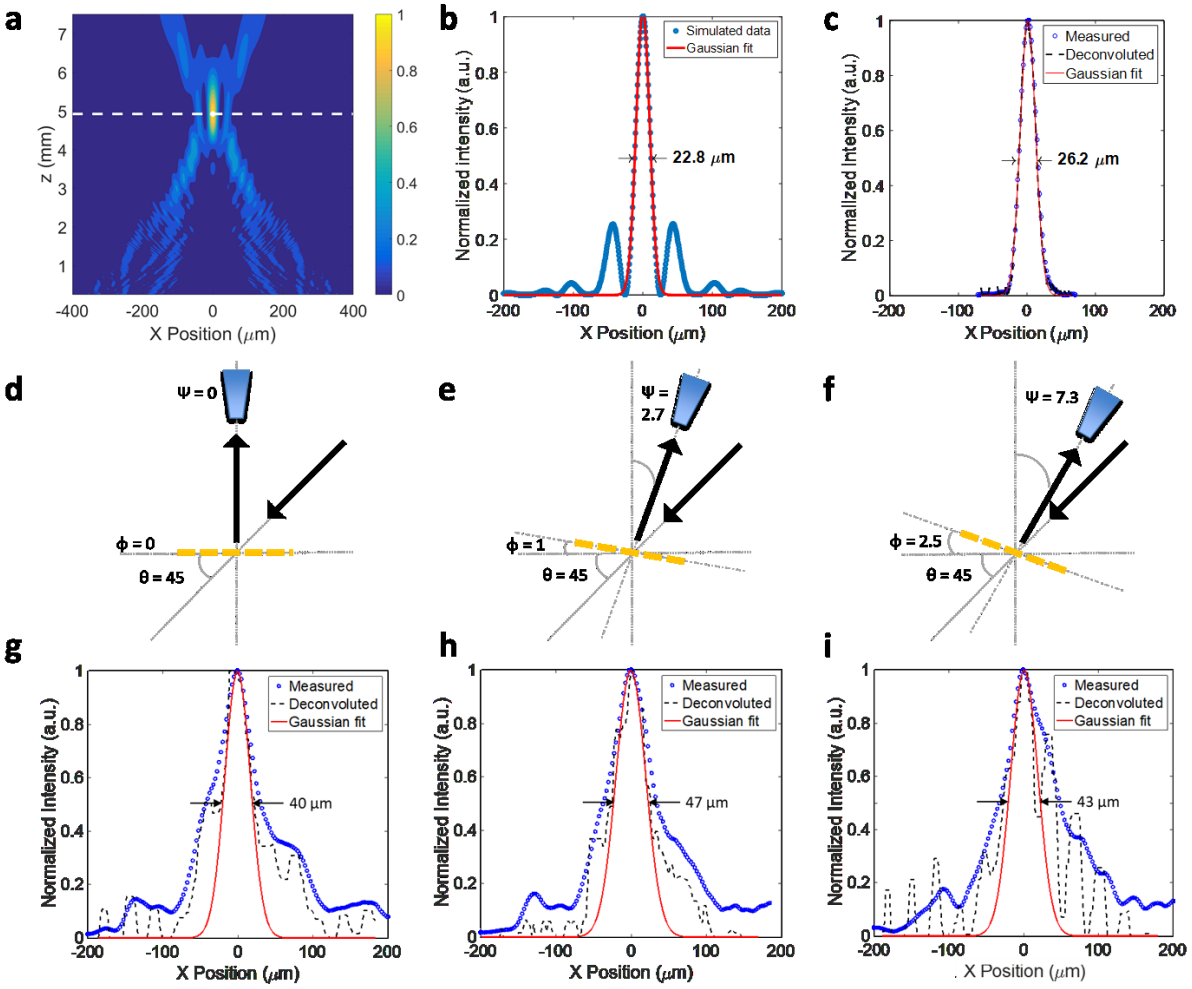

Figure 4-6 *(a) Simulation: distribution of the intensity (normalized $|E|^2$) of the reflected beam in the x-z plane at y = 0. The lens is centered at x = 0 and the size of the lens is from -0.4 mm to 0.4 mm. The white dashed line indicates the focal length. (b) Simulation: line scan of the focused beam profile at y = 0 and z = f = 5 mm along the white dashed line. (c) Experiment: translational scan of the reflected beam intensity (normalized $|E|^2$) measured at the center of the focal line. (d-f): Schematic of the three experimental configurations. The angle with respect to the vertical axis is fixed at 45°, while the MEMS platform is actuated to move the lens by 0°, 1°, and 2.5° respectively. To align with the peak of the reflected signal, the position of the detector needs to be at 0°, 2.7°, and 7.3° respectively. (g-i) Optical profile of the actuated lens-on-MEMS device. Experimentally measured translation scan for each of the three configurations. The FWHMs calculated from the Gaussian fits are comparable, though the asymmetry of the central peak changes with the tilting of the platform.*

For the experimental characterization, we use a continuous-wave Fabry-Pérot quantum cascade laser (QCL) (AdTech Optics) emitting at $\lambda = 4.6$ μm. The laser is mounted so that its output beam is s-polarized (electric field of the light is first sent through a pinhole before reaching the detector). Because of the small focused beam size, another dual-lens system is placed before the detector to expand by a factor of two the size of the focused beam. The signal-to-noise ratio is increased by modulating the intensity of the QCL with a small sinusoidal current superimposed on the direct current (Wavelength Electronics QCL1500) and demodulating the detected signal with a lock-in amplifier (AMETEK Advanced Measurement Technology). Figure 4-7 shows the schematic of the experimental arrangement. The ~3 mm laser beam is downsized by 2.5 times, such that the incident beam is only slightly larger than the 800 μm square lens. The light is incident at 45° to the lens surface. The lens reflects the incident beam at 0° and focuses the light at 5 mm away from its surface. The focused light is magnified 2 times by the lens pair L3 and L4 and the intensity is detected by a thermo-electrically cooled mid-IR detector through a pinhole. The detector, L3 and L4 sit on a rotational stage so that the angle can be adjusted. There is also a translational stage for the detector to scan the reflected beam.

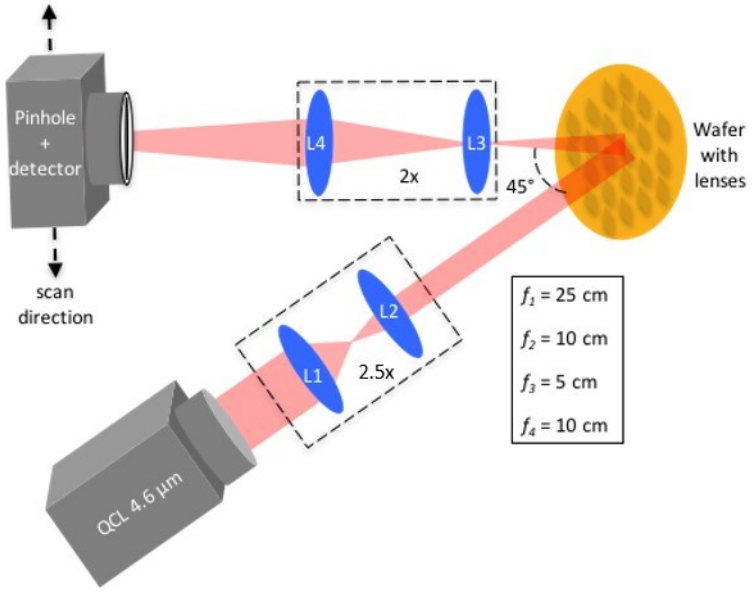

Figure 4-7 *Schematic showing experimental arrangement used for characterization of the optical response of a flat lens.*

The focus is characterized experimentally by translational scans. The data are taken at the center of the focal line, i.e. $y = 0$. The average standard deviation of repeated measurements is 0.2%. Note that the detector is scanned across the focus in 2 µm steps, which is smaller than the pinhole diameter (10 µm). So, the raw data is de-convoluted to retrieve the original beam profiles. Figure 4-6(c) shows the measurement results of the metasurface lens on a solid substrate. The FWHM is 26.2 µm, which is close to the simulated value. The difference is possibly due to fabrication errors and the M^2 factor of the QCL not being 1 (M^2 = 1.2). The side lobes in Figure 4-6(b) are not observed because of the increased FWHM in Figure 4-6(c).

The optical focusing performance of the metasurface lens integrated with the MEMS is experimentally characterized using the same set up as described above. The angle of the incident light is kept fixed at 45◦. The profile of the reflected focal line is measured for three positions of

the MEMS platform: actuating voltages of 0 V, 40 V, and 60 V are applied across the outer axis such that the lens tilts by 0◦, 1◦, and 2.5◦ respectively (Figure 4-6(d) – (f)). The measured FWHM of the focal lines for the three tilted positions of the lens are shown in Figure 4-6(g) – (i) respectively. For each position of the lens, the detector is rotated to align with the peak intensity of the reflected light. To measure the beam profile, a translational scan is performed across the rotated focal line position with a 30 μm pinhole in 5 μm steps. For the designed 0◦ position of the MEMS platform, when compared to the lens on the solid substrate (Figure 4-6(c)), we observe an increase in FWHM. This is attributed to the non-flatness of the lens when released from the solid substrate. Another factor is that when the device plane is rotated, the incident angle is no longer the same as the designed angle (45^{o}), hence it introduces phase errors affecting the focusing performance. However, tilting the integrated lens up to 2.5◦ preserves the focused beam profile, as well as the measured FWHM in general. For dynamic coma correction, one would rotate the device plane according to the change of incident angle so as to keep the incident angle constant. The simulation is performed assuming a flat substrate. The definitions of various terms are given in Figure 4-8(a). The results are summarized in Figure 4-8(b) with details given in Figure 4-8(c) – (f). The measured values are presented in Figure 4-6. The discrepancy between the calculated and measured reflective angles is likely due to the non-flatness of the lens.

a

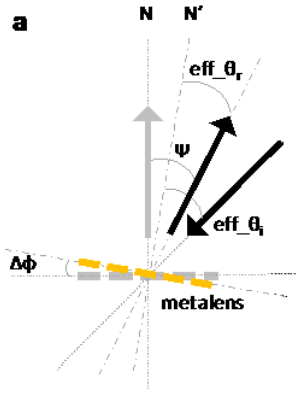

b

MEMS tilt Δϕ (°)	detector shift ψ (°)	metalens eff_θi (°)	metalens eff_θr (°)	
			calculated	measured
0	0	45	0	0
1	2.7	44	0.7	1.7
2.5	7.3	42.5	1.7	4.8

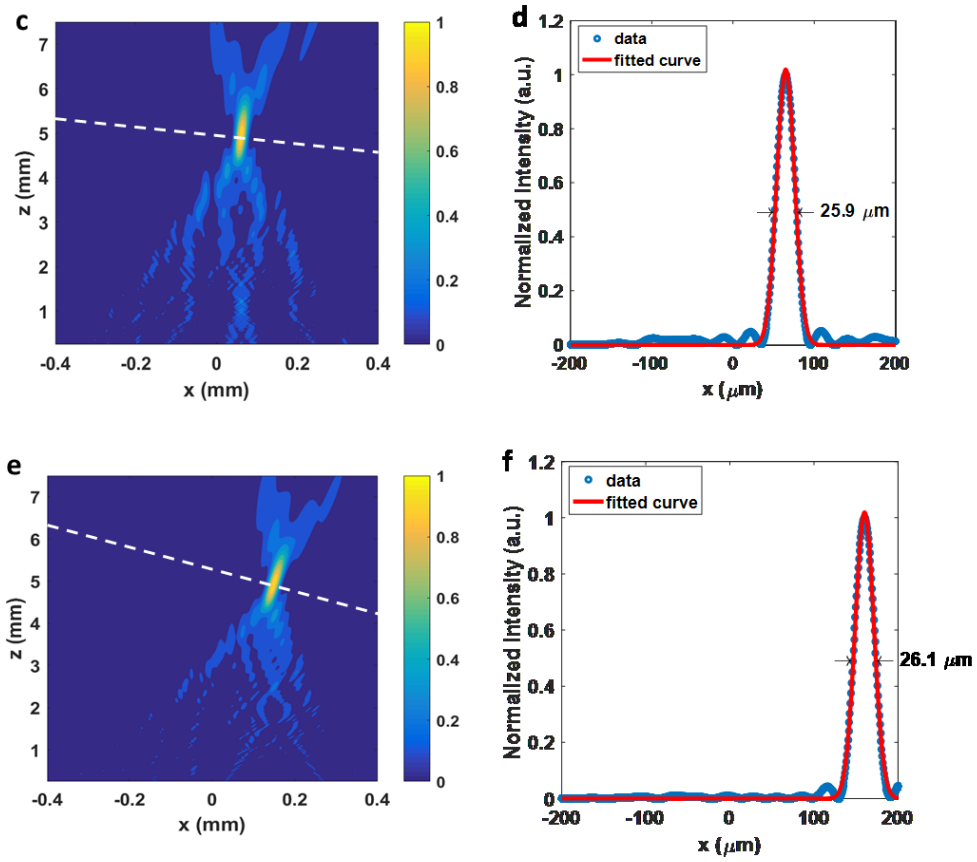

Figure 4-8 *(a) Schematic for defining the effective incident angle and effective reflective angle, when the lens is tilted. (b) Table comparing calculated (for a flat lens) and measured (for a non-flat lens) effective reflective angles for three different tilt angles of the MEMS platform. (c)-(f) FDTD simulation of reflected beam intensity and the line cut at the focal length for tilt angle (c) and (d) 1° and (e) and (f) 2.5° respectively.*

In order to quantify the effect of the curvature of the MEMS scanner on the flat-lens performance, we measure the curvature of the micro-mirror using an optical profilometer and simulate the performance of a cylindrical lens on top of a substrate having the same curvature as the MEMS scanner (Figure 4-9). The results are shown in Figure 4-10. When supported by the curved substrate, the focal length of the lens becomes 8.9 mm compared to the designed value 5 mm. The reflected beam path is at 0.5^{o} compared to the designed value 0^{o}. The FWHM becomes wider, 41.7 μm compared to 22.8 μm on a solid substrate, in reasonable agreement with the results reported in Figure 4-6(g) – (i). Hence, our simulation confirms that the curvature of the MEMS substrate is the main parameter affecting the performance of the lens. This can be understood intuitively that the MEMS substrate is curved down in the negative z-direction which diverges the incident light, hence the focal power of the lens is effectively decreased resulting in an increase in both the focal length and focal spot size. However, we would like to point out that the effect of non-flatness of the substrate depends heavily on the substrate curvature. For example, if we were to consider the curvature in Figure 4-8(d), the effect of a sloped surface is like introducing a small angle deviation to the incident beam, which will be smaller compared to the effect of Figure 4-8(c). The analysis of the effect of changing the incident angle can be found in [16].

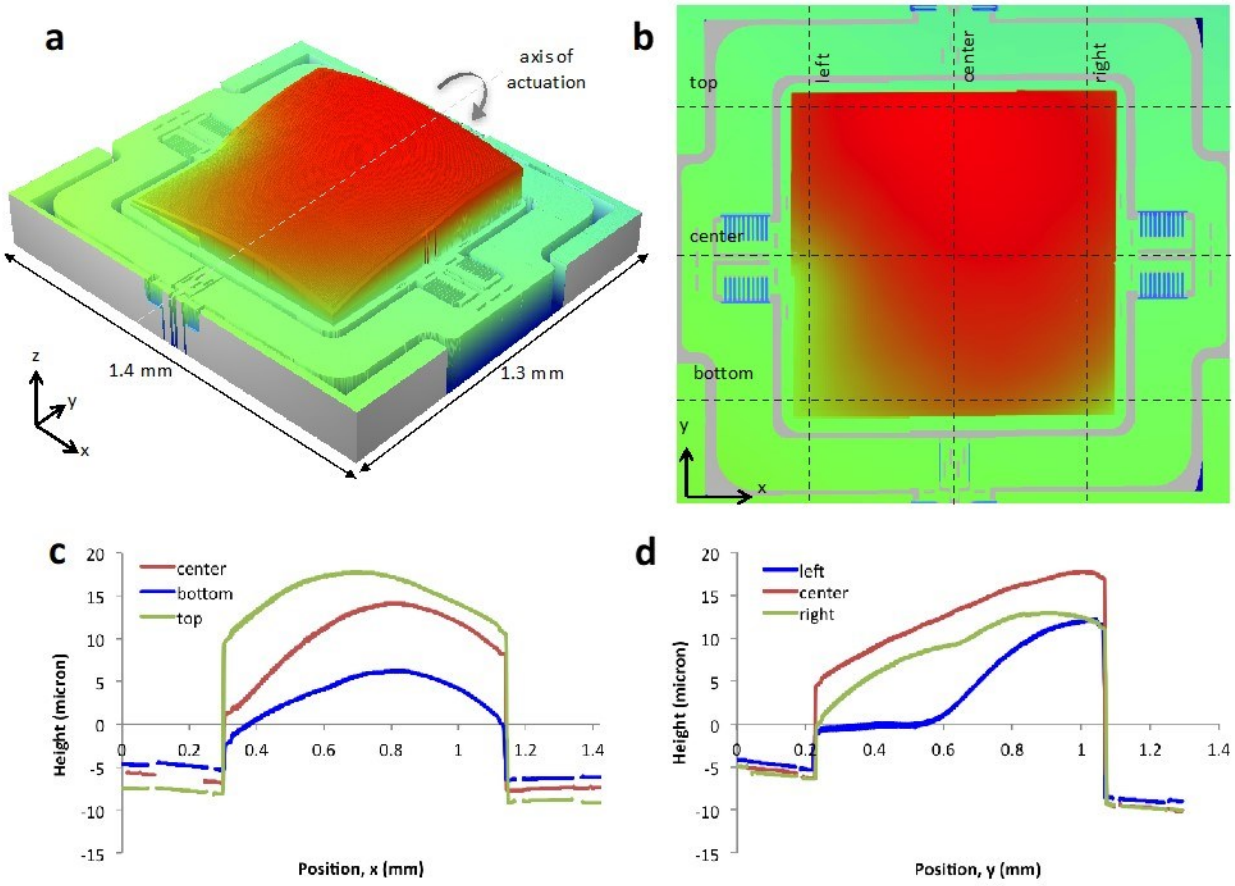

Figure 4-9 *(a) 3D topography of the integrated lens device measured with an optical profilometer. The green surrounding region indicates the flatness of the MEMS frame. Red indicates higher regions. (b) 2D top view of the device topography. (c) and (d) shows the height distribution measured along the dashed lines marked in (b) in the x and y-direction respectively.*

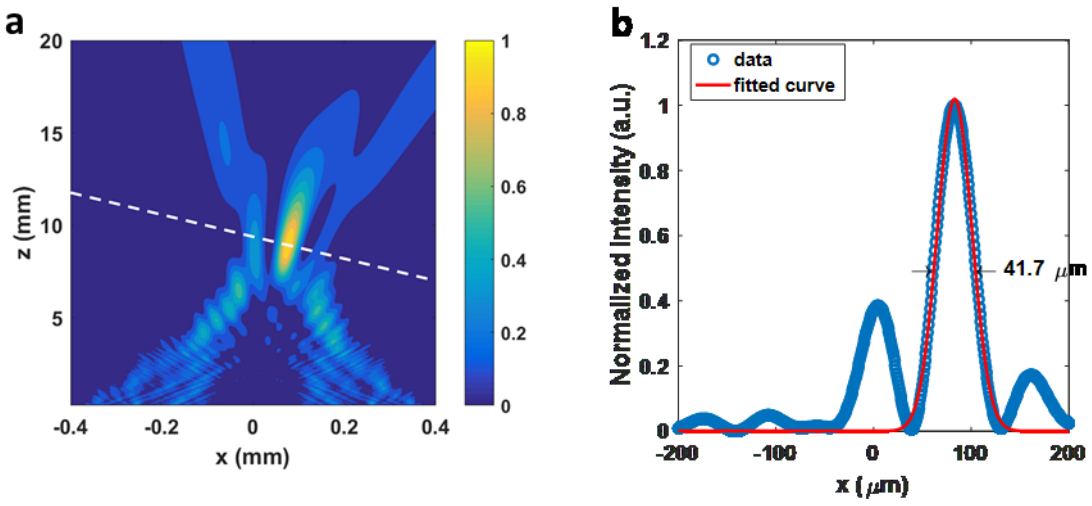

Figure 4-10 *(a) Distribution of the intensity (normalized $|E|^2$) of the reflected beam in the x-z plane at y = 0 with a curved substrate. The white dashed line is perpendicular to the reflected beam path. (b) Simulation: line scan of the focused beam profile along the white dashed line. (c) Experiment: translational scan of the reflected beam intensity (normalized $|E|^2$) measured at the center of the focal line.*

Figure 4-11 summarizes the study on the hysteresis of the integrated lens device. Light is incident at 45◦ and the detector is fixed at 0◦ aligned with the peak intensity of the reflected beam when no voltage is applied. The voltage is increased across the outer axis of the MEMS from 0 V to 140 V in 10 V steps and then decreased back to 0 V. As expected, for each applied voltage, the lens position tilts which in turn causes the reflected focal line to rotate away from the detector at 0◦. The decreasing intensity of the reflected beam with increasing voltage, as measured by the detector, is depicted in Figure 4-11(a). As the voltage is decreased back to 0 V, the intensity increases following the same path, suggesting no or minimal hysteresis of the MEMS-integrated lens. This shows that such dynamic optical devices can be useful in scanning systems. Figure 4-11(b) re-plots the same data as shown in Figure 4-11(a), but in terms of the tilt angle of MEMS deduced from mechanical characteristics presented in Figure 4-6.

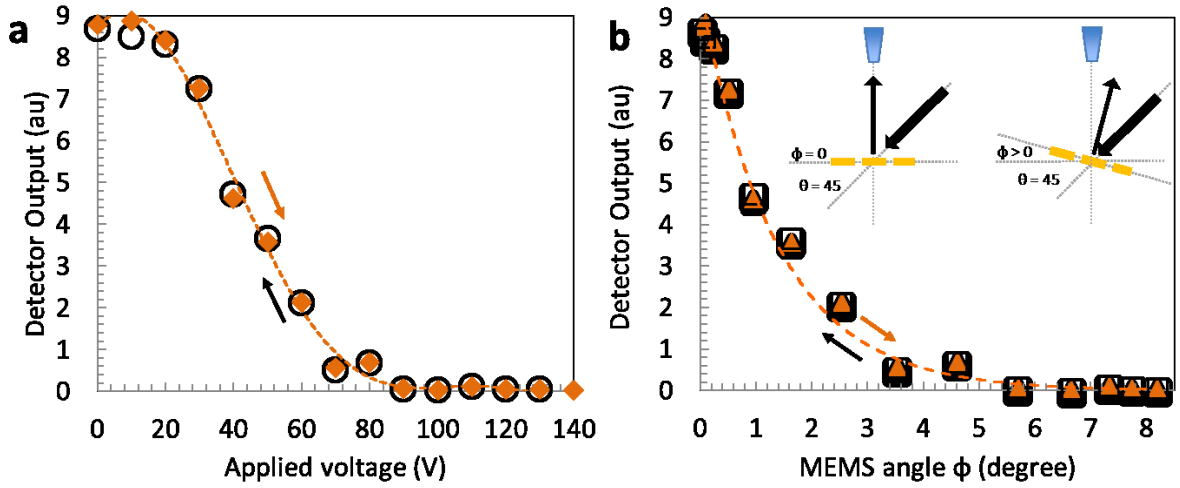

Figure 4-11 *(a) Change in focal intensity with electrostatic actuation of the MEMS. The applied voltage is increased up to the saturation region and then decreased back to zero to study hysteresis if any. The light is incident at 45°, while the detector is kept fixed at 0°. (b) Data measured in (a) plotted in terms of the mechanical angle of the integrated device. The inset shows the two configurations used for collecting the data.*

4.3 Summary

We have presented a MEMS-integrated metasurface lens. The device can be electrically controlled to vary the 2D angular rotation of a flat lens and hence the position of the focal spot by several degrees. This proof-of-concept integration of metasurface optical devices with 2D MEMS scanners can be extended to the visible and other parts of the electromagnetic spectrum implying the potential for application across wider fields, such as MEMS-based microscope systems for point-of-care *in vivo* applications, holographic imaging, LIDAR scanners, laser printing and so on. Dense integration of thousands of individually controlled lens-on-MEMS devices onto a single silicon chip would lead to the creation of a new type of reconfigurable fast digital spatial light modulators [107] that would allow an unprecedented degree of control and manipulation of the optical field.

Chapter 5
Reconfigurable metasurface devices based on dielectric elastomer actuators (DEAs) in SWIR

There has been a wide variety of work on tunable optical devices, in particular, tunable-focus lenses (i.e., varifocal lenses), with important applications in imaging and adaptive vision. State-of-the-art technologies include the following: Conventional optical zoom, involving translating rigid elements, is bulky and inertially limited in speed [133], [134]. Liquid crystal spatial light modulators with transparent electrodes made of indium tin oxide are high speed and use low operating voltage but are limited in resolution and polarization dependence [135], [136]. Fluid based tunable lenses are high speed and have a wide tuning range, but the control of the exact surface curvature is difficult, and coma has been observed when placing the lens vertically, due to gravity [137]–[142]. Tunable acoustic gradient index lenses use acoustic waves to generate an oscillating refractive index profile, which can be tuned at high speeds (~μs) but must operate in a stroboscopic mode [143], [144].

Mechanically-tunable metasurfaces have been reported recently, in which metasurfaces are embedded in stretchable substrates, such as a 1.7X zoom lens [145], a reconfigurable hologram [146], and tunable lens with focusing efficiency above 50% [26]. However, all of these were much less than a millimeter in size and required external apparatuses to generate mechanical strain, restricting their applications.

In this chapter, we introduce a new approach, in which metasurfaces can be made electrically tunable by combining them with a class of electroactive polymers known as dielectric elastomer actuators (DEA) [19], [147]. Large biaxial and reversible strains at relatively high speed

can be produced by applying an electric field and the biaxial strain is directly compatible with 2D metasurfaces. By using different electrode configurations, they can be used to alter the size, shape, and lateral translations of a metasurface bonded to the elastomer. We show the potential of this approach in performing simultaneous tuning of focal length, astigmatism correction, and image shift control. This brings the familiar tuning capabilities of electron microscopes to flat optics. It also enables long sought-after applications, in which dynamic and high-speed tuning can be achieved with voltage-resolved precision in an analog or digital manner at the millisecond time scale.

5.1 Wavefront shaping with stretched metasurfaces

A flat lens can be constructed using the following hyperboloidal phase profile:

$$\phi(r) = \pm k\left(\sqrt{r^2 + f^2} - f\right), \tag{14}$$

where k is the wavenumber ($k = 2\pi n/\lambda$, where n is the refractive index of the medium in which the lens is immersed and λ is wavelength), r is radial position, f is focal length, and the sign is positive or negative for diverging or converging lenses, respectively (Figure 5-1(a)). This phase profile focuses light free of spherical aberrations for normal incidence (infinity-corrected) illumination. We combine the metasurface lens with a DEA, to make the metasurface tunable, which was, by itself, a static device.

The DEA, sometimes referred to as “artificial muscles” in soft robotics, is effectively a compliant parallel plate capacitor [148]. By using a soft elastomer (e.g., polyacrylate and silicone rubbers), as a dielectric together with transparent, stretchable electrodes, the dielectric is compressed in the electric field direction (thickness direction) when a voltage is applied. As

elastomers conserve volume on deformation (i.e., Poisson ratio close to 0.5), the thinning results in lateral or areal expansion that can be very large, up to 500% [149]. The attainable actuation strain is a function of the electrostatically-induced Maxwell stress, the constitutive deformation behavior of the elastomer, and mechanical configuration of the elastomers and electrodes [150].

By bonding the metasurface lens to the dielectric elastomer, the in-plane (lateral) deformation of the metasurface lens is coupled to the voltage-induced stretching of the elastomer, which is uniform over the electrode area. This uniform stretching effectively scales the lateral coordinates of the lens by a stretch factor, s ($s = 1 + \epsilon_L$, where ϵ_L is lateral strain), such that $r \rightarrow r/s$:

$$\phi_{stretched}(r, s) = \pm k\left(\sqrt{(r/s)^2 + {f_0}^2} - f_0\right), \quad (15)$$

where f_0 is the focal length without actuation, provided that metasurface elements retain their original, individual phase responses, and only their separation is increased (Figure 5-1b). While this stretched phase profile is not of the same form as Equation (14) (a radially varying stretch profile, $s_{radial}(r)$, would be required), it is closely approximated by the following ideal phase profile:

$$\phi_{ideal}(r, s) = \pm k\left(\sqrt{r^2 + (s^2 f_0)} - s^2 f_0\right), \quad (16)$$

in which the focal length of Equation (14) is replaced by stretch-dependent focal length, $f(s) = s^2 f_0$. ϕ_{ideal} produces a focal length change that scales quadratically with stretch while maintaining the hyperboloidal shape necessary to be free of spherical aberration. The voltage applied to a DEA alters the focal length in the following way:

$$\frac{f}{f_0} = \frac{1}{1-\left(\frac{\epsilon}{Y}\right)\left(\frac{V}{t}\right)^2}, \tag{17}$$

where V is and voltage, and ϵ, Y, and t are the permittivity, Young's modulus, and dielectric layer thickness, respectively.

In tunable systems, optical aberrations may be augmented or reduced by tuning. With metasurface lenses, spherical aberration using normal incidence illumination is corrected by design. However, when such a metasurface is deformed, the resulting aberration is not obvious. The wavefront aberration function ($WAF = \phi_{stretched} - \phi_{ideal}$) quantifies the deviation of the resulting phase profile of the stretched metasurface from the ideal phase profile:

$$\begin{aligned} WAF &= \pm k\left(\sqrt{(r/s)^2 + {f_0}^2} - {f_0}^2\right) \mp k\left(\sqrt{r^2 + (s^2 f_0)^2} - s^2 f_0\right) \\ &= \pm k\frac{(1-s^2)r^4}{8f^3 s^6} + O(r^6). \end{aligned} \tag{18}$$

This equation shows that as the uniform stretch is increased from $s = 1$, the WAF increases from 0 until reaching a maximum aberration at $s \approx 1.22$ (e.g., for a lens ⌀6 mm, f = 50 mm, the maximum aberration is <0.05 rad at the edge). Upon further stretching, a built-in suppression of spherical aberration comes into effect, in which Equation (18) decays following a quartic function, $(r/s)^4$. This allows for highly tunable lens devices with excellent immunity to aberration.

In practice, an infinite number of aberrations exist and can be quantified in terms of Zernike polynomials. In most cases, the lowest eight terms are sufficient: piston, tip, tilt, defocus, oblique astigmatism, vertical astigmatism, vertical coma, and horizontal coma. Because Zernike terms are linear and orthogonal, specific or multiple optical aberrations can be targeted and tuned by

introducing the appropriate strain field to the phase profile. The application of stress of a particular configuration induces a strain field, resulting in a displacement field. The displacement field can be regarded as the sum of deformation ($\boldsymbol{A}$) and a rigid body displacement ($\boldsymbol{B}$) components, in which the transformed coordinates can be expressed in the following way: $\boldsymbol{x'} = \boldsymbol{A}(\boldsymbol{x}, \eta) + \boldsymbol{B}(t)$, where η is a parameterization (e.g., stress, voltage) and $\boldsymbol{x}$ and $\boldsymbol{x'}$ are the original and transformed coordinates, respectively. For metasurfaces, this reduces to a 2D problem, in which the phase profile coordinates transform: $\phi(x, y) \rightarrow \phi(x', y')$. The rigid body displacement is simply a shift in the x,y plane of the entire phase profile (Figure 5-1d), while the deformation changes the shape or size, opening up opportunities for generating new phase profiles through tuning the strain field. In the case of asymmetric biaxial strain, the lateral coordinates of the phase profile transform as follows $(x, y) \rightarrow (x/s_x, y/s_y)$:

$$\phi = \pm k\left(\sqrt{(x/s_x)^2 + (y/s_y)^2 + {f_0}^2} - f_0\right), \tag{19}$$

where $s_x \neq s_y$ ($s_x = s_y$ is uniform stretching). Here light propagating along two perpendicular planes experience different focal lengths, which is astigmatism (Figure 5-1(c)).

Using the voltage-induced strain field, it is possible to create the optical analog of image shift and stigmators found in scanning and transmission electron microscopes, which shape the electron beam dynamically. In optical systems, astigmatism can be performance-limiting, and sources of astigmatism often stem from geometric imperfections, such as misaligned, malformed, or strained lenses. Optical shift and astigmatism tuning is particularly useful in systems with that components move or deliberately utilize these parameters to extract additional information.

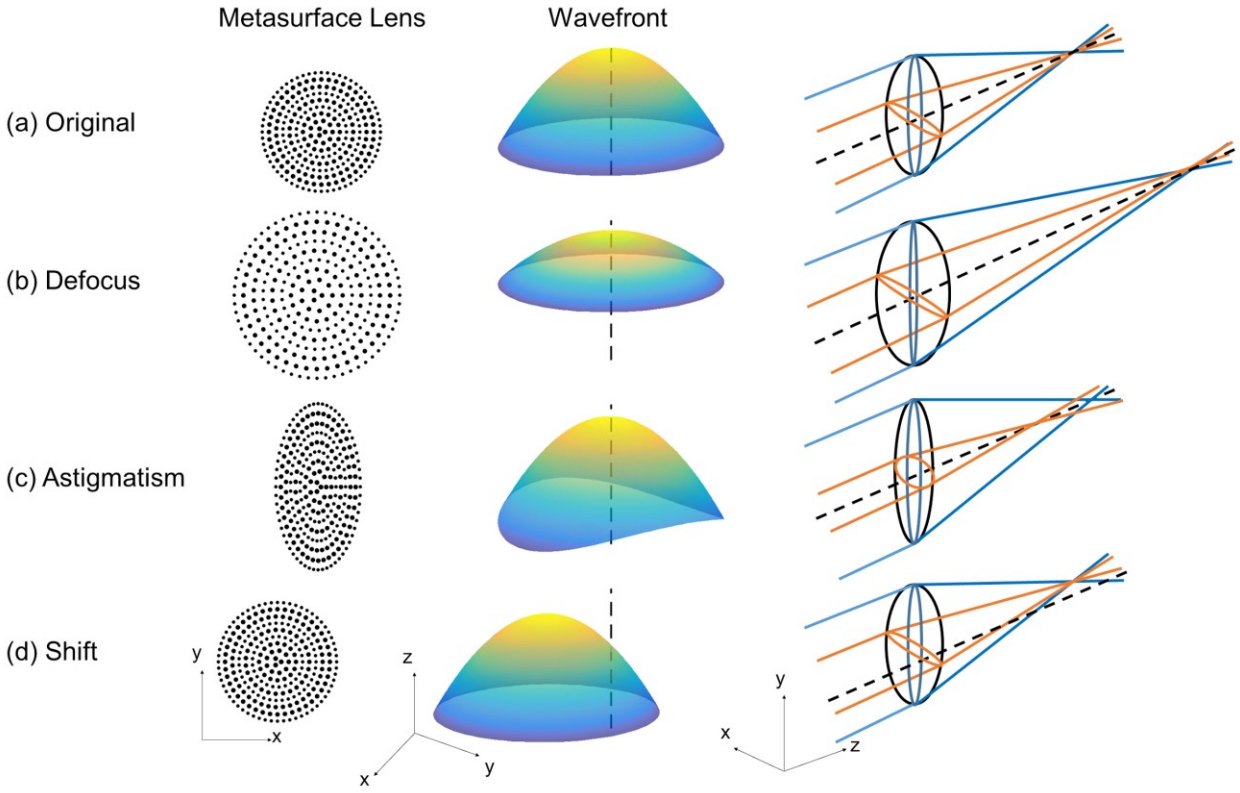

Figure 5-1 *Design of tunable metasurface lens. An illustration of a metasurface (left column) is constructed by digitizing an analog optical phase profile on a flat surface into discrete cells, each of which contains a metasurface element that locally imparts the required phase shift to the incident light in order to reconstruct the desired wavefront (middle column, dotted line is optic axis). The wavefront generated by the metasurface determines the subsequent beam shaping (right column). A periodic, radial gradient structure can be seen in the metasurface illustration, corresponding to 0 to 2π phase modulation, similar to the rings of a Fresnel lens. Rows: (a) A metasurface with a hyperboloidal phase profile following Equation 1 will focus normal incidence light to a point at distance corresponding to the focal length. Light rays traveling along the x, z and y, z planes (red and blue lines, respectively) will both be focused to the same point. (b) When the metasurface is stretched uniformly and isotropically, the phase profile widens and shallows, and this is seen in the outgoing wavefront (i.e., isophase surface), resulting in an extended focal length. Conversely, if the metasurface is compressed, the focal length would reduce. (c) When the metasurface is asymmetrically stretched (here stretched and compressed in the x and y directions, respectively), astigmatism is produced, such that light rays traveling along the x, z and y, z planes experience different focal lengths. (d) When the metasurface is displaced laterally in the x, y plane, the entire phase profile and hence focus position is correspondingly laterally shifted.*

5.2 Device design and characterization

The lens was fabricated using photolithography in a prepared film stack (see Figure 5-2(a)). By attaching the DEA to the sample surface and dissolving the sacrificial layer in water, the metasurface was transferred to the DEA. Electrical leads were then attached to apply control voltages. The final device includes a metasurface lens with a diameter of 6 mm. We designed and fabricated a polarization-insensitive, converging metasurface lens with a diameter of 20 mm and a focal length of 50 mm for a wavelength of 1550 nm based on Equation (14). The metasurface consisted of amorphous (a)-Si circular posts (Figure 5-2(b)). The data file for the photomask pattern generator was created using an algorithm we recently developed for efficiently generating large area metasurface designs with an extremely large number of densely-packed polygons [151]. We constructed the DEA using transparent polyacrylate elastomers (VHB 4905, 3M) with stretchable-transparent electrodes made of single-walled carbon nanotubes (SWCNT) [152]. These were measured to exhibit large transparency windows in the visible, near-infrared, and mid-infrared spectra.

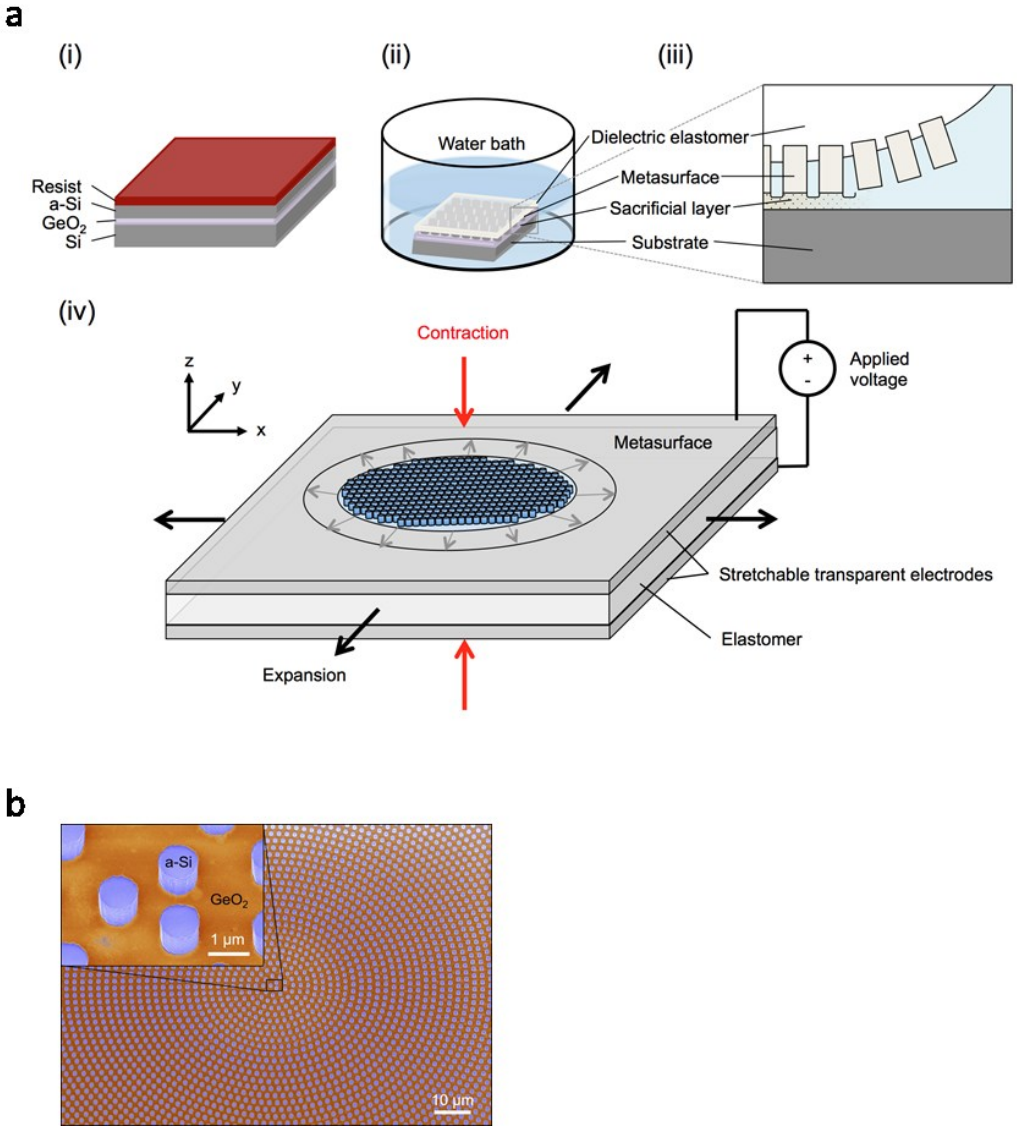

Figure 5-2 *Dielectric elastomer actuator platform. (a) Fabrication steps: (i) Schematic of the thin-film stack prepared for photolithography. (ii) After patterning and etching, the stack is attached to an elastomer layer and the whole stack is immersed in a water bath. (iii) Schematic of the release process showing the dissolution of the sacrificial layer (GeO_2) from the outer edge of the device towards the center, leaving the metasurface structure attached to, and supported by, the elastomer layer. (iv) A schematic of metasurface and DEA combination in which an applied voltage supplies the electrode layers (SWCNTs) with electrical charges. Their electrostatic attraction compresses the elastomer in the thickness direction and causes expansion in the lateral direction. (b) False-colored scanning electron microscope image of the center of the lens shows a-Si posts on the GeO_2 sacrificial layer before attaching to the elastomer layer.*

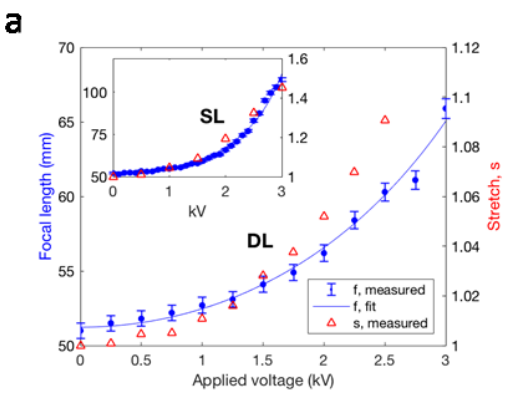
a
Focal length (mm)
Stretch, s
Applied voltage (kV)
SL
DL
kV
f, measured
f, fit
s, measured

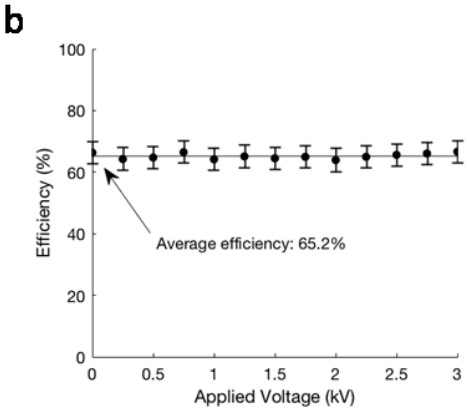
b
Efficiency (%)
Average efficiency: 65.2%
Applied Voltage (kV)

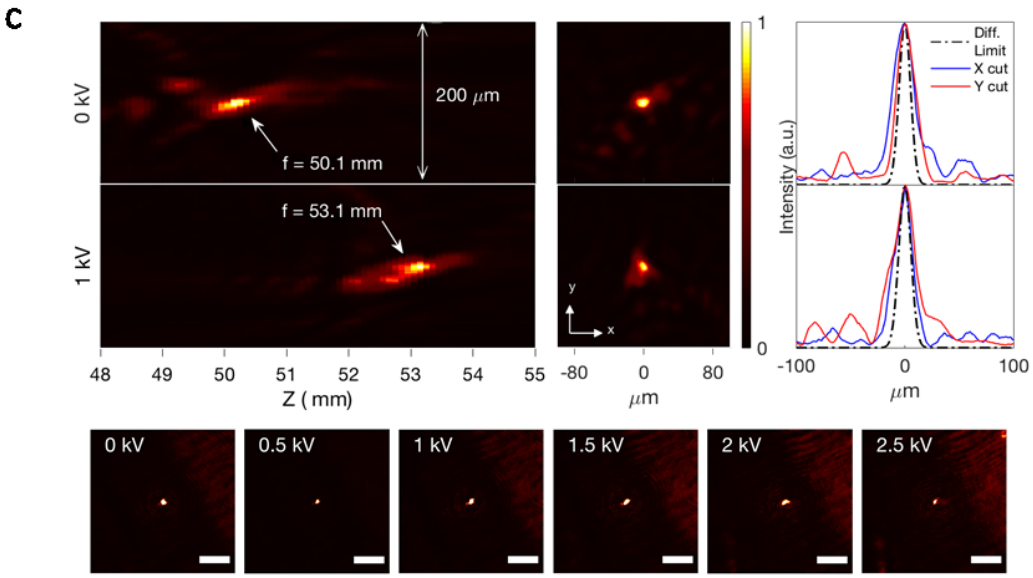
c
0 kV
1 kV
200 μm
f = 50.1 mm
f = 53.1 mm
Z (mm)
μm
Intensity (a.u.)
Diff. Limit
X cut
Y cut
0 kV
0.5 kV
1 kV
1.5 kV
2 kV
2.5 kV

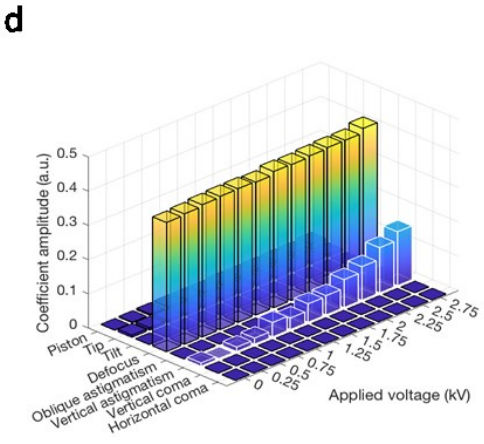
d
Coefficient amplitude (a.u.)
Piston
Tip
Tilt
Defocus
Oblique astigmatism
Vertical astigmatism
Vertical coma
Horizontal coma
Applied voltage (kV)

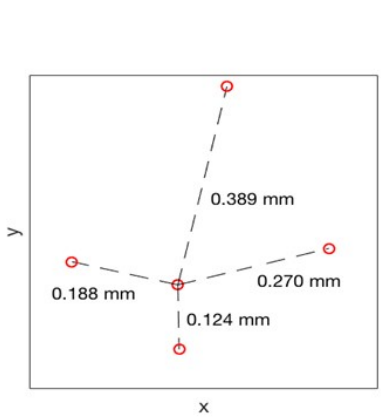
e
0.389 mm
0.188 mm
0.270 mm
0.124 mm
y
x

Figure 5-3 (Continued) *(a) Measurement of focal length tuning using center electrode V_5. Blue dots with error bars (standard deviation): Optical measurement of device focal length as a function of applied voltage. Solid blue line: fit focal length data to Equation 3, showing good agreement (R^2 = 0.9915). Red triangles: Measurement of stretch as a function of the applied voltage. (b) Measured focusing efficiency with error bars (standard deviation) as the voltage is varied. (c) The focus profile was scanned using a microscope objective (10x magnification) at two different voltages: 0 kV (top) and 1 kV (bottom). (Left) Z-scan of the intensity profile showing two distinct focal lengths. (Center) Image of focal spot intensity profile, i.e. x-y cross sections at the position of maximum intensity. (Right) Line scans of focal spot intensity image in the x (blue) and y (red) directions in comparison to the theoretical diffraction-limited spot size (black). Bottom: Also shown are the images of the focal spots at 0 through 2.5 kV captured directly by the camera without the microscope objective (scale bar: 500 μm). (d) As the applied voltage is tuned using the x-stigmator electrode configuration, the measured Zernike coefficients of the phase profile are plotted, showing targeted tuning of vertical astigmatism, while other Zernike coefficients exhibit little change throughout the tuning range. The defocus value accounts for the original focusing power of the lens. (e) Measurement of X,Y-shift control as 1.9 kV applied, showing two-axis control over displacement from the focus position (center red circle) at 0 kV.*

Two types of devices were fabricated and measured, a single layer (SL) and double layer (DL) device. While the SL demonstrated better tunability than the DL, most of the data presented are of the DL, due to it being higher quality. DEA induced stretch was observed from optical microscope images of the center of the lens. The Fourier transforms (FT) of the DL images were used to quantify the stretch (Figure 5-3(a)), in which we measured the radii of the first order annulus of FT, corresponding to the reciprocal space representation of the radially symmetric post-to-post separation. With the same applied voltage, the DL was stretched less than SL, on account of the greater stiffness introduced by the larger intermediate elastomer layer. The maximum voltage used was 3 kV, which produced s = 1.41 (SL) and 1.15 (DL).

The focal lengths were measured by scanning a camera along the z-axis for different applied voltages. From f = 50 mm without actuation, the DL focal length was tuned by 15 mm (30%, $\Delta f / f_0$) as the voltage was increased from 0 to 3 kV (Figure 5-3(a)) and closely followed

the predicted relation with voltage (Equation (17)). The SL displayed a greater, 107% focal length modulation upon varying the voltage from 0 to 3 kV (Figure 5-3(a), inset). The focusing efficiency, defined as the ratio of the focused optical power and the incident power, was measured for the DL and showed a high average efficiency of 62.5% with minimal variation throughout the tuning range (Figure 5-3(b)). For comparison, the measured focusing efficiency of the metasurface before transfer (fabricated on a fused silica wafer) was 91%, and the difference was attributed scattering and absorption by the DEA as well as imperfections in the transfer process. Images of the focus were taken to investigate the effect of aberrations upon tuning. Since the sizes of the beam (⌀7 mm) and lens (⌀6 mm) were comparable, the illumination profile impinging on the lens was Gaussian rather than a plane wave, causing the Airy pattern to not manifest by apodization. In the absence of any applied voltage, the measured focal spot size ($1/e^2$ full beam waist) was 34.4±1.1 μm, compared to the theoretical diffraction-limited spot size of 21.4 μm (⌀6 mm, f=50 mm, M^2=1.3). At 1.0 kV, the measured focal spot size was 37.7±2.8 μm, compared to a diffraction-limited spot size of 22.7 μm (⌀6 mm, f=53 mm, M^2=1.3). Possible reasons for this difference include errors introduced during fabrication and the transfer process. In particular, it is likely that a non-uniform strain field was created as the elastomer membrane was initially pressed onto the metasurface, resulting in small distortions in the final device. Optical performance can be improved by optimizing these procedures. The focal spot sizes were within their measurement errors indicating that the focal spot size, although not diffraction-limited, was maintained on tuning. Due to setup constraints, images of the focal spots at higher voltages (> 1 kV) were obtained directly by the camera without magnification (Figure 5-3(a), bottom). It was clearly seen that the focal spot maintains its shape even at high voltages.

We measured the x stigmator (Figure 5-3(d)), which squeezed the phase profile into an elliptical shape by contraction and expansion in the x and y directions, respectively. The image FT was then used to quantitatively measure the strain field, showing asymmetric yet spatially uniform biaxial strain: a requirement for good stigmator performance. The resulting astigmatism tuning was calculated by taking the Zernike transform of stretched phase profile (Figure 5-3(d)).

We measured the x, y-shift and were able to shift the image in the up, down, left and right directions by applying appropriate control voltages (Figure 5-3(e)). The observed asymmetry of the control is most likely due to some residual asymmetrical stiffness around the periphery of the device. This asymmetry occurred during fabrication, as three different structures needed to be concentrically aligned: the outer frame, electrodes, and metasurface. Precise alignment between these structures would improve the symmetry of control. Shift-induced distortion of the metasurface was minimal.

The reliability of the device was tested with a sinusoidal voltage from 2 to 100 Hz at an amplitude of 2.5 kV to continuously vary the focal length. More than 1000 cycles without failure were achieved. By applying a voltage square wave, we were able to measure the response time of our devices to be 33±3 ms. The response time is mainly limited by the viscoelasticity of the elastomer, the charge transfer and dissipation time of the SWCNT electrodes. It is expected that both can be improved by using better elastomer materials and reducing the electrical resistance of the electrodes. Dielectric breakdown of the device was also investigated. The lens can be tuned by increasing the voltage until breakdown occurs, upon which current begins to flow through the dielectric, damaging the device. Our devices broke down at around 3.5 kV. Interestingly, the electrical breakdown was a ‘soft’ breakdown associated with local burning through the elastomer

and the same devices were able to resume normal operation after disconnecting the power and allowing the device to rest for several hours. This self-healing feature is attributed to the burning and subsequent clearing of SWCNT electrodes around the breakdown location, preventing further electrical shorting.

The current device can be improved in the following ways: Reducing the thickness of the elastomer could reduce the voltage requirement [153] (possibly to less than 12 V). Miniature high voltage components are commonly found in devices, such as cell phones, including flash modules, piezo actuators, and surface acoustic wave transducers. Another consideration is to decrease the response time to potentially μs time scale [139], [154] Also, optical performance may be improved by optimizing the transfer process as well as using other DEA materials [155].

5.3 Summary

We have demonstrated for the first time an electrically-tunable metasurface lens whose focal length, astigmatism, and shift can be simultaneously controlled by applied voltage signals to a mechanically coupled, transparent dielectric elastomer actuator. The focal length scales as the quadratic function of stretch ($\propto s^2$), yielding large changes in focal length for small strains. It brings into focus embedded optical zoom and optical image stabilization for chip-scale image sensors (e.g. cell phone cameras) as well as optical zoom and adaptive focus with lightweight form factors for head mounted optics, such as everyday eyeglasses, virtual reality and augmented reality hardware. In other applications, it allows for optical zoom and focal plane scanning for cameras, telescopes, and microscopes without the need for motorized parts. Furthermore, its flat construction and inherently lateral actuation allow for highly stackable systems, such as compound

optics. While the device presented used rigid metasurface elements, non-rigid metasurface elements individually tunable with strain can also be designed. The combination of metasurface optics and DEAs enables a versatile platform for tunable optical devices, including tunable phase, amplitude, and polarization profiles, through the electrical control of the strain field in the optical layer, making it possible to bring tunability long familiar in electron optics to flat optics.

Bibliography

[1] "Nature Milestones Photonics," 2015. [Online]. Available: http://www.nature.com/milestones/milephotons/timeline.html.

[2] R. Feynman, "There's plenty of room at the bottom," *American Physical Society meeting*, 1959. [Online]. Available: https://en.wikipedia.org/wiki/There%27s_Plenty_of_Room_at_the_Bottom.

[3] N. I. Zheludev and Y. S. Kivshar, "From metamaterials to metadevices," *Nat. Mater.*, vol. 11, p. 917, Oct. 2012.

[4] W. Cai, U. K. Chettiar, A. V Kildishev, and V. M. Shalaev, "Optical cloaking with metamaterials," *Nat. Photonics*, vol. 1, p. 224, Apr. 2007.

[5] J. B. Pendry, D. Schurig, and D. R. Smith, "Controlling Electromagnetic Fields," *Science (80-.).*, vol. 312, no. 5781, p. 1780 LP-1782, Jun. 2006.

[6] C. M. Soukoulis and M. Wegener, "Optical Metamaterials—More Bulky and Less Lossy," *Science (80-.).*, vol. 330, no. 6011, p. 1633 LP-1634, Dec. 2010.

[7] H.-H. Hsiao, C. H. Chu, and D. P. Tsai, "Fundamentals and Applications of Metasurfaces," *Small Methods*, vol. 1, no. 4, p. 1600064, 2017.

[8] M. Khorasaninejad and F. Capasso, "Metalenses: Versatile multifunctional photonic components," *Science*, vol. 358, no. 6367, American Association for the Advancement of Science, pp. 1–13, 01-Dec-2017.

[9] N. Meinzer, W. L. Barnes, and I. R. Hooper, "Plasmonic meta-atoms and metasurfaces," *Nat. Photonics*, vol. 8, no. 12, pp. 889–898, 2014.

[10] M. A. Kats, R. Blanchard, P. Genevet, and F. Capasso, "Nanometre optical coatings based on strong interference effects in highly absorbing media," *Nat. Mater.*, vol. 12, no. 1, pp. 20–24, 2012.

[11] M. A. Kats, D. Sharma, J. Lin, P. Genevet, R. Blanchard, Z. Yang, M. M. Qazilbash, D. N. Basov, S. Ramanathan, and F. Capasso, "Ultra-thin perfect absorber employing a tunable phase change material," *Appl. Phys. Lett.*, vol. 101, no. 22, 2012.

[12] N. Yu, P. Genevet, M. a Kats, F. Aieta, J.-P. Tetienne, F. Capasso, and Z. Gaburro, "Light Propagation with Phase Discontinuities Reflection and Refraction," *Science (80-.).*, vol. 334, no. 6054, pp. 333–337, 2011.

[13] F. Aieta, P. Genevet, M. A. Kats, N. Yu, R. Blanchard, Z. Gaburro, and F. Capasso, "Aberration-Free Ultrathin Flat Lenses and Axicons at Telecom Wavelengths Based on Plasmonic Metasurfaces," *Nano Lett.*, vol. 12, no. 9, pp. 4932–4936, Sep. 2012.

[14] M. Khorasaninejad, F. Aieta, P. Kanhaiya, M. A. Kats, P. Genevet, D. Rousso, and F. Capasso, “Achromatic Metasurface Lens at Telecommunication Wavelengths,” *Nano Lett.*, vol. 15, no. 8, pp. 5358–5362, 2015.

[15] S. J. Byrnes, A. Lenef, F. Aieta, and F. Capasso, “Designing large, high-efficiency, high-numerical-aperture, transmissive meta-lenses for visible light,” *Opt. Express*, vol. 24, no. January 2016, pp. 1–16, 2015.

[16] S. Zhang, M.-H. Kim, F. Aieta, A. She, T. Mansuripur, I. Gabay, M. Khorasaninejad, D. Rousso, X. Wang, M. Troccoli, N. Yu, and F. Capasso, “High efficiency near diffraction-limited mid-infrared flat lenses based on metasurface reflectarrays,” *Opt. Express*, vol. 24, no. 16, pp. 18024–18034, 2016.

[17] M. Khorasaninejad, W. T. Chen, R. C. Devlin, J. Oh, A. Y. Zhu, and F. Capasso, “Metalenses at visible wavelengths: Diffraction-limited focusing and subwavelength resolution imaging,” *Science (80-.).*, vol. 352, no. 6290, pp. 1190–1194, 2016.

[18] M. Khorasaninejad, A. Y. Zhu, C. Roques-Carmes, W. T. Chen, J. Oh, I. Mishra, R. C. Devlin, and F. Capasso, “Polarization-Insensitive Metalenses at Visible Wavelengths,” *Nano Lett.*, vol. 16, no. 11, pp. 7229–7234, Nov. 2016.

[19] A. She, S. Zhang, S. Shian, D. R. Clarke, and F. Capasso, “Large Area Electrically Tunable Lenses Based on Metasurfaces and Dielectric Elastomer Actuators,” *arXiv:1708.01972*, Aug. 2017.

[20] M. Khorasaninejad, Z. Shi, A. Y. Zhu, W. T. Chen, V. Sanjeev, A. Zaidi, and F. Capasso, “Achromatic Metalens over 60 nm Bandwidth in the Visible and Metalens with Reverse Chromatic Dispersion,” *Nano Lett.*, vol. 17, no. 3, pp. 1819–1824, Mar. 2017.

[21] B. Groever, W. T. Chen, and F. Capasso, “Meta-Lens Doublet in the Visible Region,” *Nano Lett.*, vol. 17, no. 8, pp. 4902–4907, Aug. 2017.

[22] M. Khorasaninejad, A. Ambrosio, P. Kanhaiya, and F. Capasso, “Broadband and chiral binary dielectric meta-holograms,” *Sci. Adv.*, vol. 2, no. 5, pp. e1501258–e1501258, 2016.

[23] X. Ni, A. V Kildishev, and V. M. Shalaev, “Metasurface holograms for visible light,” *Nat. Commun.*, vol. 4, pp. 1–6, 2013.

[24] J. P. B. Mueller, K. Leosson, and F. Capasso, “Ultracompact metasurface in-line polarimeter,” *Optica*, vol. 3, no. 1, pp. 42–47, Jan. 2016.

[25] S. M. Kamali, A. Arbabi, E. Arbabi, Y. Horie, and A. Faraon, “Decoupling optical function and geometrical form using conformal flexible dielectric metasurfaces,” *Nat. Commun.*, vol. 7, no. May, pp. 1–12, 2015.

[26] S. M. Kamali, E. Arbabi, A. Arbabi, Y. Horie, and A. Faraon, "Highly tunable elastic dielectric metasurface lenses," *Laser Photonics Rev.*, vol. 10, no. 6, pp. 1002–1008, 2016.

[27] M. R. M. Hashemi, S.-H. Yang, T. Wang, N. Sepúlveda, and M. Jarrahi, "Electronically-Controlled Beam-Steering through Vanadium Dioxide Metasurfaces," *Sci. Rep.*, vol. 6, no. 1, p. 35439, Dec. 2016.

[28] D. Wang, L. Zhang, Y. Gong, L. Jian, T. Venkatesan, C.-W. Qiu, and M. Hong, "Multiband Switchable Terahertz Quarter-Wave Plates via Phase-Change Metasurfaces," *IEEE Photonics J.*, vol. 8, no. 1, pp. 1–8, Feb. 2016.

[29] D. Wang, L. Zhang, Y. Gu, M. Q. Mehmood, Y. Gong, A. Srivastava, L. Jian, T. Venkatesan, C.-W. Qiu, and M. Hong, "Switchable Ultrathin Quarter-wave Plate in Terahertz Using Active Phase-change Metasurface.," *Sci. Rep.*, vol. 5, p. 15020, Oct. 2015.

[30] Q. Wang, E. T. F. Rogers, B. Gholipour, C.-M. Wang, G. Yuan, J. Teng, and N. I. Zheludev, "Optically reconfigurable metasurfaces and photonic devices based on phase change materials," *Nat. Photonics*, vol. 10, no. 1, pp. 60–65, Dec. 2015.

[31] J. Sautter, I. Staude, M. Decker, E. Rusak, D. N. Neshev, I. Brener, and Y. S. Kivshar, "Active Tuning of All-Dielectric Metasurfaces," *ACS Nano*, vol. 9, no. 4, pp. 4308–4315, Apr. 2015.

[32] O. Buchnev, N. Podoliak, M. Kaczmarek, N. I. Zheludev, and V. A. Fedotov, "Electrically Controlled Nanostructured Metasurface Loaded with Liquid Crystal: Toward Multifunctional Photonic Switch," *Adv. Opt. Mater.*, vol. 3, no. 5, pp. 674–679, May 2015.

[33] W. Zhu, Q. Song, L. Yan, W. Zhang, P.-C. Wu, L. K. Chin, H. Cai, D. P. Tsai, Z. X. Shen, T. W. Deng, S. K. Ting, Y. Gu, G. Q. Lo, D. L. Kwong, Z. C. Yang, R. Huang, A.-Q. Liu, and N. Zheludev, "A Flat Lens with Tunable Phase Gradient by Using Random Access Reconfigurable Metamaterial," *Adv. Mater.*, vol. 27, no. 32, pp. 4739–4743, Aug. 2015.

[34] N. Dabidian, I. Kholmanov, A. B. Khanikaev, K. Tatar, S. Trendafilov, S. H. Mousavi, C. Magnuson, R. S. Ruoff, and G. Shvets, "Electrical Switching of Infrared Light Using Graphene Integration with Plasmonic Fano Resonant Metasurfaces," *ACS Photonics*, vol. 2, no. 2, pp. 216–227, Feb. 2015.

[35] F. J. Morin, "Oxides Which Show a Metal-to-Insulator Transition at the Neel Temperature," *Phys. Rev. Lett.*, vol. 3, no. 1, pp. 34–36, Jul. 1959.

[36] C. Batista, R. Ribeiro, and V. Teixeira, "Synthesis and characterization of VO2-based thermochromic thin films for energy-efficient windows," *Nanoscale Res. Lett.*, vol. 6, no. 1, pp. 1–7, 2011.

[37] F. Guinneton, L. Sauques, J. C. Valmalette, F. Cros, and J. R. Gavarri, "Optimized infrared

switching properties in thermochromic vanadium dioxide thin films: Role of deposition process and microstructure," *Thin Solid Films*, vol. 446, no. 2, pp. 287–295, 2004.

[38] M. A. Kats, D. Sharma, J. Lin, P. Genevet, R. Blanchard, Z. Yang, M. M. Qazilbash, D. N. Basov, S. Ramanathan, and F. Capasso, "Ultra-thin perfect absorber employing a tunable phase change material," *Appl. Phys. Lett.*, vol. 101, no. 22, p. 221101, Nov. 2012.

[39] M. A. Kats, R. Blanchard, S. Zhang, P. Genevet, C. Ko, S. Ramanathan, and F. Capasso, "Vanadium dioxide as a natural disordered metamaterial: Perfect thermal emission and large broadband negative differential thermal emittance," *Phys. Rev. X*, vol. 3, no. 4, 2014.

[40] M. A. Kats, R. Blanchard, P. Genevet, Z. Yang, M. M. Qazilbash, D. N. Basov, S. Ramanathan, and F. Capasso, "Thermal tuning of mid-infrared plasmonic antenna arrays using a phase change material," *Opt. Lett.*, vol. 38, no. 3, pp. 368–370, 2013.

[41] M. M. Qazilbash, M. Brehm, B. G. Chae, P. C. Ho, G. O. Andreev, B. J. Kim, S. J. Yun, A. V. Balatsky, M. B. Maple, F. Keilmann, H. T. Kim, and D. N. Basov, "Mott transition in VO2 revealed by infrared spectroscopy and nano-imaging," *Science (80-.).*, vol. 318, no. 5857, pp. 1750–1753, Dec. 2007.

[42] D. Ruzmetov and S. Ramanathan, "Metal-insulator transition in thin film vanadium dioxide," in *Thin Film Metal-Oxides: Fundamentals and Applications in Electronics and Energy*, S. Ramanathan, Ed. Boston, MA: Springer US, 2010, pp. 51–94.

[43] Y. Zhou, X. Chen, C. Ko, Z. Yang, C. Mouli, and S. Ramanathan, "Voltage-triggered ultrafast phase transition in vanadium dioxide switches," *IEEE Electron Device Lett.*, vol. 34, no. 2, pp. 220–222, 2013.

[44] C. N. Berglund and H. J. Guggenheim, "Electronic Properties of VO2 near the Semiconductor-Metal Transition," *Phys. Rev.*, vol. 185, no. 3, pp. 1022–1033, Sep. 1969.

[45] T. Mitsuishi, "On the Phase Transformation of VO $_2$," *Jpn. J. Appl. Phys.*, vol. 6, no. 9, pp. 1060–1071, Sep. 1967.

[46] K. Nagashima, T. Yanagida, H. Tanaka, and T. Kawai, "Stress relaxation effect on transport properties of strained vanadium dioxide epitaxial thin films," *Phys. Rev. B*, vol. 74, no. 17, p. 172106, Nov. 2006.

[47] C. Ko and S. Ramanathan, "Stability of electrical switching properties in vanadium dioxide thin films under multiple thermal cycles across the phase transition boundary," *J. Appl. Phys.*, vol. 104, no. 8, p. 86105, Oct. 2008.

[48] N. (Nader) Engheta, R. W. Ziolkowski, and Institute of Electrical and Electronics Engineers., *Metamaterials : physics and engineering explorations*. Wiley-Interscience, 2006.

[49] S. Zhang, M. A. Kats, Y. Cui, Y. Zhou, Y. Yao, S. Ramanathan, and F. Capasso, "Current-modulated optical properties of vanadium dioxide thin films in the phase transition region," *Appl. Phys. Lett.*, vol. 105, no. 21, 2014.

[50] J. Rensberg, S. Zhang, Y. Zhou, A. S. McLeod, C. Schwarz, M. Goldflam, M. Liu, J. Kerbusch, R. Nawrodt, S. Ramanathan, D. N. Basov, F. Capasso, C. Ronning, and M. A. Kats, "Active Optical Metasurfaces Based on Defect-Engineered Phase-Transition Materials," *Nano Lett.*, vol. 16, no. 2, pp. 1050–1055, 2016.

[51] M. D. Goldflam, T. Driscoll, D. Barnas, O. Khatib, M. Royal, N. Marie Jokerst, D. R. Smith, B.-J. Kim, G. Seo, H.-T. Kim, and D. N. Basov, "Two-dimensional reconfigurable gradient index memory metasurface," *Appl. Phys. Lett.*, vol. 102, no. 22, p. 224103, Jun. 2013.

[52] M. D. Goldflam, T. Driscoll, B. Chapler, O. Khatib, N. Marie Jokerst, S. Palit, D. R. Smith, B.-J. Kim, G. Seo, H.-T. Kim, M. Di Ventra, and D. N. Basov, "Reconfigurable gradient index using VO $_2$ memory metamaterials," *Appl. Phys. Lett.*, vol. 99, no. 4, p. 44103, Jul. 2011.

[53] M. D. Goldflam, T. Driscoll, B. Chapler, O. Khatib, N. Marie Jokerst, S. Palit, D. R. Smith, B. J. Kim, G. Seo, H. T. Kim, M. Di Ventra, and D. N. Basov, "Reconfigurable gradient index using VO2 memory metamaterials," *Appl. Phys. Lett.*, vol. 99, no. 4, pp. 2011–2014, 2011.

[54] Y. Z. and J. H. and C. C. and Z. Fan, "Electrically controlled metal–insulator transition process in VO 2 thin films," *J. Phys. Condens. Matter*, vol. 24, no. 3, p. 35601, 2012.

[55] E. Dagotto, M. Brehm, B.-G. Chae, P.-C. Ho, G. O. Andreev, B.-J. Kim, S. J. Yun, A. V. Balatsky, M. B. Maple, F. Keilmann, H.-T. Kim, and D. N. Basov, "Complexity in strongly correlated electronic systems.," *Science*, vol. 309, no. 5732, pp. 257–62, Jul. 2005.

[56] A. Crunteanu, J. Givernaud, J. Leroy, D. Mardivirin, C. Champeaux, J. C. Orlianges, A. Catherinot, and P. Blondy, "Voltage- and current-activated metal-insulator transition in VO 2-based electrical switches: A lifetime operation analysis," *Sci. Technol. Adv. Mater.*, vol. 11, no. 6, p. 65002, Dec. 2010.

[57] H.-T. Kim, B.-G. Chae, D.-H. Youn, G. Kim, K.-Y. Kang, S.-J. Lee, K. Kim, and Y.-S. Lim, "Raman study of electric-field-induced first-order metal-insulator transition in VO2-based devices," *Appl. Phys. Lett.*, vol. 86, no. 24, p. 242101, Jun. 2005.

[58] P. Schilbe, "Raman scattering in VO2," in *Physica B: Condensed Matter*, 2002, vol. 316–317, pp. 600–602.

[59] D. R. Smith, J. B. Pendry, and M. C. K. Wiltshire, "Metamaterials and negative refractive index.," *Science*, vol. 305, no. 5685, pp. 788–92, Aug. 2004.

[60] H.-T. Chen, W. J. Padilla, J. M. O. Zide, A. C. Gossard, A. J. Taylor, and R. D. Averitt, "Active terahertz metamaterial devices," *Nature*, vol. 444, no. 7119, pp. 597–600, Nov. 2006.

[61] J.-Y. Ou, E. Plum, J. Zhang, and N. I. Zheludev, "An electromechanically reconfigurable plasmonic metamaterial operating in the near-infrared," *Nat. Nanotechnol.*, vol. 8, no. 4, pp. 252–255, Mar. 2013.

[62] Y. Yao, R. Shankar, M. A. Kats, Y. Song, J. Kong, M. Loncar, and F. Capasso, "Electrically Tunable Metasurface Perfect Absorbers for Ultrathin Mid-Infrared Optical Modulators," *Nano Lett.*, vol. 14, no. 11, pp. 6526–6532, Nov. 2014.

[63] Q. Zhao, L. Kang, B. Du, B. Li, J. Zhou, H. Tang, X. Liang, and B. Zhang, "Electrically tunable negative permeability metamaterials based on nematic liquid crystals," *Appl. Phys. Lett.*, vol. 90, no. 1, p. 11112, Jan. 2007.

[64] D. H. Werner, D.-H. Kwon, I.-C. Khoo, A. V. Kildishev, and V. M. Shalaev, "Liquid crystal clad near-infrared metamaterials with tunable negative-zero-positive refractive indices," *Opt. Express*, vol. 15, no. 6, p. 3342, Mar. 2007.

[65] M. Imada, A. Fujimori, and Y. Tokura, "Metal-insulator transitions," *Rev. Mod. Phys.*, vol. 70, no. 4, pp. 1039–1263, Oct. 1998.

[66] M. Liu, H. Y. Hwang, H. Tao, A. C. Strikwerda, K. Fan, G. R. Keiser, A. J. Sternbach, K. G. West, S. Kittiwatanakul, J. Lu, S. A. Wolf, F. G. Omenetto, X. Zhang, K. A. Nelson, and R. D. Averitt, "Terahertz-field-induced insulator-to-metal transition in vanadium dioxide metamaterial," *Nature*, vol. 487, no. 7407, pp. 345–348, Jul. 2012.

[67] P. Hosseini, C. D. Wright, and H. Bhaskaran, "An optoelectronic framework enabled by low-dimensional phase-change films," *Nature*, vol. 511, no. 7508, pp. 206–211, Jul. 2014.

[68] X. Yin, M. Schäferling, A.-K. U. Michel, A. Tittl, M. Wuttig, T. Taubner, and H. Giessen, "Active Chiral Plasmonics," *Nano Lett.*, vol. 15, no. 7, pp. 4255–4260, Jul. 2015.

[69] L. A. Ladd and W. Paul, "Optical and Transport Properties of High Quality Crystals of V_2O_4 Near the Metallic Transition temperature," *Solid State Commun.*, vol. 7, no. 4, pp. 425–428, Feb. 1969.

[70] R. Jaramillo, S. D. Ha, D. M. Silevitch, and S. Ramanathan, "Origins of bad metal conductivity and the insulator-metal transition in the rare-earth nickelates," Sep. 2013.

[71] M. Sheik-Bahae, D. J. Hagan, and E. W. Van Stryland, "Dispersion and band-gap scaling of the electronic Kerr effect in solids associated with two-photon absorption," *Phys. Rev. Lett.*, vol. 65, no. 1, pp. 96–99, Jul. 1990.

[72] M. Humar, M. Ravnik, S. Pajk, and I. Muševič, "Electrically tunable liquid crystal optical microresonators," *Nat. Photonics*, vol. 3, no. 10, pp. 595–600, Oct. 2009.

[73] M. A. Kats, R. Blanchard, P. Genevet, Z. Yang, M. M. Qazilbash, D. N. Basov, S. Ramanathan, and F. Capasso, "Thermal tuning of mid-infrared plasmonic antenna arrays using a phase change material.," *Opt. Lett.*, vol. 38, no. 3, pp. 368–70, 2013.

[74] K. Shibuya, M. Kawasaki, and Y. Tokura, "Metal-insulator transition in epitaxial V1−xWxO2(0≤x≤0.33) thin films," *Appl. Phys. Lett.*, vol. 96, no. 2, p. 22102, Jan. 2010.

[75] C. Kübler, H. Ehrke, R. Huber, R. Lopez, A. Halabica, R. F. Haglund, and A. Leitenstorfer, "Coherent Structural Dynamics and Electronic Correlations during an Ultrafast Insulator-to-Metal Phase Transition in VO 2," *Phys. Rev. Lett.*, vol. 99, no. 11, p. 116401, Sep. 2007.

[76] K. Appavoo, D. Y. Lei, Y. Sonnefraud, B. Wang, S. T. Pantelides, S. A. Maier, and R. F. Haglund, "Role of Defects in the Phase Transition of VO 2 Nanoparticles Probed by Plasmon Resonance Spectroscopy," *Nano Lett.*, vol. 12, no. 2, pp. 780–786, Feb. 2012.

[77] J. Cao, Y. Gu, W. Fan, L. Q. Chen, D. F. Ogletree, K. Chen, N. Tamura, M. Kunz, C. Barrett, J. Seidel, and J. Wu, "Extended Mapping and Exploration of the Vanadium Dioxide Stress-Temperature Phase Diagram," *Nano Lett.*, vol. 10, no. 7, pp. 2667–2673, Jul. 2010.

[78] J. H. Park, J. M. Coy, T. S. Kasirga, C. Huang, Z. Fei, S. Hunter, and D. H. Cobden, "Measurement of a solid-state triple point at the metal–insulator transition in VO2," *Nature*, vol. 500, no. 7463, pp. 431–434, Aug. 2013.

[79] N. B. Aetukuri, A. X. Gray, M. Drouard, M. Cossale, L. Gao, A. H. Reid, R. Kukreja, H. Ohldag, C. A. Jenkins, E. Arenholz, K. P. Roche, H. A. Dürr, M. G. Samant, and S. S. P. Parkin, "Control of the metal–insulator transition in vanadium dioxide by modifying orbital occupancy," *Nat. Phys.*, vol. 9, no. 10, pp. 661–666, Sep. 2013.

[80] M. Brokate, "Hysteresis Operators," in *Lecture Notes in Mathematics*, vol. 1584, Springer, New York, NY, 1994, pp. 1–38.

[81] L. Zhao, L. Miao, C. Liu, C. Li, T. Asaka, Y. Kang, Y. Iwamoto, S. Tanemura, H. Gu, and H. Su, "Solution-processed VO2-SiO2 composite films with simultaneously enhanced luminous transmittance, solar modulation ability and anti-oxidation property.," *Sci. Rep.*, vol. 4, p. 7000, Nov. 2014.

[82] W. Wesch, E. Wendler, and C. S. Schnohr, "Damage evolution and amorphization in semiconductors under ion irradiation," *Nucl. Instruments Methods Phys. Res. Sect. B Beam Interact. with Mater. Atoms*, vol. 277, pp. 58–69, Apr. 2012.

[83] H. Hofsäss, P. Ehrhardt, H.-G. Gehrke, M. Brötzmann, U. Vetter, K. Zhang, J. Krauser, C. Trautmann, C. Ko, and S. Ramanathan, "Tuning the conductivity of vanadium dioxide films

on silicon by swift heavy ion irradiation," *AIP Adv.*, vol. 1, no. 3, p. 32168, Sep. 2011.

[84] K.-D. Ufert and E. I. Terukov, "On the Problem of the Phase Transition in Disordered VO2 Thin Films," *Phys. Status Solidi*, vol. 40, no. 2, pp. K157–K159, Apr. 1977.

[85] H. Choi, J. Ahn, J. Jung, T. Noh, and D. Kim, "Mid-infrared properties of a VO2 film near the metal-insulator transition," *Phys. Rev. B*, vol. 54, no. 7, pp. 4621–4628, 1996.

[86] D. A. G. Bruggeman, "Berechnzcrrg verschCedcner physikalducher Eonstanten von heterogenew Yuhstan.xen 1.," *Ann. Phys.*, vol. 24, no. 7, pp. 636–664, Jan. 1935.

[87] D. Polder and J. H. van Santen, "The effective permeability of mixtures of solids," *Physica*, vol. 12, no. 5, pp. 257–271, Aug. 1946.

[88] D. Schmidt and M. Schubert, "Anisotropic Bruggeman effective medium approaches for slanted columnar thin films," *J. Appl. Phys.*, vol. 114, no. 8, p. 83510, Aug. 2013.

[89] X. Zhong, X. Zhang, A. Gupta, and P. LeClair, "Avalanche breakdown in microscale VO_2 structures," *J. Appl. Phys.*, vol. 110, no. 8, p. 84516, Oct. 2011.

[90] M. Schubert, T. E. Tiwald, and C. M. Herzinger, "Infrared dielectric anisotropy and phonon modes of sapphire," *Phys. Rev. B*, vol. 61, no. 12, pp. 8187–8201, Mar. 2000.

[91] H. Looyenga, "Dielectric constants of heterogeneous mixtures," *Physica*, vol. 31, no. 3, pp. 401–406, 1965.

[92] A. V. Goncharenko, V. Z. Lozovski, and E. F. Venger, "Lichtenecker's equation: applicability and limitations," *Opt. Commun.*, vol. 174, no. 1–4, pp. 19–32, Jan. 2000.

[93] T. Paik, S.-H. Hong, E. A. Gaulding, H. Caglayan, T. R. Gordon, N. Engheta, C. R. Kagan, and C. B. Murray, "Solution-Processed Phase-Change VO_2 Metamaterials from Colloidal Vanadium Oxide (VO_x) Nanocrystals," *ACS Nano*, vol. 8, no. 1, pp. 797–806, Jan. 2014.

[94] M. Liu, A. J. Sternbach, M. Wagner, T. V. Slusar, T. Kong, S. L. Bud'ko, S. Kittiwatanakul, M. M. Qazilbash, A. McLeod, Z. Fei, E. Abreu, J. Zhang, M. Goldflam, S. Dai, G.-X. Ni, J. Lu, H. A. Bechtel, M. C. Martin, M. B. Raschke, R. D. Averitt, S. A. Wolf, H.-T. Kim, P. C. Canfield, and D. N. Basov, "Phase transition in bulk single crystals and thin films of V O 2 by nanoscale infrared spectroscopy and imaging," *Phys. Rev. B*, vol. 91, no. 24, p. 245155, Jun. 2015.

[95] T. Jostmeier, J. Zimmer, H. Karl, H. J. Krenner, and M. Betz, "Optically imprinted reconfigurable photonic elements in a VO_2 nanocomposite," *Appl. Phys. Lett.*, vol. 105, no. 7, p. 71107, Aug. 2014.

[96] R. Soref and B. Bennett, "Electrooptical effects in silicon," *IEEE J. Quantum Electron.*, vol. 23, no. 1, pp. 123–129, Jan. 1987.

[97] A. Tittl, A.-K. U. Michel, M. Schäferling, X. Yin, B. Gholipour, L. Cui, M. Wuttig, T. Taubner, F. Neubrech, and H. Giessen, "A Switchable Mid-Infrared Plasmonic Perfect Absorber with Multispectral Thermal Imaging Capability," *Adv. Mater.*, vol. 27, no. 31, pp. 4597–4603, Aug. 2015.

[98] A. Schliesser, N. Picqué, and T. W. Hänsch, "Mid-infrared frequency combs," *Nat. Photonics*, vol. 6, no. 7, pp. 440–449, 2012.

[99] R. Soref, "Mid-infrared photonics in silicon and germanium," *Nat. Photonics*, vol. 4, no. 8, pp. 495–497, 2010.

[100] E. Optics, "The correct material for infrared (IR) applications." [Online]. Available: http://www.edmundoptics.com/resources/application-notes/optics/the-correct-material-for-infrared-applications/.

[101] Y. Nanfang, P. Genevet, F. Aieta, M. A. Kats, R. Blanchard, G. Aoust, J. P. Tetienne, Z. Gaburro, and F. Capasso, "Flat Optics: Controlling Wavefronts With Optical Antenna Metasurfaces," *Sel. Top. Quantum Electron. IEEE J.*, vol. 19, no. 3, p. 4700423, 2013.

[102] Y. C. Cheng, S. Kicas, J. Trull, M. Peckus, C. Cojocaru, R. Vilaseca, R. Drazdys, and K. Staliunas, "Flat Focusing Mirror," *Sci. Rep.*, vol. 4, p. 6326, 2014.

[103] D. Fattal, J. Li, Z. Peng, M. Fiorentino, and R. G. Beausoleil, "Flat dielectric grating reflectors with focusing abilities," *Nat Phot.*, vol. 4, no. 7, pp. 466–470, 2010.

[104] A. Pors, M. G. Nielsen, R. L. Eriksen, and S. I. Bozhevolnyi, "Broadband Focusing Flat Mirrors Based on Plasmonic Gradient Metasurfaces," *Nano Lett.*, vol. 13, no. 2, pp. 829–834, 2013.

[105] A. T. Tokunaga, T. Bond, J. Elias, M. Chun, M. Richter, M. Liang, J. Lacy, L. Daggert, E. Tollestrup, M. Ressler, D. Warren, S. Fisher, and J. Carr, "Design tradeoffs for a high spectral resolution mid-infrared echelle spectrograph on the Thirty-Meter Telescope," 2006, vol. 6269, p. 62693Y.

[106] R. Lu, "Infrared microscopy applications," 2013. [Online]. Available: http://www.gia.edu/gia-news-research-Infrared-Microscopy-Applications.

[107] S. Sun, K.-Y. Yang, C.-M. Wang, T.-K. Juan, W. T. Chen, C. Y. Liao, Q. He, S. Xiao, W.-T. Kung, G.-Y. Guo, L. Zhou, and D. P. Tsai, "High-Efficiency Broadband Anomalous Reflection by Gradient Meta-Surfaces," *Nano Lett.*, vol. 12, no. 12, pp. 6223–6229, 2012.

[108] S. Sun, Q. He, S. Xiao, Q. Xu, X. Li, and L. Zhou, "Gradient-index meta-surfaces as a bridge linking propagating waves and surface waves," *Nat Mater*, vol. 11, no. 5, pp. 426–431, 2012.

[109] A. Arbabi, R. M. Briggs, Y. Horie, M. Bagheri, and A. Faraon, "Efficient dielectric metasurface collimating lenses for mid-infrared quantum cascade lasers," *Opt. Express*, vol. 23, no. 26, p. 33310, 2015.

[110] A. B. Klemm, D. Stellinga, E. R. Martins, L. Lewis, G. Huyet, L. O'Faolain, and T. F. Krauss, "Experimental high numerical aperture focusing with high contrast gratings," *Opt. Lett.*, vol. 38, no. 17, pp. 3410–3413, 2013.

[111] D. Hu, X. Wang, S. Feng, J. Ye, W. Sun, Q. Kan, P. J. Klar, and Y. Zhang, "Ultrathin Terahertz Planar Elements," *Adv. Opt. Mater.*, vol. 1, no. 2, pp. 186–191, 2013.

[112] I. Lumerical Solutions, "Far field from periodic structures." [Online]. Available: https://kb.lumerical.com/en/solvers_grating_projections_far_field.html.

[113] R. O'Connell, "Telescope optical design," *ASTR 511: AStronomical Techniques*. .

[114] N. M. Estakhri and A. Alù, "Recent progress in gradient metasurfaces," *J. Opt. Soc. Am. B*, vol. 33, no. 2, p. A21, 2015.

[115] A. Epstein and G. V Eleftheriades, "Huygens' metasurfaces via the equivalence principle: design and applications," *J. Opt. Soc. Am. B*, vol. 33, no. 2, pp. A31–A50, 2016.

[116] F. Aieta, P. Genevet, M. Kats, and F. Capasso, "Aberrations of flat lenses and aplanatic metasurfaces," *Opt. Express*, vol. 21, no. 25, pp. 31530–31539, 2013.

[117] P. Wang, N. Mohammad, and R. Menon, "Chromatic-aberration-corrected diffractive lenses for ultra-broadband focusing," *Sci. Rep.*, vol. 6, no. 1, p. 21545, Aug. 2016.

[118] Y. Li, X. Li, M. Pu, Z. Zhao, X. Ma, Y. Wang, and X. Luo, "Achromatic flat optical components via compensation between structure and material dispersions," *Sci. Rep.*, vol. 6, no. 1, p. 19885, Apr. 2016.

[119] E. Arbabi, A. Arbabi, S. M. Kamali, Y. Horie, and A. Faraon, "Multiwavelength polarization insensitive lenses based on dielectric metasurfaces with meta-molecules," *Optica*, vol. 3, no. 6, p. 628, 2016.

[120] J. Cheng and H. Mosallaei, "Truly achromatic optical metasurfaces: a filter circuit theory-based design," *J. Opt. Soc. Am. B*, vol. 32, no. 10, pp. 2115–2121, 2015.

[121] F. Aieta, M. A. Kats, P. Genevet, and F. Capasso, "Multiwavelength achromatic metasurfaces by dispersive phase compensation," *Science (80-.).*, vol. 347, no. 6228, pp. 1342–1345, 2015.

[122] T. Roy, S. Zhang, I. L. W. Jung, M. Troccoli, and F. Capasso, "Dynamic metasurface lens based on MEMS Technology," *arXiv: 1712.03616*, Dec. 2017.

[123] O. Solgaard and SpringerLink (Online service), “Photonic Microsystems: Micro and Nanotechnology Applied to Optical Devices and Systems,” *Springer eBooks*, 2009.

[124] B. Schwarz, “Lidar: Mapping the world in 3D,” *Nat. Photonics*, vol. 4, no. 7, pp. 429–430, Jul. 2010.

[125] J. E. Ford, M. C. Wu, and O. Solgaard, “Optical MEMS for Lightwave Communication,” *J. Light. Technol. Vol. 24, Issue 12, pp. 4433-4454*, vol. 24, no. 12, pp. 4433–4454, Dec. 2006.

[126] V. A. Aksyuk, M. E. Simon, F. Pardo, S. Arney, D. Lopez, and A. Villanueva, “Optical MEMS design for telecommunications applications,” in *Proc. Solid-state sensor, actuator and Microsystems workshop*, 2002.

[127] I. W. Jung, S. Rattanavarin, P. Sarapukdee, M. J. Mandella, W. Piyawattanametha, and D. López, “2-D MEMS scanner for handheld multispectral confocal microscopes,” *2012 International Conference on Optical MEMS and Nanophotonics*. pp. 238–239, 2012.

[128] S. Rattanavarin, P. Sarapukdee, N. Khemthongcharoen, U. Jarujareet, R. Jolivot, I. W. Jung, D. López, M. J. Mandella, and W. Piyawattanametha, “MEMS based multispectral confocal probe,” *2013 Transducers & Eurosensors XXVII: The 17th International Conference on Solid-State Sensors, Actuators and Microsystems (TRANSDUCERS & EUROSENSORS XXVII)*. pp. 2173–2176, 2013.

[129] C. Yin, A. K. Glaser, S. Y. Leigh, Y. Chen, L. Wei, P. C. S. Pillai, M. C. Rosenberg, S. Abeytunge, G. Peterson, C. Glazowski, N. Sanai, M. J. Mandella, M. Rajadhyaksha, and J. T. C. Liu, “Miniature in vivo MEMS-based line-scanned dual-axis confocal microscope for point-of-care pathology,” *Biomed. Opt. Express*, vol. 7, no. 2, pp. 251–263, 2016.

[130] W. Jung, S. Tnag, T. Xie, D. T. Mccormick, Y.-C. Ahn, J. Su, I. V Tomov, T. B. Krasieva, B. J. Tromberg, and Z. Chen, “Miniaturized probe using 2 axis MEMS scanner for endoscopic multiphoton excitation microscopy,” in *Proceedings of SPIE*, 2008, p. 68510D.

[131] G. T. Kovacs, *Micromachined Transducers Sourcebook*. McGraw-Hill Companies, 1998.

[132] B. Park, I. W. Jung, J. Provine, O. Solgaard, and R. T. Howe, “Highly Sensitive Monolithic Silicon Photonic Crystal Fiber Tip Sensor for Simultaneous Measurement of Refractive Index and Temperature,” *J. Light. Technol. Vol. 29, Issue 9, pp. 1367-1374*, vol. 29, no. 9, pp. 1367–1374, May 2011.

[133] T. R. Dallmeyer, “Photographic lens.” Google Patents, 1904.

[134] L. W. Alvarez, “Two-element variable-power spherical lens,” 1967.

[135] L. Li, D. Bryant, T. van Heugten, and P. J. Bos, “Physical limitations and fundamental factors affecting performance of liquid crystal tunable lenses with concentric electrode

rings," *Appl. Opt.*, vol. 52, no. 9, p. 1978, Mar. 2013.

[136] L. Li, D. Bryant, T. Van Heugten, and P. J. Bos, "Near-diffraction-limited and low-haze electro-optical tunable liquid crystal lens with floating electrodes," *Opt. Express*, vol. 21, no. 7, p. 8371, Apr. 2013.

[137] N. Hasan, A. Banerjee, H. Kim, and C. H. Mastrangelo, "Tunable-focus lens for adaptive eyeglasses," *Opt. Express*, vol. 25, no. 2, p. 1221, Jan. 2017.

[138] E. Simon, B. Berge, F. Fillit, H. Gaton, M. Guillet, O. Jacques-Sermet, F. Laune, J. Legrand, M. Maillard, and N. Tallaron, "Optical design rules of a camera module with a liquid lens and principle of command for AF and OIS functions," in *Proceedings of SPIE*, 2010, p. 784903.

[139] L. Maffli, S. Rosset, M. Ghilardi, F. Carpi, and H. Shea, "Ultrafast All-Polymer Electrically Tunable Silicone Lenses," *Adv. Funct. Mater.*, vol. 25, no. 11, pp. 1656–1665, Mar. 2015.

[140] S. Shian, R. M. Diebold, and D. R. Clarke, "High-speed, compact, adaptive lenses using in-line transparent dielectric elastomer actuator membranes," in *Proceedings of SPIE*, 2013, vol. 21, p. 86872D.

[141] S. Shian, R. M. Diebold, and D. R. Clarke, "Tunable lenses using transparent dielectric elastomer actuators.," *Opt. Express*, vol. 21, no. 7, pp. 8669–76, 2013.

[142] M. Blum, M. Büeler, C. Grätzel, and M. Aschwanden, "Compact optical design solutions using focus tunable lenses," in *Proceeding of SPIE*, 2011, vol. 8167, p. 81670W.

[143] A. Mermillod-Blondin, E. McLeod, and C. B. Arnold, "High-speed varifocal imaging with a tunable acoustic gradient index of refraction lens," *Opt. Lett.*, vol. 33, no. 18, p. 2146, Sep. 2008.

[144] M. Duocastella, G. Vicidomini, and A. Diaspro, "Simultaneous multiplane confocal microscopy using acoustic tunable lenses," *Opt. Express*, vol. 22, no. 16, p. 19293, Aug. 2014.

[145] H.-S. Ee and R. Agarwal, "Tunable Metasurface and Flat Optical Zoom Lens on a Stretchable Substrate," *Nano Lett.*, vol. 16, no. 4, pp. 2818–2823, Apr. 2016.

[146] S. C. Malek, H.-S. Ee, and R. Agarwal, "Strain Multiplexed Metasurface Holograms on a Stretchable Substrate," *Nano Lett.*, vol. 17, no. 6, pp. 3641–3645, May 2017.

[147] A. She, S. Zhang, S. Shian, D. R. Clarke, and F. Capasso, "Large area metalenses: design, characterization, and mass manufacturing," *Opt. Express*, vol. 26, no. 2, p. 1573, Jan. 2018.

[148] P. Brochu and Q. Pei, "Advances in Dielectric Elastomers for Actuators and Artificial Muscles," *Macromol. Rapid Commun.*, vol. 31, no. 1, pp. 10–36, Jan. 2010.

[149] J. Huang, T. Li, C. Chiang Foo, J. Zhu, D. R. Clarke, and Z. Suo, “Giant, voltage-actuated deformation of a dielectric elastomer under dead load,” *Appl. Phys. Lett.*, vol. 100, no. 4, p. 41911, Jan. 2012.

[150] S. J. A. Koh, T. Li, J. Zhou, X. Zhao, W. Hong, J. Zhu, and Z. Suo, “Mechanisms of large actuation strain in dielectric elastomers,” *J. Polym. Sci. Part B Polym. Phys.*, vol. 49, no. 7, pp. 504–515, Apr. 2011.

[151] A. She, S. Zhang, and F. Capasso, “Highly Efficient Data Representation Of Dense Polygonal Structures,” 2017.

[152] S. Shian, R. M. Diebold, A. McNamara, and D. R. Clarke, “Highly compliant transparent electrodes,” *Appl. Phys. Lett.*, vol. 101, no. 6, p. 61101, Aug. 2012.

[153] T. Töpper, F. Weiss, B. Osmani, C. Bippes, V. Leung, and B. Müller, “Siloxane-based thin films for biomimetic low-voltage dielectric actuators,” *Sensors Actuators A Phys.*, vol. 233, pp. 32–41, Sep. 2015.

[154] S. Rosset and H. R. Shea, “Small, fast, and tough: Shrinking down integrated elastomer transducers,” *Appl. Phys. Rev.*, vol. 3, no. 3, p. 31105, Sep. 2016.

[155] C. Keplinger, J.-Y. Sun, C. C. Foo, P. Rothemund, G. M. Whitesides, and Z. Suo, “Stretchable, Transparent, Ionic Conductors,” *Science (80-.).*, vol. 341, no. 6149, pp. 984–987, 2013.

Appendix A
Characterization of VO_2-based metasurfaces

A1: X-ray diffraction measurements

The quality of the as-grown VO_2 films on c-Al_2O_3 was investigated using X-ray diffraction measurements (Figure A1). Besides reflections from 0 0 6 and 0 0 12 planes of the Al_2O_3 substrates, only reflections from 0 2 0 and 0 4 0 planes of monoclinic VO_2 can be seen indicating either epitaxial or textured growth with the *b*-axis of the film normal to the substrate surface.

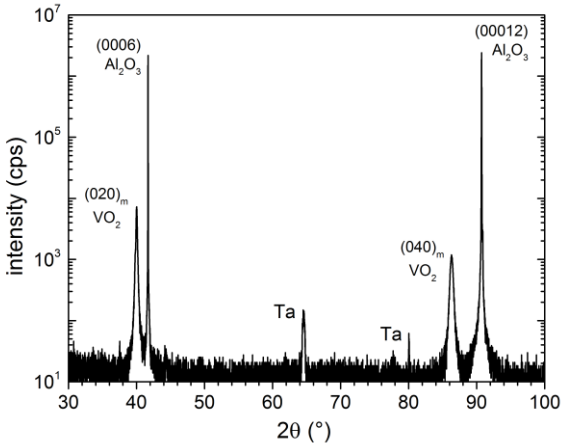

Figure A1: *X-ray diffraction pattern of a 100 nm as grown VO_2 thin film on c-axis oriented Al_2O_3. Only reflections from the 020 and 040 VO_2 and 0006 and 000 12 Al_2O_3 planes are found indicating excellent oriented growth. Weak additional reflections are caused by the use of a tantalum strip heater which was placed underneath the sample during measurements.*

A2: Ion distribution and damage simulations

The VO_2 thin films on *c*-Al_2O_3 were irradiated with 75 keV Ar^+ or 190 keV Cs^+ ions at room temperature with ion fluences ranging from $N_I = 5\times10^{12}$ to $N_I = 1\times10^{15}$ cm^{-2}. The corresponding depth and damage profiles of implanted ions were calculated with the computer code Stopping and Range of Ions in Matter (SRIM) and are shown in Figure A2(a) and (b). As input parameters, we used the given displacement energies of SRIM as 25 eV and 28 eV for V and O, respectively.

For both irradiation conditions, the projected ion range is centered within the 100 nm VO_2 film. As the ion beam penetrates the film, it also spreads out laterally in respect to the ion beam direction (lateral straggle). If a mask covers half of a sample (lateral position > 0 in Figure A2(c)), the lateral range of ions is defined as the distance under the mask where the concentration of the implanted species drops to 25% (at the mask edge the concentration is ~ 50% of the uniform value). The simulated lateral distribution of ions for 75 keV Ar^+ and 190 keV Cs^+ irradiation is shown in Figure A2(c) and is calculated to be ~15 nm and ~12 nm, respectively.

The calculated number of primary displacements per lattice atom (n_{dpa}) by SRIM, used as a bottom scale in Figure A2(b), depends on the ion energy as well as on the mass of ion and target atoms, and is the sum of both V and O Frenkel pairs created in the kinematic collision process for VO_2 at T = 0. Thus, although it does not consider dynamic annealing processes, it allows for a direct comparison of the number of primary created defects by the different irradiations (here: 75 keV Ar^+ versus 190 keV Cs^+). The value increases linearly with ion fluence for any irradiation condition, as shown as a top scale of Figure A2(b).

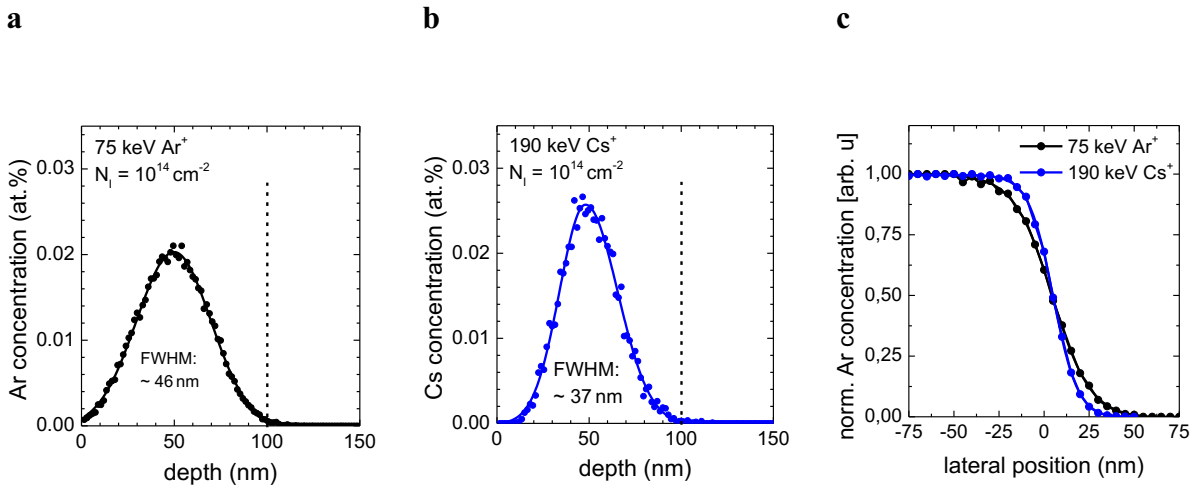

Figure A2 *Simulated depth profiles of (a) 75 keV Ar^+ and (b) 190 keV Cs^+ ion implantation into VO_2 using SRIM for a fixed ion fluence of $N_I = 10^{14}$ cm^{-2}, respectively. The dotted line indicates the interface to the sapphire substrate. No interface mixing is expected. (c) Simulated lateral concentration of Ar^+ and Cs^+ ions at a penetration depth of 50 nm for a sample, which is half covered with an irradiation mask. The mask covers positive lateral positions, and no ions can penetrate through the mask.*

A3: RBS/Channeling measurements

Rutherford backscattering spectrometry in channeling geometry (RBS/C) was performed to evaluate the defect concentration in intrinsic and irradiated VO_2. A relatively low yield from He ions backscattered from vanadium atoms in the channeling direction compared to the yield in a random direction indicates a low defect concentration of the as-grown VO_2 (Figure A3(a)). With increasing ion fluence, the backscattering yield increases due to the presence of lattice defects. From RBS/C measurements, the defect concentration of the VO_2 thin film can be estimated as the fraction of backscattering yield in the channeling direction compared to the backscattering yield in a random direction (Figure A3(b)). Progressive amorphization with increasing ion fluence N_I

due to defect accumulation can be described by a direct-impact model where each ion creates a small defective region in the lattice with damage cross-section σ. The defect concentration can then be determined as $n = (1 - e^{-\sigma N_I})$. Figure A3(b) shows the defect concentration calculated in the middle of the VO_2 layer (channel ~425) and the direct impact model fit to this data ($\sigma \sim 3 \times 10^{14}$ cm^{-2}). It can also be seen that for ion fluences above ~ 1×10^{15} cm^{-2}, the VO_2 layer is amorphous ($n = 1$).

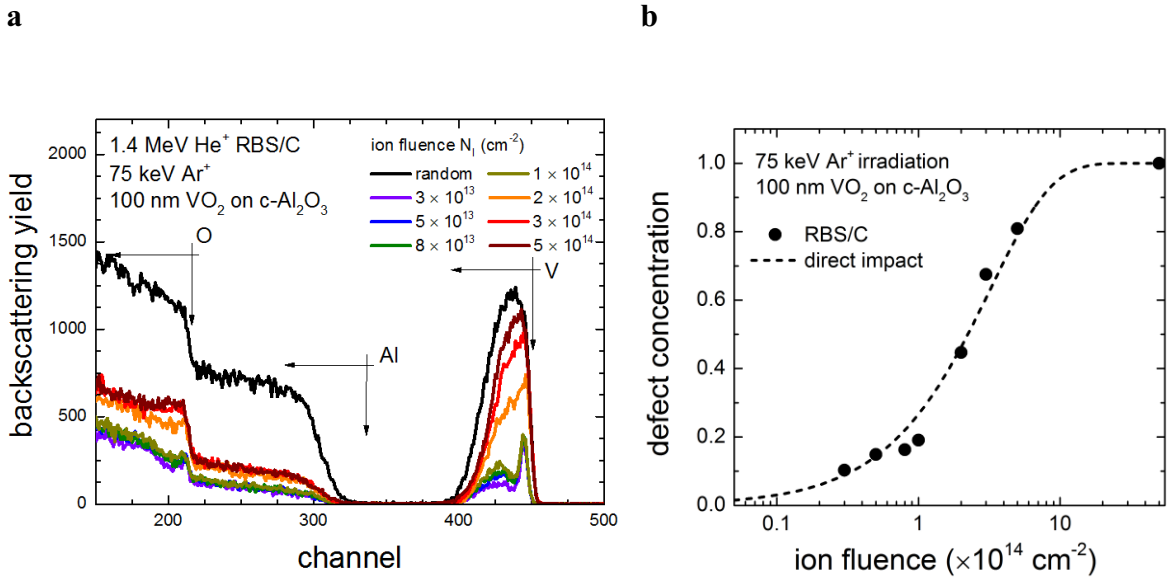

Figure A3 *(a) RBS/C spectra of intrinsic and irradiated VO_2 as a function of ion fluence. The samples were irradiated with 75 keV Ar^+ ions at room temperature. (b) Damage fraction calculated from the vanadium part of the RBS/C spectra. The dashed line corresponds to a direct impact model that fits the data well.*

A4: Scattering type scanning near-field infrared microscopy (SNIM)

By comparing the near-field images with high-resolution atomic force microscopy images that were taken simultaneously, we observed that the spatial boundary between metallic and

insulating VO_2 follows the grain boundaries. The grains are visible in the AFM images (Figure A4) , and have a grain size between 20 and 100 nm.

s-SNIM AFM

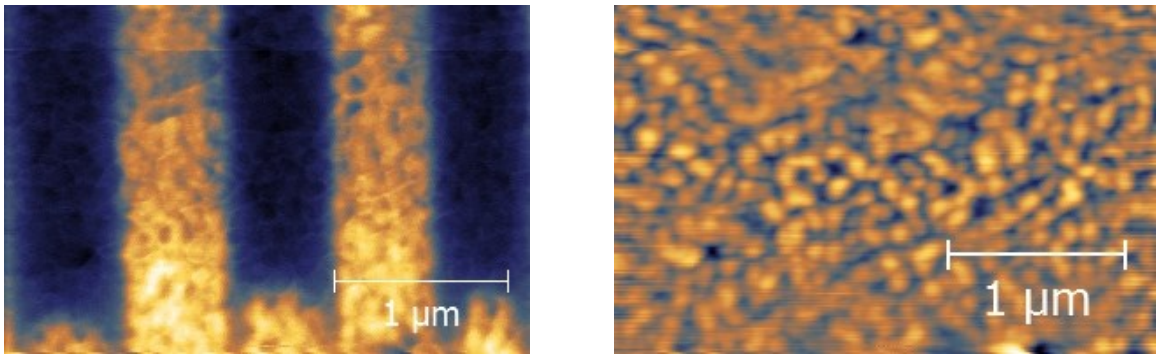

Figure A4 *Comparison of a near-field image obtained by s-SNIM and the corresponding AFM image that was taken simultaneously. Dark (bright) regions in the s-SNIM image correspond to insulating (metallic) VO_2 that causes a small (large) scattering amplitude.*